AUTOMATED STRAIN ANALYSIS SYSTEM: DEVELOPMENT AND APPLICATIONS

By

WEIQI YIN

A DISSERTATION PRESENTED TO THE GRADUATE SCHOOL
OF THE UNIVERSITY OF FLORIDA IN PARTIAL FULFILLMENT
OF THE REQUIREMENTS FOR THE DEGREE OF
DOCTOR OF PHILOSOPHY

UNIVERSITY OF FLORIDA

2009

To my parents, Guoyin and Jine, and my wife, Min

ACKNOWLEDGMENTS

I sincerely thank my advisor, Dr. Peter Ifju, for his support, guidance, knowledge and friendship. It is very fortunate for me to work with him. Also, I sincerely thank my committee members, Dr. Bhavani Sankar, Dr. Raphael Haftka, Dr. Youping Chen and Dr. Mang Tia, for participating and evaluating my research work.

I would like to especially thank Tzuchau Chen, my colleague in the Experimental Stress Analysis lab for his continuous help on experiments and shared knowledge. I would also like to thank my other lab colleagues, Nancy Strickland, Vijay Jagdale and Mulugeta Haile, for their shared knowledge and help. I am very grateful to Christian Gogu for his shared knowledge on material property identification using full field measurement.

TABLE OF CONTENTS

LIST OF TABLES

LIST OF FIGURES

Abstract of Dissertation Presented to the Graduate School
of the University of Florida in Partial Fulfillment of the
Requirements for the Degree of Doctor of Philosophy

AUTOMATED STRAIN ANALYSIS SYSTEM: DEVELOPMENT AND APPLICATIONS

By

Weiqi Yin

December 2009

Chair: Peter G. Ifju
Major: Mechanical Engineering

Interferometry has been widely applied for industrial and scientific studies because of its capability of full-field displacement measurement, high sensitivity and high spatial resolution. The output of moiré is represented as interference fringe patterns which need to be analyzed to obtain the desired physical parameters such as displacements, strains, etc. Numerous algorithms have been developed for fringe pattern analysis, however, most of them are focused on specific aspect and hard to be automated, and the strain result is usually a qualitative analysis. In this dissertation, the existing techniques were investigated, the appropriate algorithms were adopted, some of the selected algorithms were improved, and new algorithms were developed.

A technique based on phase extraction is investigated, improved and applied for fringe pattern analysis. Phase shifting method uses a series of phase shifted fringe patterns and involves procedures of noise filtering, wrapped phase calculation, phase unwrapping, and calculation of displacement and strain. Appropriate digital image processing techniques are applied for noise filtering. Phase shifting algorithm is used to calculate wrapped phase. A quality guided phase unwrapping method is adopted and

improved. Global and local surface fit based smoothing algorithms are developed to calculate displacements and strains.

Additionally, a hybrid method based on both intensity and phase information, optical/digital fringe multiplication (O/DFM), is also investigated and developed. O/DFM also uses a series of phase shifted fringe patterns and involves the steps of noise filtering, fringe multiplication, fringe centerline detection, fringe thinning, fringe order assignment, fringe order interpolation, and calculation of displacement and strain.

An automated strain analysis system based on the above techniques is developed as a Windows GUI-based software in the Experimental Stress Analysis (ESA) Lab. By the use of this system, fringe patterns can be processed and analyzed, and the full-field displacements and strains can be obtained effectively and accurately. The system is successfully applied for the residual stress characterization of plain weave textile, shrinkage measurement of concrete material and material property identification of laminate, etc.

CHAPTER 1
INTRODUCTION

Background

Acquiring data simultaneously at many points on the specimen is frequently needed for experiments in solid mechanics. Although conventional point-wise methods such as strain gauges, dial gauges and other mechanical or electrical devices, can measure physical parameters such as surface strain and displacement, they can only provide localized measurement. Large numbers of separate measurements are required to build up an overall picture of the physical parameters; however, when the required number of sensors exceeds 10^2-10^3 the cost typically becomes prohibitive. By contrast, moiré interferometry, can provide an attractive solution for many applications and can provide full-field information equivalent to more than 10^5 independent point-wise sensors. With moiré interferometry, the data are usually recorded in the form of two-dimensional (2D) fringe pattern. Sophisticated digital cameras with high spatial resolution, high temporal resolution, and high accuracy have been applied in replace of photographic plates.

Moiré interferometry is a laser-based optical technique that combines the concepts of optical interferometry and geometrical moiré. It has been widely applied for studies of composite materials, fracture mechanics, electronic packages, etc. because of its full-field displacement measurement capability, high displacement sensitivity, high spatial resolution, and high signal to noise ratio [1]. It is a non-contacting and whole-field method capable of measuring both normal and shear strain. A schematic of the moiré interferometry setup can be seen in Figure 1-1. Figure 1-2 shows one actual four-beam Moiré interferometer with a specimen placed in front of it.

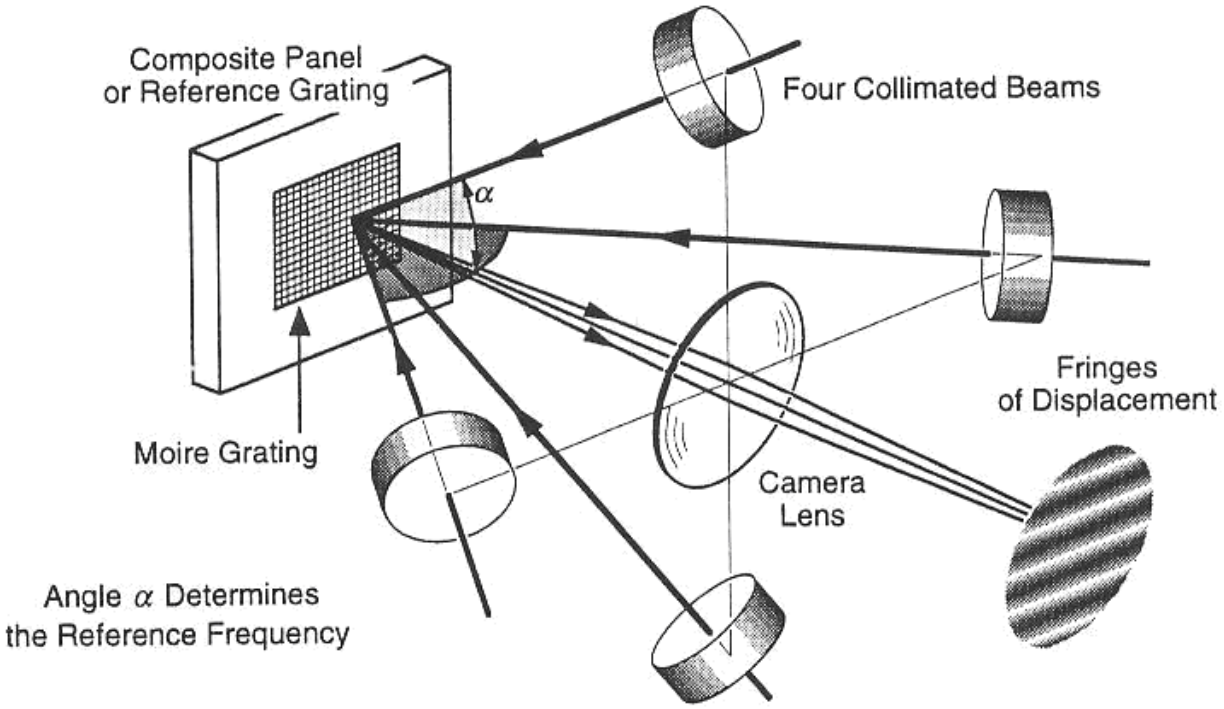

Figure 1-1. Four-beam Moiré Interferometer schematic

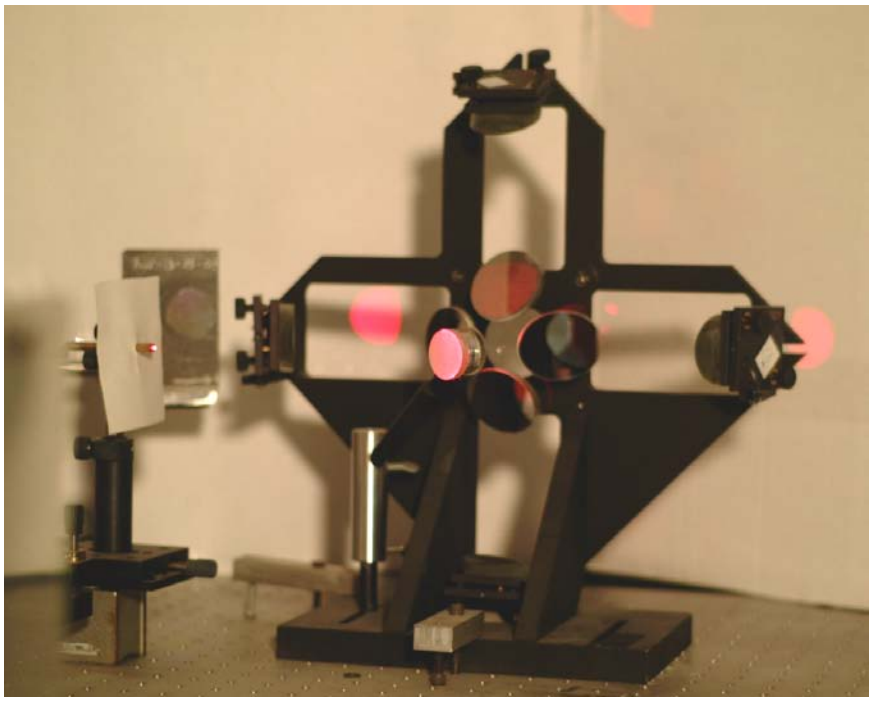

Figure 1-2. Four-beam Moiré Interferometer

Fringe patterns recorded via charge coupled device (CCD) camera are characteristic patterns of light and dark fringes as seen in Figure 1-3 which represent the intensity of the constructive and destructive interference of light. Mathematically the intensity can be expressed as Equation (1-1) [2],

$$I(x,y) = I_b(x,y) + I_m(x,y)\cos\left[\phi(x,y)\right] \tag{1-1}$$

where (x,y) is the coordinates of the pixel, $I(x,y)$ is the recorded intensity of each pixel (x,y), $I_b(x,y)$ is the background intensity, $I_m(x,y)$ is the fringe amplitude, and $\phi(x,y)$ is the phase which is a function of (x,y). $\phi(x,y)$ represents the fringe order $N(x,y)$ by $\phi(x,y) = 2\pi N(x,y)$.

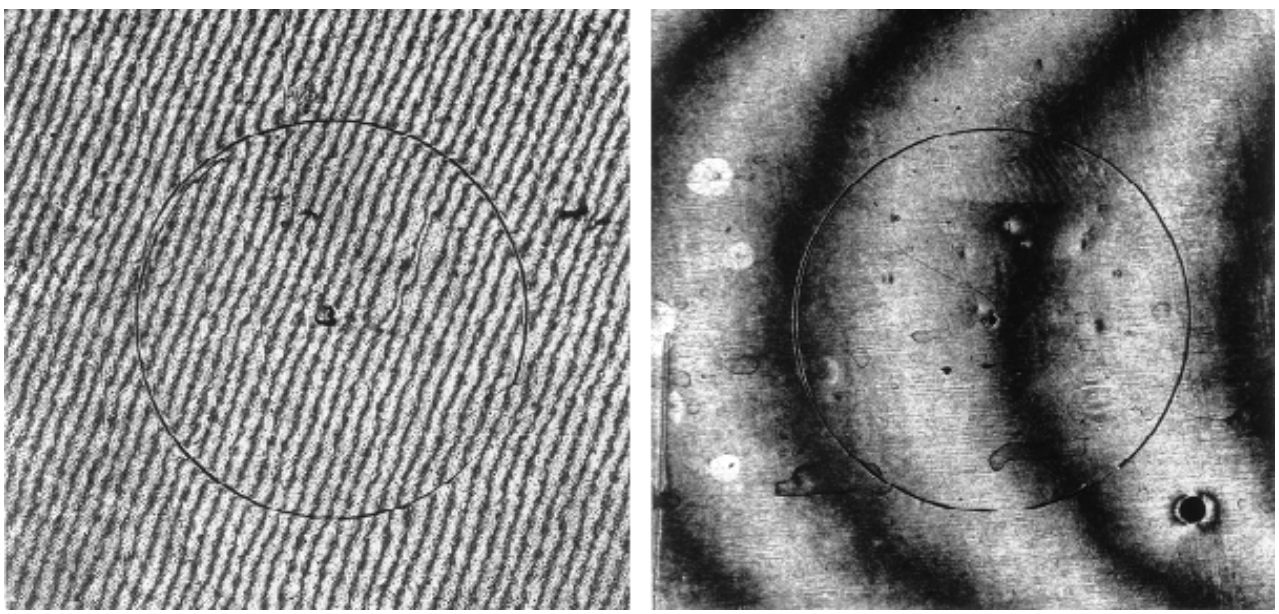

Figure 1-3. Typical fringe patterns (scribed circle is 1-inch diameter)

The relationship between fringe order and displacement is shown as in Equation (1-2),

$$\begin{cases} U(x,y) = \dfrac{1}{2f} N_x \\ V(x,y) = \dfrac{1}{2f} N_y \end{cases} \tag{1-2}$$

where $U(x,y)$ and $V(x,y)$ are the horizontal and vertical displacement fields. N_x and N_y are the fringe orders corresponding to the horizontal and vertical displacement fields. f is the specimen grating frequency.

Using the relationships between displacements and engineering strains, the strain can be approximated as shown in Equation (1-3).

$$\begin{cases} \varepsilon_{xx}(x,y) = \dfrac{\partial U(x,y)}{\partial x} \cong \dfrac{1}{2f}\dfrac{\Delta N_x}{\Delta x} \\ \varepsilon_{yy}(x,y) = \dfrac{\partial V(x,y)}{\partial y} \cong \dfrac{1}{2f}\dfrac{\Delta N_y}{\Delta y} \\ \varepsilon_{xy}(x,y) = \dfrac{1}{2}\left[\dfrac{\partial U(x,y)}{\partial y} + \dfrac{\partial V(x,y)}{\partial x}\right] \cong \dfrac{1}{4f}\left[\dfrac{\Delta N_x}{\Delta y} + \dfrac{\Delta N_y}{\Delta x}\right] \end{cases} \tag{1-3}$$

where $\varepsilon_{xx}(x,y)$ and $\varepsilon_{yy}(x,y)$ are the normal strains in x and y directions, $\varepsilon_{xy}(x,y)$ is shear strain, Δx and Δy are the lengths of gage lines (similar to strain gage) in x and y directions.

The traditional technique to analyze a fringe pattern is to manually count the numbers of fringes crossing the gage line and convert it to the displacement and strain information for discrete points [1]. Although this procedure can be duplicated often to obtain as many data points as possible, its disadvantages such as low efficiency and lack of full-field information limit its application. The term ‘automated strain analysis system’ refers to the process of converting these fringe patterns into maps representing the parameters of interest: displacement, strain distributions, for example via

implementation of mathematical algorithms on a digital computer. Based on the information hidden behind the fringe pattern, there are two basic methods to analyze fringe patterns. One is intensity-based method and another is phase extraction technique.

Literature Review

In the early days of interferometry, fringe pattern analysis was carried out manually. (Thomas Young [3] was presumably one of the first practitioners of fringe analysis when, in the early 1800s, he measured the spacing of interference fringes in order to calculate the wavelength of light.) During the 1960s, a number of electronic aids [4-5] to fringe analysis were developed. These devices allowed a substantial improvement in the accuracy with which fringes could be located within an interferogram but the overall analysis remained essentially manual.

During the last 30 years, the rapid development of digital image processing equipment has boosted the research on processing fringe pattern automatically. Based on the principle equation shown in Equation (1-1), the analysis of a fringe pattern can be achieved through the intensity or phase information. Automated fringe pattern analysis falls into two categories: one is intensity-based and another is based on phase extraction. Most early attempts at automated fringe pattern analysis are intensity-based [6-28] which is established based on the traditional manual processing method. It involves detecting and thinning fringe centerlines (fringe skeletons), assigning fringe orders and interpolating fringe orders. Although these intensity-based techniques are still sometimes used, methods based on phase extraction [29-67] have become more popular. They have significant advantages over the intensity-based methods [68]: data

are obtained over the full-field, not just at the fringe maxima and minima; the sign of the deformation is given; and immunity from noise is normally better.

Intensity-Based Analysis

The intensity-based fringe analysis method resulted from the traditional manual processing method [1]. In the traditional method, the gage lines are drawn on some points of the fringe pattern and the numbers of fringes crossing these lines are counted separately. Then the displacement and strain in these points can be estimated using Equation (1-2) and (1-3).

The matured intensity-based procedure includes detecting and thinning fringe skeletons, assigning fringe orders and interpolating fringe orders. Among them, fringe skeleton detection and fringe order interpolation are the core techniques. Two kinds of methods can be used to detect fringe skeletons. One method involves truncation and binarization of the fringe patterns [21]; another one is to find the fringe skeleton via detecting the local maxima or minima of fringe intensities [6, 12, 15-20, 28].

Although many techniques have been proposed and developed for detecting fringe centerlines, few studies can be found in the literature for fringe order assignment [10]. It is generally impractical to assign fringe orders automatically because the fringe patterns do not contain the fringe order information. One solution to this problem is to develop a semi-automatic method to assign the fringe order which requires the user to detect the ascending or descending directions of the fringe order while applying a small change of load in the experiment [69]. Because only the integral fringe orders along the fringe centerlines are assigned, fringe order interpolation is required to obtain fractional fringe orders at every pixel [11]. For fringe order interpolation, one-dimension (1-D) algorithms based on linear or quadric interpolation are available which are inadequate since the

fringe patterns contain two-dimensional (2-D) information. 2-D fringe order interpolation algorithms are needed to be developed and will be shown in chapter 2.

Phase Extraction Methods

When compared to the intensity-based methods which only use the information of fringe centerlines, phase extraction techniques use the full-field fringe information for the analysis. The phase extraction methods include Fourier transform method [29-41] and phase shifting method [42-67].

The most important advantage of using Fourier transform method to extract the phase information is that only one single fringe pattern is needed for the analysis. However, several practical drawbacks limit the application of this method [69]. The general Fourier transform method does not work for fringe analysis when the sign of fringe order gradient changes. Although adding carrier fringe could solve this problem, it increases difficulty in practice because the frequency of the carrier fringe must be controlled accurately. Another critical limitation of Fourier transform techniques is the lack of capability to handle discontinuities.

Phase shifting method is another technique widely used to extract the phase information easily and accurately. From the expression of Equation (1-1), one can see that it is in general impossible to obtain a unique phase distribution from a single fringe pattern because positive phases cannot be distinguished from negative ones without more information. The near-universal solution to this problem is to add to the phase function a known phase ramp which is linear to either time or position. Phase shifting method uses a series of fringe patterns with phase shifted to calculate the wrapped

phase, $\phi(x, y)$. It is ideal for fringe analysis; however, it also suffers from several problems such as phase unwrapping [70-94] and gradient (strain) calculation.

Phase Unwrapping

Inconsistent areas from noise, broken fringes and false fringes exist in most fringe patterns and bring difficulties to phase unwrapping. To overcome these difficulties, a number of phase unwrapping algorithms have been developed [70-94] in the past 20 years, and new phase unwrapping algorithms are still being proposed for various scientific images such as optical shape reconstruction, medical image analysis, geometrical survey, etc. Most of these algorithms are set for certain problems. Appropriate adoption or improvement of certain algorithms is necessary for the automated strain analysis system.

Itoh's method [70] is the simplest and fastest phase unwrapping procedure. However, if any of the pixels are masked or noise exists in the fringe pattern, the process will be interrupted or an error will propagate through subsequent data.

One class of algorithm to eliminate the effect from broken fringes is termed 'branch cut' method. These algorithms are based on the identification of the residues [71] in the wrapped phase data and balance them with branch cuts [71-72]. These algorithms are effective in repairing the broken fringes. An alternative technique is the so-called un-weighted least-squares phase unwrapping [76, 78], which was developed by the astronomy and synthetic-aperture radar signal processing community. The unwrapped phase map is chosen such that the local phase gradients match the wrapped gradients of the wrapped phase map in a least-squares sense. The algorithms above can

generally produce a correct solution; however, they are not able to distinguish false fringes from broken ones since their residues are identical.

The minimum spanning tree method [74, 94] divides the pixels into three groups: 1st group is all the unwrapped pixels (pixels whose phase have been unwrapped); 2nd group is the wrapped pixels with at least one neighboring unwrapped pixel; 3rd group is all other wrapped pixels. The next pixel to be unwrapped is from the 2nd group and should have the minimum phase difference with its unwrapped neighbor among the 1st group.

The preconditioned-conjugate-gradient (PCG) [76, 82] algorithm is the improved un-weighted least-squares method with the acceleration of the PCG by introducing weights. The weights are to zero-weight the regions of residues to prevent them from corrupting the unwrapped solution. PCG can offer good performance although it is much slower when compared to branch cut method or minimum spanning tree method.

Quality-guided phase unwrapping algorithm [73, 77, 83, 88] does not identify the residues at all. Rather than depending on branch cuts, it relies completely on a quality map [81] to guide the unwrapping paths. The quality map, can determine the “consistency” of each pixel from the wrapped phase. Phase unwrapping begins at a pixel and “grows” a region of unwrapped pixels, beginning with the highest-quality pixels and ending with the lowest-quality pixels. The algorithm is very successful and more efficient than the PCG method, however, it’s not guaranteed that the unwrapping paths will not encircle inconsistent areas and thereby introduce spurious discontinuities. So a good quality map is important to this algorithm. And new algorithms to detect and repair these inconsistent areas will be developed to improve the accuracy of the unwrapped

phase map. In practice, quality-guided phase unwrapping algorithm shows low efficiency for those large fringe patterns. It will be improved in the dissertation to increase its speed of phase unwrapping on large fringe patterns.

Some other algorithms, such as the Flynn's algorithm [80] and the L^p-norm algorithm [79], can also result in good performance for phase unwrapping of fringe patterns. However, these methods are less practical and are not discussed here.

Strain Calculation

In practice, there is often interest in the strain results which require differentiation of the displacement data (unwrapped phase). Generally the displacement or unwrapped phase field contains optical and electrical noise. The noise may not significantly affect the displacement field; however, it can result in large errors in strain calculation. Finite difference formulae are sensitive to the spacing (gage length) and normally insufficiently robust. It is necessary to filter the data by, for example, fitting low-order polynomials over a small region of the field [95-96] or by Fourier transform low-pass filtering [97]. The simplest method is a linear fit over a square sub-region [96]. Although these methods can calculate strain, many discontinuities were observed in practice in the ESA lab.

Fringe order gradient or strain can also be calculated via differentiating the polynomial function used in the 1-D fringe order interpolation [8, 11]. 1-D interpolation is effective and fast, however, the result from the interpolations along different directions (x and y direction) are different, which indicate it is not sufficient to capture the 2-D information. For simple and uniform fringe patterns, global 2-D polynomial interpolation may be used. However, for most real engineering problems, the global 2-D polynomial

interpolation is not enough to catch the full-field phase change due to the complex distribution of the displacement.

Strain calculation can also be done via finite element analysis [98-100]. In this method, the displacement fields are defined as the boundary condition of the finite element model. However, this method can be used only when the material properties are known. Its accuracy depends on the accuracy of the finite element model.

In this dissertation, methods based on the global and local surface fit are developed to calculate the strain efficiently with high accuracy. They can also be used for fringe order interpolation.

Objectives

The ultimate objectives of the dissertation include the development of the automated strain analysis system for Moiré Interferometry, and the applications of this system for different research projects in the ESA lab. In order to achieve the goal, the existing algorithms are investigated and improved, and new algorithms are developed. The following tasks will be completed in this dissertation:

- Investigation and selection of appropriate algorithms for fringe pattern analysis
- Improvement of the selected algorithms to increase efficiency and accuracy
- Experimental setup for phase shifting and calibration
- Development of new algorithms including detection and repair of inconsistent areas in phase map, and strain calculation via global and local surface fit
- Investigation and development of O/DFM method including fringe centerline detection/fringe multiplication/fringe thinning/fringe order assignment/fringe order interpolation/strain calculation from fringe order map

- Development of an expert software system for fringe pattern analysis
- Development of additional functions to assist fringe pattern analysis
- Applications of this software system in real projects

Selected original applications of this system will be completed in this dissertation:

- Residual stress characterization of plain woven composite
- Shrinkage measurement of concrete material
- Material property identification of laminate using full-field displacement measurement

CHAPTER 2
APPROACH

Pre-Processing of Fringe Pattern

The inherent optical noise of an interferogram is shown in Figure 2-1(A). The intensities along the red lines in the fringe pattern are also shown in the Figure 2-1(B) and they are roughly distributed. Although the back and white fringe gives good contrast, random noise with large amplitude is evident. The noise within the fringe pattern will affect the automated fringe analysis result which is shown in Figure 2-2. Appropriate noise filtering algorithms are needed to reduce the effect resulting from the random noise.

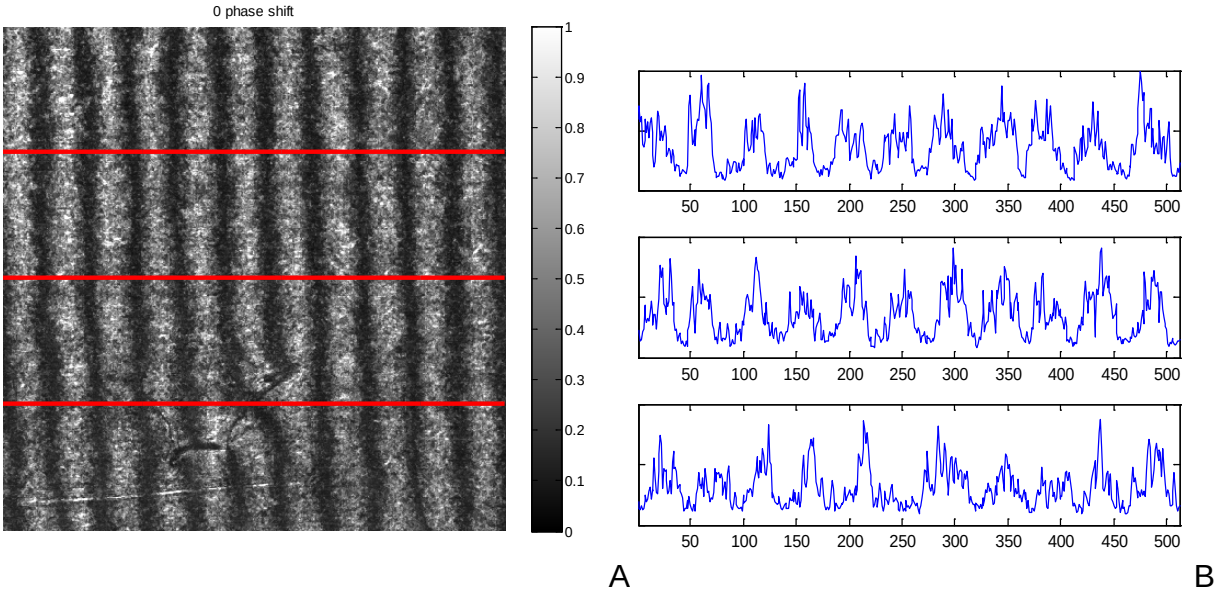

Figure 2-1. Illustration of large random noise existing in fringe pattern. A) Original fringe pattern. B) Intensity distribution along the lines

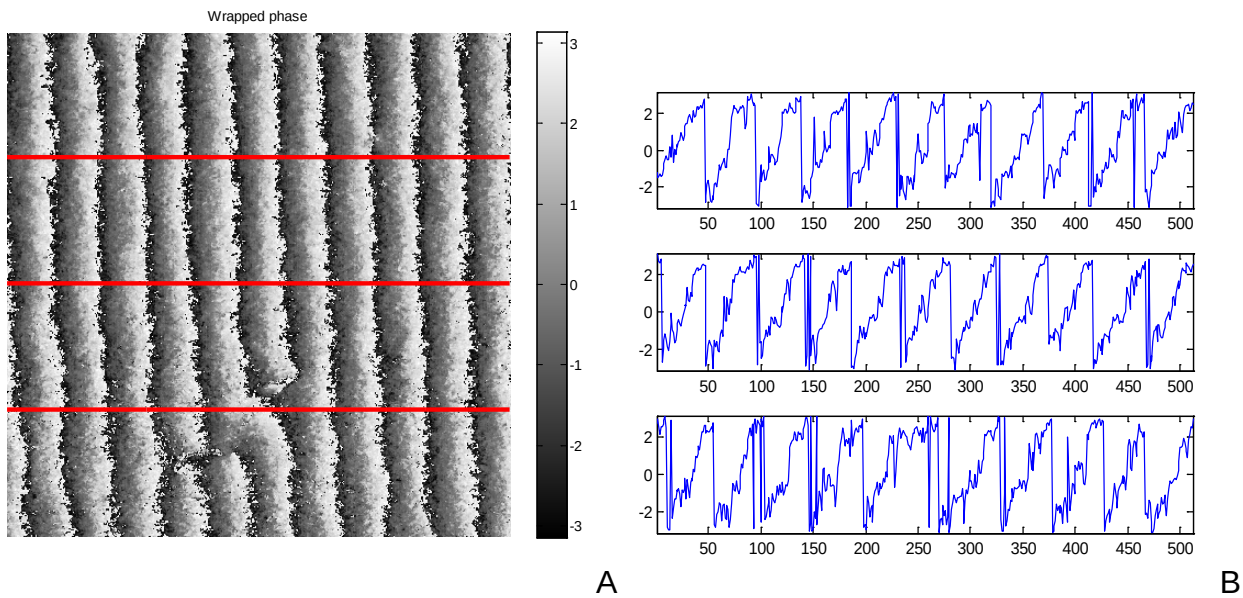

Figure 2-2. Illustration of large random noise existing in wrapped phase. A) Wrapped phase. B) Wrapped phase distribution along the lines

Noise filtering algorithms fall into two broad categories: spatial domain methods and frequency domain methods [101-102]. Spatial domain refers to the image plane itself, and approaches in this category are based on direct manipulation of pixels in an image. Frequency domain processing techniques are based on modifying the Fourier transform of an image.

Image Processing in the Spatial Domain

Spatial domain methods are procedures that operate directly on the pixels in the image as shown by the Equation (2-1).

$$g(x,y) = T\left[f(x,y)\right] \tag{2-1}$$

where $f(x,y)$ is the input image, $g(x,y)$ is the processed image, and T is an operator on $f(x,y)$, defined over some neighborhood of (x,y).

Spatial filtering works with the values of the image pixels in the neighborhood and the corresponding values of a sub-image (filter, mask, kernel, template, or window) that

has the same dimensions as the neighborhood. Figure 2-3 shows a 3x3 mask $w_{3\times3}$ and the 3x3 neighborhood of $f(x, y)$. The process consists simply of moving the filter mask from point to point in an image. At each point, the response of the filter at that point is calculated using a predefined relationship [101-102].

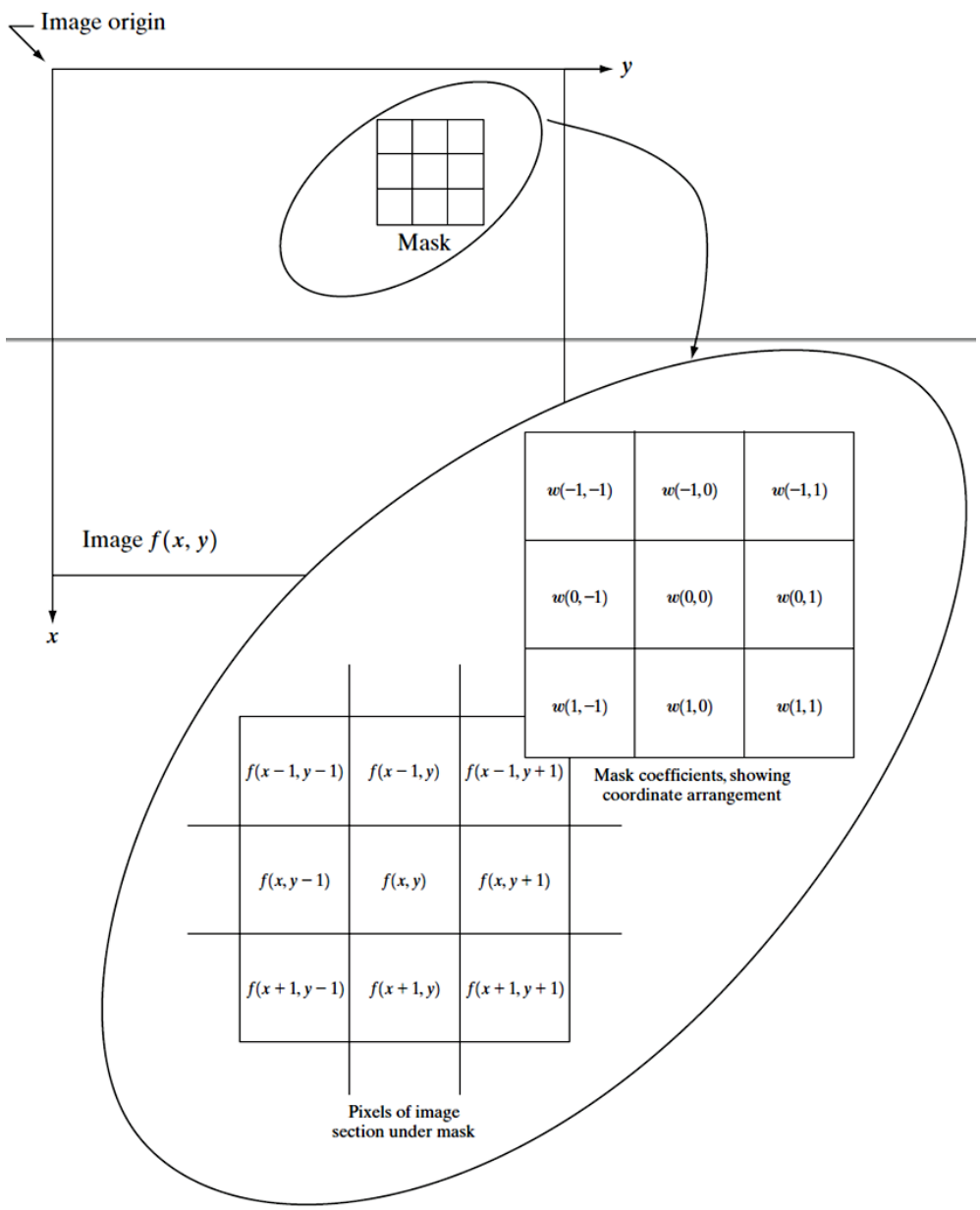

Figure 2-3. Spatial filtering. The magnified drawing shows a 3×3 mask and the image section directly under it

Smoothing linear filters

In general, linear filtering of an image of size $M \times N$ with a filter mask of size $m \times n$ is given by the Equation (2-2):

$$g(x,y) = \frac{\sum_{s=-a}^{a} \sum_{t=-b}^{b} w(s,t)\, f(x+s, y+t)}{\sum_{s=-a}^{a} \sum_{t=-b}^{b} w(s,t)} \tag{2-2}$$

where $a = (m-1)/2$ and $b = (n-1)/2$. $w(s,t)$ is the weight coefficient from the mask.

The output of a smoothing linear filter is the weighted average of the pixels within the neighborhood of the filter mask. These filters sometimes are called averaging filters.

Linear filters can remove the random noise very well. However, it can make the image look blurred. Thus it should be used carefully in practice.

Order-statistics filters

Order-statistics filters [101-102] are nonlinear spatial filters whose response is based on ranking the pixels within the image area encompassed by the filter, and then replacing the value of the center pixel with the value determined by the ranking result. Among all of the order-statistics filters, median filters are quite popular because they provide excellent noise-reduction capabilities, with considerably less blurring than linear smoothing filters of similar size.

Median filters are particularly effective in the presence of impulse noise, also called salt-and–pepper noise because of its appearance as white and black dots superimposed on an image. But it is not as good as averaging filter for random noise. The combination of median filter and averaging filter may give the better solution to

remove the impulse and random noise. And median filters are especially useful when discontinuities exist in the fringe patterns.

Image Processing in the Frequency Domain

Low frequencies in the Fourier transform are responsible for the general gray-level appearance of an image over smooth areas, while high frequencies are responsible for detail, such as edges and noise. The idea for the noise filtering in frequency domain comes from the removal or attenuation of the frequencies in the frequency domain. After the fringe pattern is converted into the frequency domain using Fourier transform as shown in Equation (2-3),

$$f(x,y) \rightarrow F(u,v) \tag{2-3}$$

The modification of the frequencies can be done directly using Equation (2-4),

$$G(u,v) = H(u,v)F(u,v) \tag{2-4}$$

The multiplication of H and F involves two-dimensional functions and is defined on an element-by-element basis. The filtered image is obtained simply by taking the inverse Fourier transform of $G(u,v)$.

Ideal low pass filters

The simplest low pass filter is a filter that “cuts off” all high-frequency components of the Fourier transform that are at a distance greater than a specified distance D_0 from the origin of the (centered) transform. Such a filter is called 2-D ideal low pass filter (ILPF) and has the transfer function as Equation (2-5).

$$H(u,v) = \begin{cases} 1 & \text{if } D(u,v) \le D_0 \\ 0 & \text{if } D(u,v) > D_0 \end{cases} \tag{2-5}$$

where D_0 is a specified nonnegative quantity, and $D(u,v)$ is the distance from point (u,v) to the origin of the frequency rectangle.

ILPFs are not very practical because of the severe occurrence of ringing [102] even when only 2% of the total power in the image was removed. This ringing behavior is a characteristic of ideal filters. Gaussian low pass filters are better to avoid this phenomena.

Gaussian low pass filters (GLPF)

The form of a 2-D GLPF is shown in Equation (2-6).

$$H(u,v) = e^{-D^2(u,v)/2D_0^2} \tag{2-6}$$

where D_0 is the cutoff frequency, and $D(u,v)$ is the distance from point (u,v) to the origin of the frequency rectangle. When $D(u,v) = D_0$, the filter is down to 0.607 of its maximum value. GLPF can avoid the occurrence of ring well and will be used frequently in practical.

Summary

Both spatial and frequency domain filters are effective in removing the random noise existing in a fringe pattern. But they have their own disadvantages. The wrapped phase obtained from 4 phase shifted fringe patterns which are filtered via 5×5 averaging filter and GLPF filter separately are shown in Figure 2-4 and Figure 2-5.

The comparison shows that GLPF filter can always result in cleaner wrapped phase map. But the frequency domain filter is difficult to apply to those fringe patterns with undefined values. So the choice of them depends on the specific problem at hand.

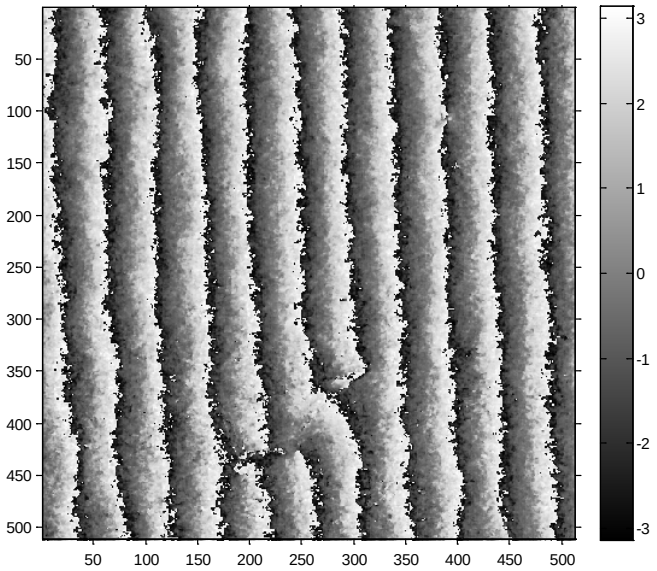

Figure 2-4. Wrapped phase map from 4 fringe patterns filtered via 5×5 averaging filter

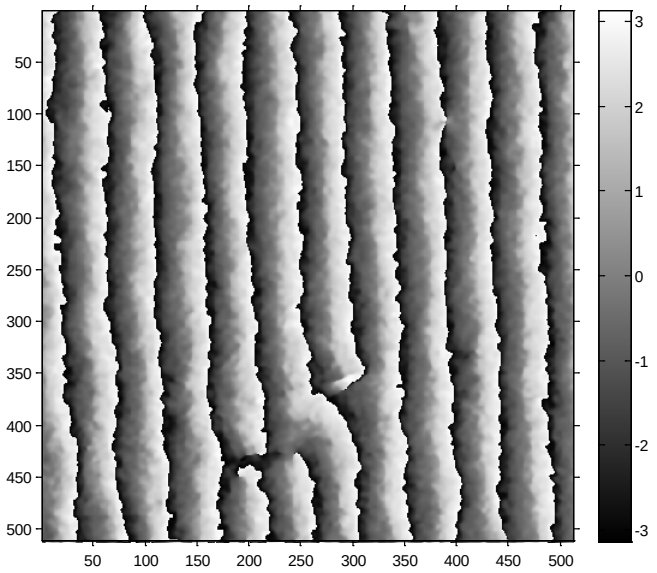

Figure 2-5. Wrapped phase map from 4 fringe patterns filtered via GLPF filter

Phase Shifting

Phase shifting is a method to extract phase information from fringe patterns. The following sections will cover aspects of phase shifting.

Theory of Phase Shifting

The main elements of a two-beam interferometer are shown schematically in Figure 2-6. Light from a coherent light source is divided into the two beams, 1 and 2, which travel along separate paths before being recombined. A photo detector array then measures the resultant intensity distribution. It is convenient to represent the complex amplitudes of the interfering beams as phasors, as shown in Figure 2-7, where a_1 and a_2 are the amplitudes and φ_1 and φ_2 are the phases of the two beams at a given pixel.

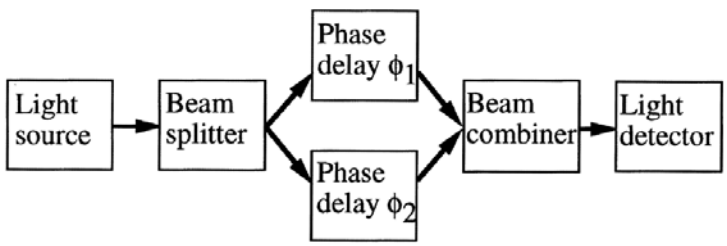

Figure 2-6. Generalized two-beam interferometer

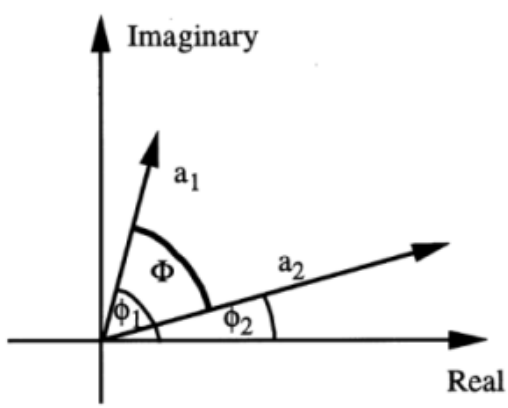

Figure 2-7. Phasor diagram

The pixel produces a signal, $s(x, y)$, which is proportional to the intensity of the light falling on to it and can be expressed as Equation (2-7),

$$s(x, y) = \left| a_1 e^{i\varphi_1} + a_2 e^{i\varphi_2} \right|^2 = a_1^2 + a_2^2 + 2a_1 a_2 \cos\varphi \qquad (2\text{-}7)$$

where $\varphi = \varphi_1 - \varphi_2$ is the difference in phase due to the differing optical path lengths encountered by the two beams. For simplicity, φ will be called phase in the later chapters and the intensity can be mathematically expressed as Equation (2-8),

$$I(x,y) = I_b(x,y) + I_m(x,y)\cos\left[\phi(x,y)\right] \tag{2-8}$$

where (x,y) is the coordinates of the pixel, $I(x,y)$ is the recorded intensity, $I_b(x,y)$ is the background intensity, $I_m(x,y)$ is the fringe amplitude, and $\phi(x,y)$ is the phase function.

From the expression of Equation (2-8), it's seen that it is generally impossible to obtain a unique phase distribution from a single fringe pattern. Positive phase cannot be distinguished from negative ones without more information. The solution to this problem is to add to the phase function a known phase ramp which is linear in either time or position as shown in Equation (2-9). If the added phase ramp $n\alpha$ is linear in time, it is called temporal phase shifting. If it is linear in position, it is called spatial phase shifting.

$$I(x,y) = I_b(x,y) + I_m(x,y)\cos\left[\phi(x,y) + n\alpha\right] \qquad (n = 0,1,2.....N-1) \tag{2-9}$$

where $n\alpha$ is the added phase ramp, N is the total number of fringe patterns with phase shifted, n is the order of the phase shifting pattern.

Phase shifting uses a series fringe patterns with shifted phase. And the output phase, $\phi(x,y)$, can be calculated using Fourier transform as shown in Equation (2-10).

$$\phi(x,y) = arctg\frac{\sum_{n=0}^{N-1} I_n(x,y)\sin(2n\pi/N)}{\sum_{n=0}^{N-1} I_n(x,y)\cos(2n\pi/N)} \tag{2-10}$$

For example, when $N = 4$, four fringe patterns with shifted phase $\pi / 2$ can be expressed as Equation (2-11),

$$\begin{cases} I_0 = I_b + I_m \cos\left[\phi(x,y)\right] \\ I_1 = I_b + I_m \cos\left[\phi(x,y) + \dfrac{\pi}{2}\right] = I_b - I_m \sin\left[\phi(x,y)\right] \\ I_2 = I_b + I_m \cos\left[\phi(x,y) + 2\dfrac{\pi}{2}\right] = I_b - I_m \cos\left[\phi(x,y)\right] \\ I_3 = I_b + I_m \cos\left[\phi(x,y) + 3\dfrac{\pi}{2}\right] = I_b + I_m \sin\left[\phi(x,y)\right] \end{cases} \tag{2-11}$$

The wrapped phase can then be calculated as Equation (2-12),

$$\phi(x,y) = \arctan \frac{I_3 - I_1}{I_0 - I_2} \tag{2-12}$$

In order to use phase shifting, the phase of the fringe pattern needs to be shifted by a certain value. A special stage for our interferometer was designed to add the phase ramp to the fringe pattern. At the same time, since the phase above is calculated via function arctan, it belongs to $[-\pi, \pi]$ and is called wrapped phase. The wrapped phase cannot be used to calculate displacement. A procedure of phase unwrapping is needed to convert the wrapped phase to the natural unwrapped phase.

Experimental Setup

The experimental setup for the phase shifting measurement is shown in Figure 2-8. It includes a moiré interferometer, stage, power supply, specimen grating, CCD camera and computer. The moiré interferometer is put on the stage which is controlled. When the stage moves, the fringe pattern is shifted and recorded via CCD camera which is controlled by software in the computer and can record fringe patterns continuously with some time interval.

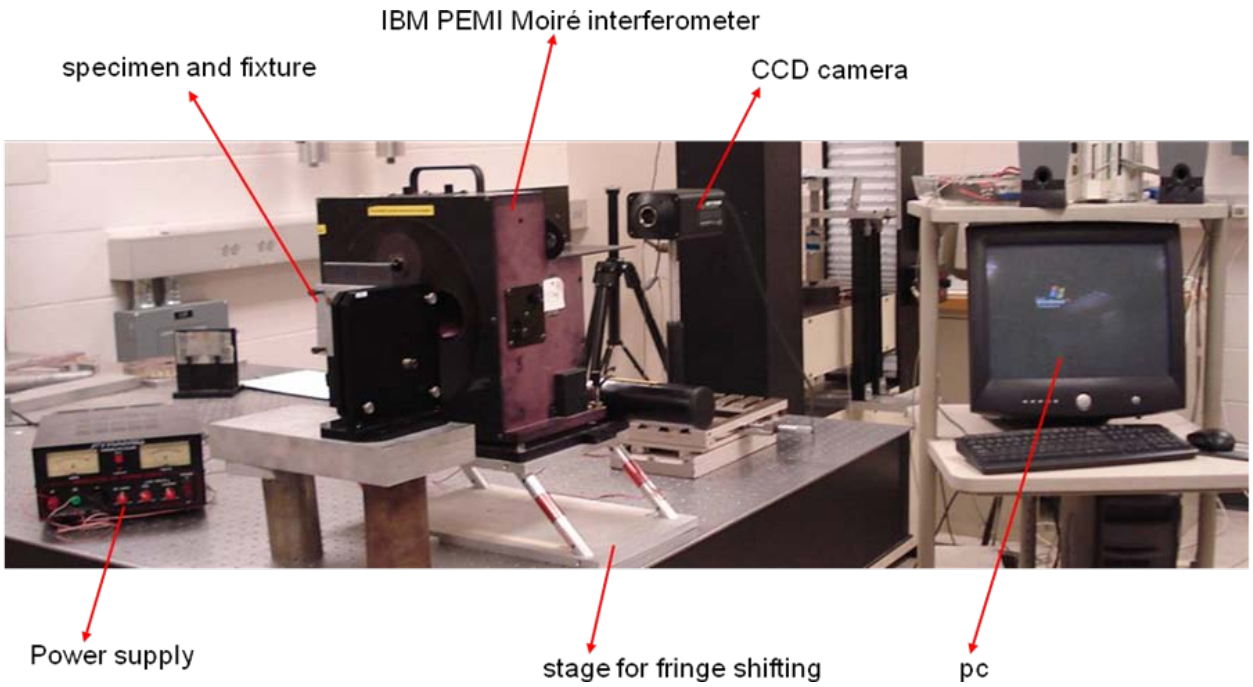

Figure 2-8. Setup for experiment

Stage for Phase Shifting

A stage for phase shifting was designed in the ESA Lab at the University of Florida [103]. As shown in Figure 2-9, the stage is composed of two aluminum plates and four aluminum tubes. The four tubes were precisely machined and attached to the bottom and top plates at 45°. Magnetic wires of 0.007'' diameter with special enamel coating for high temperature were wrapped exactly 200 times around the center of each of the four aluminum tubes then connected together with strain gage wire to complete the circuit. A 0~35 V, 0~5 A adjustable power supply, from Pyramid, model PS-32 lab was connected to the circuit. By turning the power ON and increasing the voltage, the current going through the magnet wire heats the aluminum tubes, which then expands, thus raising the interferometer in a 45° direction.

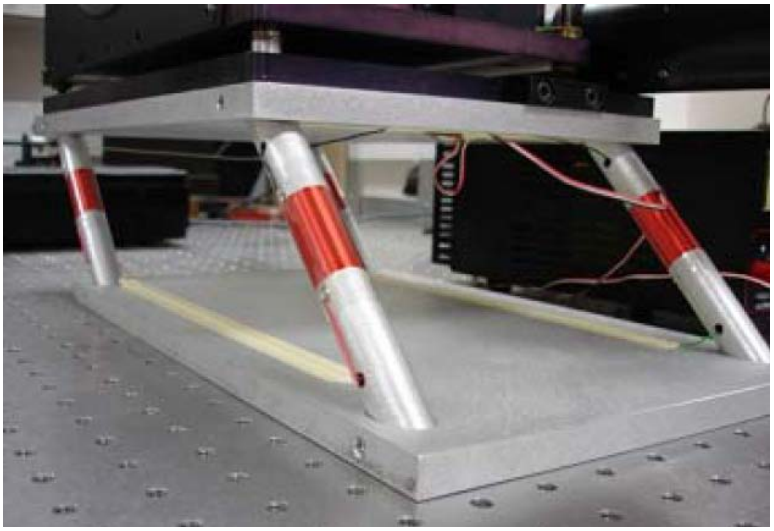

Figure 2-9. Stage designed for phase shifting

The stage was calibrated via a time-based calibration method. With a certain voltage (16V for our research) applied to the stage, the shifted fringe order and corresponding time was recorded via a high accuracy stop watch program. The plot of time vs. fringe shift number is illustrated in Figure 2-10. It showed that a linear shift existed for the low order fringe shifting. The average time for the first fringe shift is 4.230s. It is divided into several intervals depending on how many images were taken and used in the phase shifting procedure.

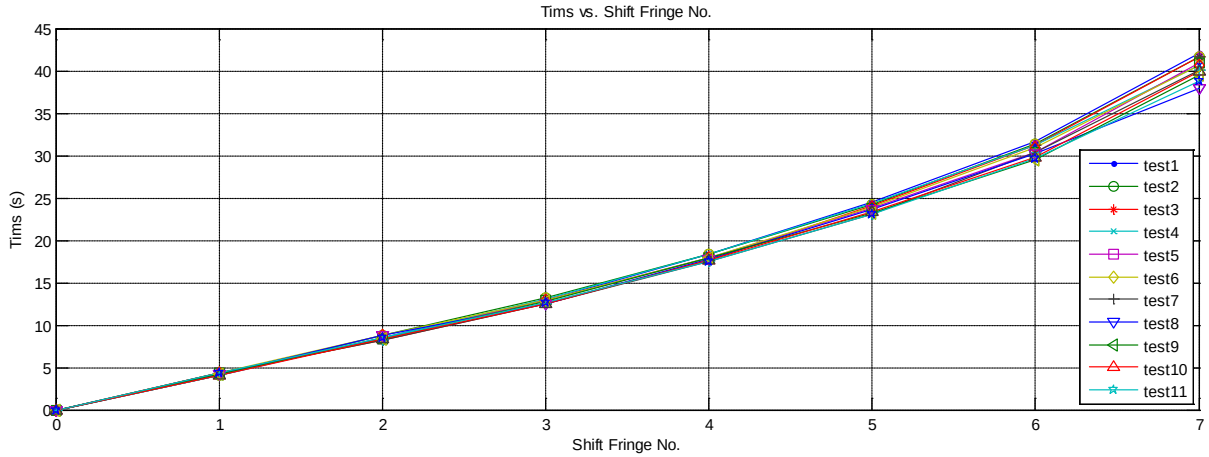

Figure 2-10. Calibration of the stage

Elimination of Miscalibration (N+1 Phase Shifting)

Error from miscalibration of the stage is unavoidable and it might bring significant systematic error to the phase shifting algorithm when the error from miscalibration is large. This error is called linear phase shift error and several approaches have been developed to reduce the influence of this type of error. Among these methods, one class of algorithm [104] is especially efficient since it requires only one extra sample (M=N+1) fringe pattern. This N+1 phase shifting algorithm will be incorporated into the automated strain analysis system.

Phase Unwrapping

Obviously the wrapped phase obtained from phase shifting belongs to $[-\pi, \pi]$ as shown in Figure 2-11. The wrapped phase information is not useful in obtaining the displacement information. The procedure to restore wrapped phase back to unwrapped phase is called phase unwrapping.

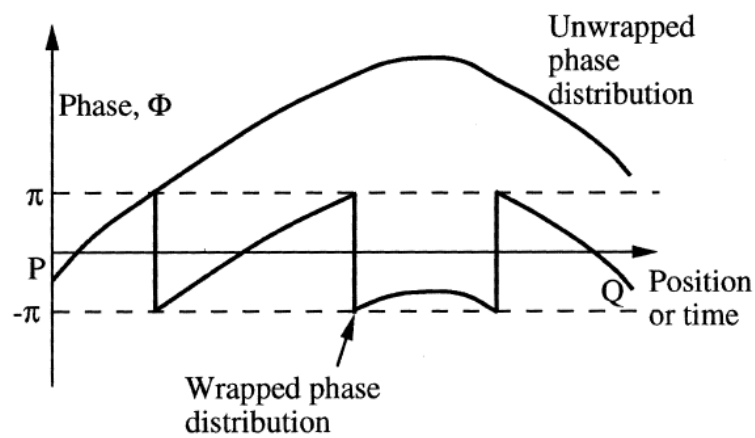

Figure 2-11. Wrapped phase and unwrapped phase

The relationship between wrapped phase and unwrapped phase can be expressed as Equation (2-13). Appropriate multiples of 2π are added to the wrapped phase at each pixel to make the phase map continuously distributed.

$$\phi(x,y)=\varphi(x,y)+2\pi k(x,y)=w\left[\varphi(x,y)\right] \tag{2-13}$$

where $\phi(x,y)$ is wrapped phase, $\varphi(x,y)$ is unwrapped phase and $w[\ ]$ is the wrapping operator.

Phase unwrapping methods have been extensively studied by numerous researchers. The most straight forward is Itoh's method [70].

Itoh's method

Itoh's method can be easily explained in one-dimension (1-D) as follows: $w[\ ]$ is the wrapping operator (defined by Equation (2-13)) that wraps the phase into the interval $[-\pi,\pi]$. Thus

$$w\left[\varphi(n)\right]=\phi(n)=\varphi(n)+2\pi k(n), \qquad n=0,1,\ldots,N-1, \tag{2-14}$$

where $k(n)$ is an array of integers chosen so that

$$-\pi<\phi(n)\le\pi \tag{2-15}$$

The difference operator Δ is defined as

$$\begin{aligned}\Delta\{\varphi(n)\}&=\varphi(n+1)-\varphi(n),\\ \Delta\{k(n)\}&=k(n+1)-k(n), \qquad n=0,1,\ldots,N-2,\end{aligned} \tag{2-16}$$

Computing the difference of wrapped phases using Equation (2-14) and (2-16) yields the Equation (2-17),

$$\Delta\left\{w\left[\varphi(n)\right]\right\}=\Delta\{\phi(n)\}=\Delta\{\varphi(n)\}+2\pi\Delta\{k_1(n)\} \tag{2-17}$$

Again apply the wrapping operator to the above result to obtain,

$$w\left\{\Delta\left\{w\left[\varphi(n)\right]\right\}\right\}=w\{\Delta\{\phi(n)\}\}=\Delta\{\varphi(n)\}+2\pi\left[\Delta\{k_1(n)\}+k_2(n)\right] \tag{2-18}$$

The subscripts on k_1 and k_2 are used to distinguish the integer arrays found by the two wrapping operations. The result of Equation (2-18) is the wrapped difference of wrapped phases. Because the wrapping operator w produces values in the interval $[-\pi, \pi]$, the requirement

$$-\pi < \Delta\{\varphi(n)\} \le \pi \tag{2-19}$$

implies that the term $2\pi\left[\Delta\{k_1(n)\} + k_2(n)\right]$ in Equation (2-18) must equal zero. Thus

$$\Delta\{\varphi(n)\} = w\left\{\Delta\left\{w\left[\varphi(n)\right]\right\}\right\} = w\left\{\Delta\{\phi(n)\}\right\} \tag{2-20}$$

which can be manipulated to yield the Equation (2-21),

$$\varphi(m) = \varphi(0) + \sum_{n=0}^{m-1} w\left\{\Delta\left\{w\left[\varphi(n)\right]\right\}\right\} \tag{2-21}$$

Equation (2-21) states that the phase can be unwrapped by integrating the wrapped difference of the wrapped phases. A simple one-dimensional phase unwrapping procedure based on Itoh's method is presented as the following algorithm. This procedure unwraps the phase in the array $\varphi(i), 0 \le i \le N-1$.

Table 2-1. Procedure of Itoh's method of phase unwrapping

Step	Features
Step 1	Compute the phase differences: $D(i) = \phi(i+1) - \phi(i)$ for $i = 0, ..., N-2$.
Step 2	Compute the wrapped phase differences: $\Delta(i) = \arctan\{\sin D(i), \cos D(i)\}$ for $i = 0, ..., N-2$.
Step 3	Initialize the first unwrapped value: $\phi(0) = \varphi(0)$
Step 4	Unwrap by summing the wrapped phase differences: $\phi(i) = \phi(i-1) + \Delta(i-1)$ for $i = 1, ..., N-1$

Figure 2-12 illustrates the obtained unwrapped phase using Itoh's method for the pixels along a line in a fringe pattern. Obviously the unwrapped phase is continuous and can be used to calculate displacement and other parameters.

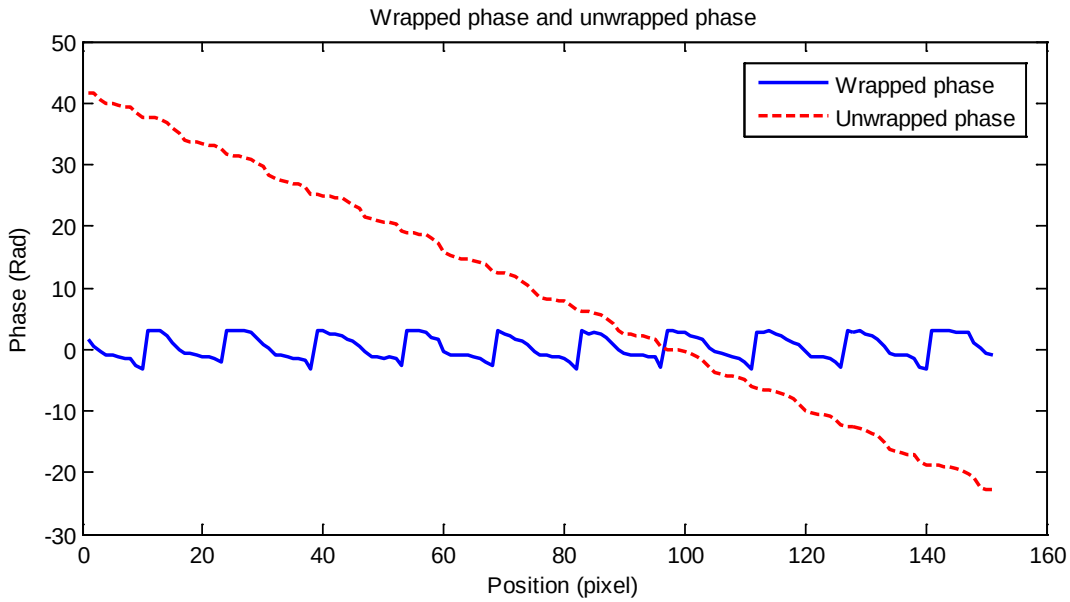

Figure 2-12. Wrapped phase and unwrapped phase

The concept above for one dimensional Itoh's method can be extended to two dimensional phase unwrapping. The phase unwrapping algorithm in two dimensions includes a row and a column search of the distribution first by solution of the horizontal discontinuities followed by the vertical ones.

Itoh's method is effective when the fringe patterns are in perfect condition and no broken fringes or false fringes exist. When broken or false fringes exit, Itoh's method will result in errors in the unwrapped phase. Figure 2-13 shows the unwrapped phase using Itoh's method for a two dimensional fringe pattern.

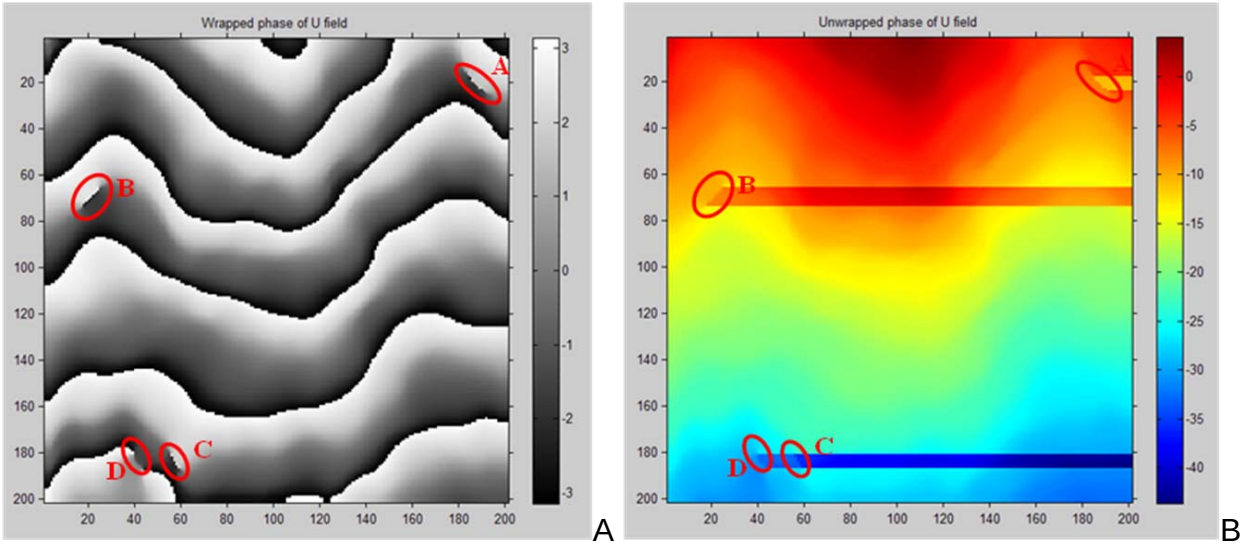

Figure 2-13. Wrapped phase and unwrapped phase. A) Wrapped phase. B) Unwrapped phase obtained using Itoh's method

The inconsistent areas such as broken fringes (D) and false fringes (A,B,C) shown in Figure 2-12A bring significant errors in the unwrapped phase which is shown in Figure 2-12B. A better phase unwrapping algorithm is needed to eliminate or limit the affects of these inconsistent areas.

As discussed in the literature review chapter, many other phase unwrapping methods, such as Flynn's minimum discontinuity method, cellular-automata method [80], minimum spanning tree method [94], and preconditioned-conjugate-gradient (PCG) least-square iteration [76, 82], can offer better performance. However, these methods are not practical because of their disadvantages which include an unstable result and inefficiency.

Quality guided phase unwrapping

The position of inconsistent areas can be determined via detecting and locating the residues. The calculation of residues is shown in Figure 2-14 and Equation (2-20).

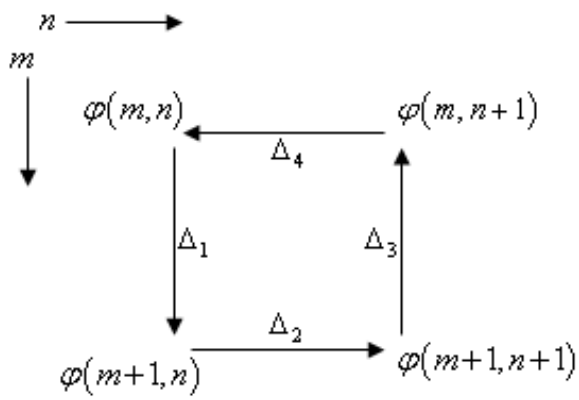

Figure 2-14. Integration direction of residue calculation

$$
\begin{aligned}
&\text{Residue} = \sum \Delta_i = \Delta_1 + \Delta_2 + \Delta_3 + \Delta_4 \\
&\textit{where} \\
&\Delta_1 = W\left\{\varphi(m+1,n) - \varphi(m,n)\right\}, \\
&\Delta_2 = W\left\{\varphi(m+1,n+1) - \varphi(m+1,n)\right\}, \\
&\Delta_3 = W\left\{\varphi(m,n+1) - \varphi(m+1,n+1)\right\}, \\
&\Delta_4 = W\left\{\varphi(m,n) - \varphi(m,n+1)\right\}, \\
&W \text{ is the phase wrapping operator.}
\end{aligned}
\tag{2-22}
$$

For the area without any residues, the integration of the gradient around a closed path should be zero. If the integration is not zero (-2π or 2π), it indicates there is a residue (negative or positive residue). Figure 2-15 shows the residues detected using the above method. When compared to Figure 2-13, the position of inconsistent areas and residues accurately agree.

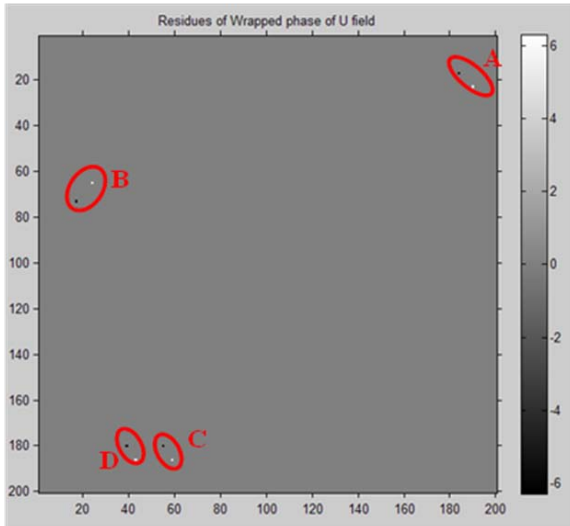

Figure 2-15. Residues detected

The residues will bring wrong -2π or 2π to some areas in the unwrapped phase when using Itoh's method which is shown in Figure 2-13. An advanced phase unwrapping algorithm is needed to eliminate the inconsistent areas or limit the expansion of the inconsistent areas.

The residues above can tell where the inconsistent areas are. The information is limited to the inconsistent areas only. Another parameter, quality map, can determine the "consistency" of each pixel from the wrapped phase. In a quality map, the areas with low quality represent unreliable phase data and vice versa. There are many quality maps [81, 93] available such as correlation, pseudo-correlation, phase derivative variance (PDV), etc. Among those quality maps, the PDV map can provide the best estimate of "consistency" of each pixel.

The PDV map is defined by Equation (2-23),

$$z_{m,n} = -\frac{\sqrt{\sum\left(\Delta_{i,j}^{x} - \overline{\Delta_{m,n}^{x}}\right)^2 + \sum\left(\Delta_{i,j}^{y} - \overline{\Delta_{m,n}^{y}}\right)^2}}{k \times k} \tag{2-23}$$

where k is the window size with center pixel (m,n), $\Delta^{x}_{i,j} = W\{\varphi(i,j+1) - \varphi(i,j)\}$, $\Delta^{y}_{i,j} = W\{\varphi(i+1,j) - \varphi(i,j)\}$, $\overline{\Delta^{x}_{m,n}}$ and $\overline{\Delta^{y}_{m,n}}$ are the averages of these partial derivatives in the $k \times k$ window.

Figure 2-16B shows the PDV quality map. Obviously in the quality map it is seen that there are several areas with low PDV values corresponding to the inconsistent areas in the wrapped phase map. When phase unwrapping procedure is performed, those pixels with lower PDV values should be unwrapped at the end.

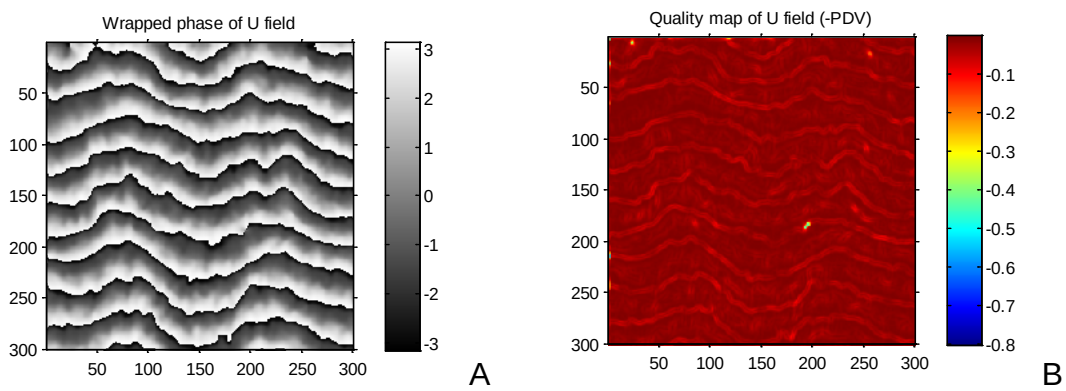

Figure 2-16. Wrapped phase map and its quality map. A) Wrapped phase map. B) PDV quality map

After the PDV quality map is obtained, the quality guided phase unwrapping algorithm can be realized. The procedure of this algorithm is summarized in Table 2-2.

Figure 2-17 shows a series images which represent the stage of Quality-guided phase unwrapping procedure.

Table 2-2. Procedure of quality guided phase unwrapping

Step	Features
Step 1	Calculate PDV map $z_{m,n}$ and create a binary mask of the same size. Set the value of each point in the mask as 0 (0 means this point is not unwrapped and 1 means it's unwrapped).
Step 2	Choose the pixel with maximum PDV value as the initial pixel and mark the corresponding point in the binary mask as 1, then put information of its neighboring pixels into array ii_adj, jj_adj (location), and qual_adj (quality value).
Step 3	Choose pixel (ii,jj) from array ii_adj, jj_adj, qual_adj with highest quality within the neighboring pixels, and put its neighboring pixels which has been unwrapped into temporary array ii_adj_temp, jj_adj_temp, qual_adj_temp.
Step 4	Determine the pixel (ii_base, jj_base) with the highest quality within the temporary array as the base point.
Step 5	Unwrap the phase of pixel (ii,jj) based on the neighboring pixel (ii_base, jj_base).
Step 6	Repeat steps 3-5 until all the pixels are unwrapped when array qual_adj_temp is empty.

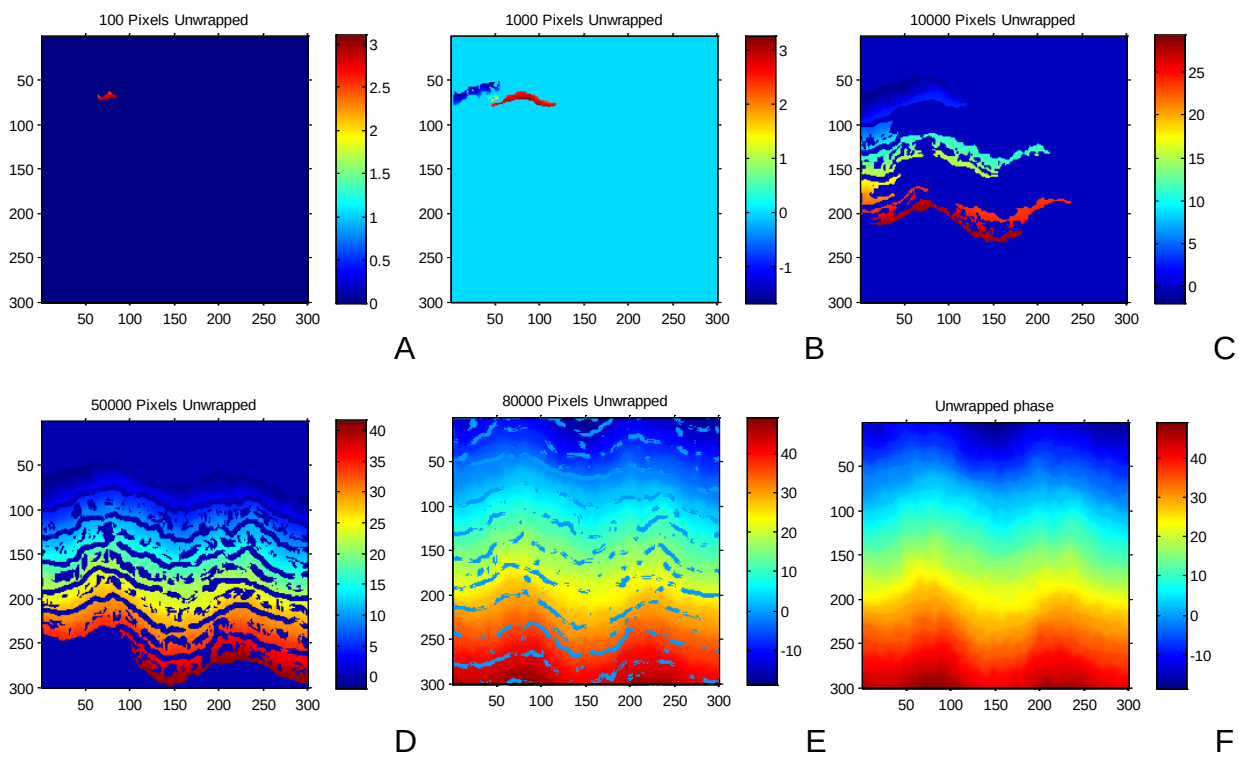

Figure 2-17. Process of Quality guided phase unwrapping. A) 100 pixels unwrapped. B) 1000 pixels unwrapped. C) 10000 pixels unwrapped. D) 50000 pixels unwrapped. E) 80000 pixels unwrapped. F) Final unwrapped phase

Phase unwrapping starts from the pixel with the highest quality and expands to other pixels according to the order of the quality. When compared Figure 2-17F to Figure 2-13B, it's seen that the improvement is significant and the affect of inconsistent areas is limited to a small region.

Improved quality guided phase unwrapping

The quality guided phase unwrapping method only relies on the quality map information. The error from inconsistent areas can be limited to a small area and will not propagate to the whole field. When compared to the Itoh's method, the improvement is obvious. Figure 2-18A and B show the unwrapped phase resulting from the Itoh's method and the quality guided phase unwrapping. It's seen that the unwrapped phase from the new algorithm is more accurate without streaks emanating from the inconsistent areas with low quality in the quality map. By the use of the new algorithm, the effect of those inconsistent areas is limited and can be attenuated via interpolation.

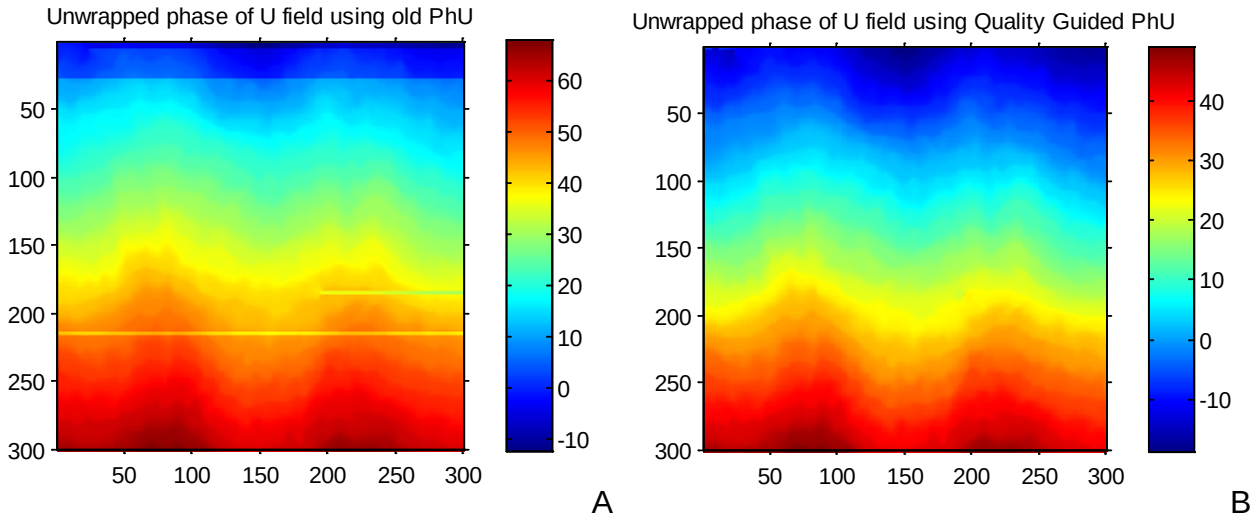

Figure 2-18. Unwrapped phase map. A) by Itoh's method. B) by quality guided phase unwrapping

The result from the quality guided phase unwrapping method is much better than the Itoh's method; however, it's very time-consuming in practice when applied to a large fringe pattern. Table 2-3 collects the CPU time for the program when applied to fringe pattern with different size. When the area is small, the speed of the program is very fast. For the area of 100×100 pixels the run time on a PC is less than 5 seconds. But for the area of 700×700 pixels, the run time increased significantly to about 2.5 hours. The efficiency of the program makes it impractical for large images.

Table 2-3. CPU time vs. image size

Image size (pixel*pixel)	CPU time (s)
100×100	4.7344
200×200	46.5469
300×300	259.4063
400×400	843.6094
500×500	2149.1
600×600	4277.6
700×700	8381.3

The solution to this problem is to first divide the large wrapped phase map into small areas, and then apply the quality guided phase unwrapping for each area separately. After all of the areas are unwrapped, they can be connected using boundary pixels.

Figure 2-19A and B show a test on the improved procedure. The 785×785 pixels wrapped phase is divided into small areas and each area is unwrapped separately as shown in Figure 2-19A. Obviously the whole unwrapped phase is not continuous. A procedure of connecting the separate areas is utilized and the final unwrapped phase is shown in Figure 2-19B.

Table 2-4. Improved procedure of quality guided phase unwrapping

Step	Features
Step 0	**Divide large wrapped phase map into small areas and do the PhU for each area separately**
Step 1	Calculate PDV map $z_{m,n}$ and create a binary mask of the same size. Set the value of each point in the mask as 0 (0 means this point is not unwrapped and 1 means it's unwrapped).
Step 2	Choose the pixel with maximum PDV value as the initial pixel and mark the corresponding point in the binary mask as 1, then put information of its neighboring pixels into array ii_adj, jj_adj (location), and qual_adj (quality value).
Step 3	Choose pixel (ii,jj) from array ii_adj, jj_adj, qual_adj with highest quality within the neighboring pixels, and put its neighboring pixels which has been unwrapped into temporary array ii_adj_temp, jj_adj_temp, qual_adj_temp.
Step 4	Determine the pixel (ii_base, jj_base) with the highest quality within the temporary array as the base point.
Step 5	Unwrap the phase of pixel (ii,jj) based on the neighboring pixel (ii_base, jj_base).
Step 6	Repeat steps 3-5 until all the pixels are unwrapped when array qual_adj_temp is empty.
Step 7	**Connect all the separate areas using boundary pixels**

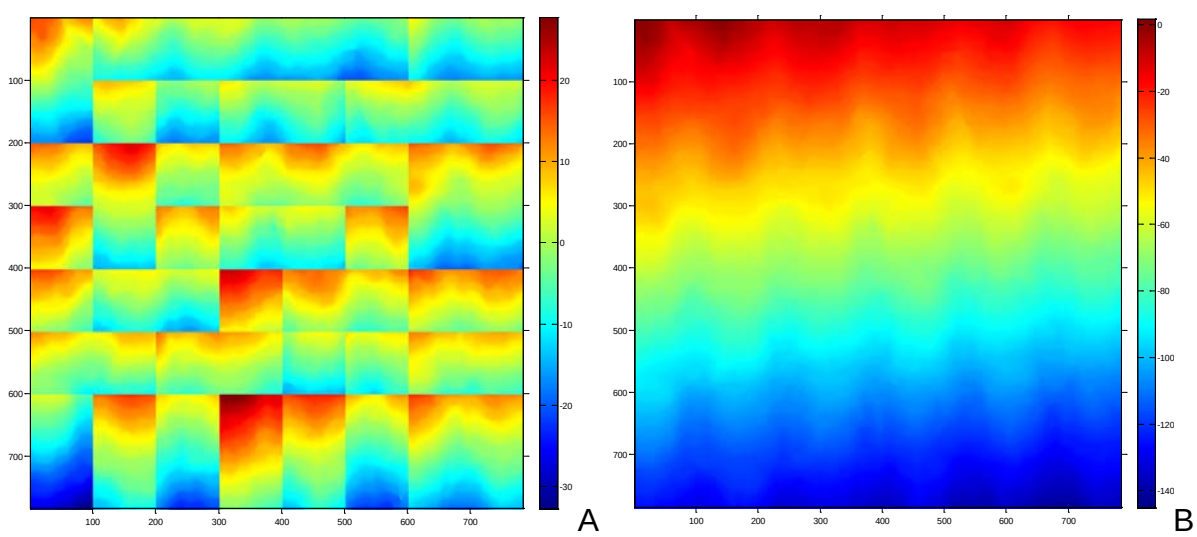

Figure 2-19. Unwrapped phase map. A) by Itoh's method. B) by quality guided phase unwrapping

The CPU time of unwrapping with for different division sizes is listed in Table 2-5.

The improvement of the speed is significant.

Table 2-5. CPU time vs. division size

Image size (pixel*pixel)	CPU time (s)
700×700	8381.3
785×785 (divided into 150×150 areas)	530.2656
785×785 (divided into 100×100 areas)	349.3125

Repair of inconsistent areas

Some research has been done to repair the broken fringe by placing branch cuts between the positive and negative residues [71-72]. However, it is hard to place branch cuts to the right residues since it is hard to detect the right pair of positive and negative residues. And it will also place branch cuts onto the residues from the false fringes. Few studies can be found in literature for false fringe detection and repair. A simple and effective method to detect and repair the false and broken fringes is developed.

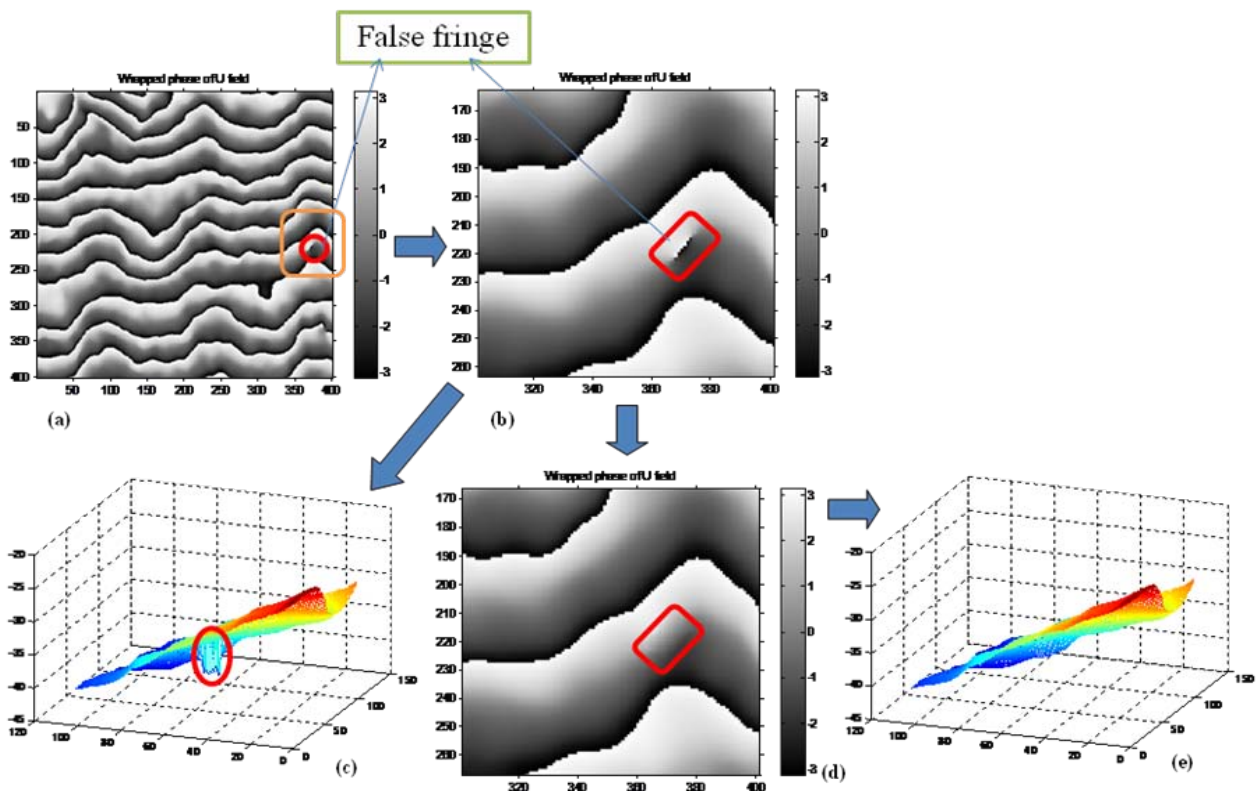

Figure 2-20. Removal of false fringe manually. A) Wrapped phase with false fringe. B) Zoomed in the area with false fringe. C) Unwrapped phase with big error around the false fringe. D) Wrapped phase after removal of false fringe. E) Unwrapped phase with false fringe removed.

Quality guided phase unwrapping can restrict the errors from inconsistent areas to a small area. Therefore these errors will not propagate to the whole field. However, it cannot attenuate the error from the inconsistent areas such as broken or false fringes. Figure 2-20A and B show the wrapped phase with a false fringe.

With quality guided phase unwrapping, the unwrapped phase of the zoomed area is shown in Figure 2-20C with phase jump clearly observed. As described previously, the errors caused by the false fringe are limited to the area around. These errors need to be removed or attenuated since they will cause huge errors for gradient (strain) calculation.

Eliminating the false or broken fringe can be done manually via selection of the area and do the interpolation of the area using the value around the area. Solving Laplace's equation within the area is used to interpolate the phase. The mathematical expression Laplace's equation is shown in Equation (2-24). $\varphi_0(i, j)$ is the phase of the points around the area selected. $\varphi(x, y)$ is the interpolated phase of the points within area. With the phase of the point in the boundary is given, the phase with distribution of Laplace's equation can be obtained. Figure 2-20D and E show the wrapped and unwrapped phase with the false fringe area selected and appropriately interpolated. When comparing the unwrapped phase in Figure 2-20C and E, the enhancement resulted from the false fringe elimination procedure is obvious.

$$\begin{cases} \dfrac{\partial^2 \varphi}{\partial x^2} + \dfrac{\partial^2 \varphi}{\partial y^2} = 0 \\ \varphi(i, j) = \varphi_0(i, j) \end{cases} \tag{2-24}$$

However, this manual selection of the areas is not practical and hard to control the dimension. An automatic method is developed to detect the inconsistent areas.

Detection of inconsistent areas

The unwrapped phase for Figure 2-13 A is shown in Figure 2-21A with 3 false fringes and 1 broken fringe. The residue map (Figure 2-13 B) and quality map (Figure 2-21B) shows the positions of the end points of these false and broken fringes.

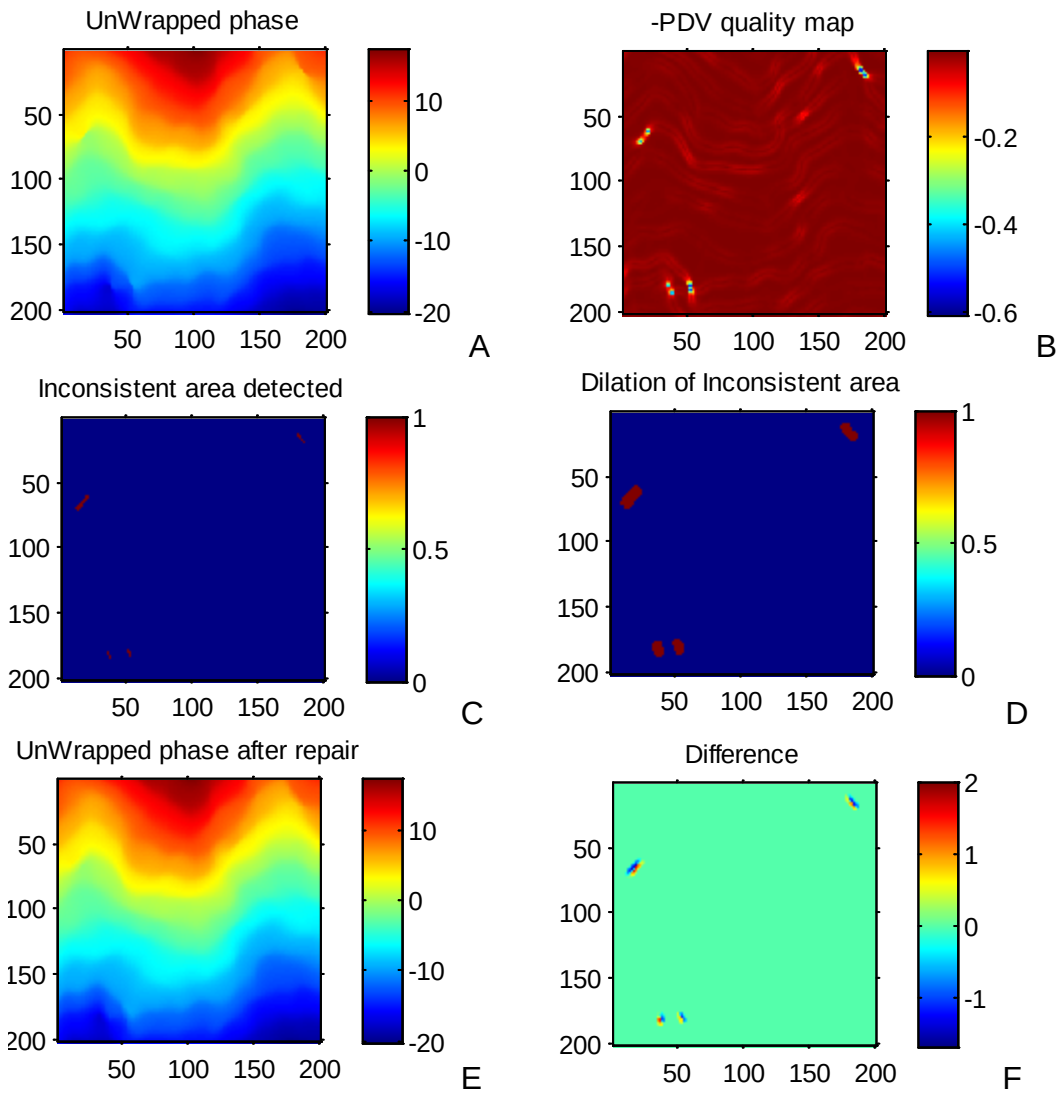

Figure 2-21. Detection and repair of inconsistent areas. A) Original unwrapped phase. B) Quality map. C) Inconsistent areas detected. D) Extended inconsistent areas. E) Repaired unwrapped phase map. F) Difference of unwrapped phase before and after repair

The false or broken fringes can be identified by detecting the consistency between the neighboring pixels in the unwrapped phase map obtained through quality guided phase unwrapping. For the consistent areas, the absolute phase difference between 2 neighboring pixels is very small (<0.3). However, for the inconsistent areas, the absolute phase difference is much larger (>1). This characteristic can be used to detect the pixels within the inconsistent areas. Starting from the left top corner to the right bottom corner, for each pixel P(i,j), only 3 directions as shown in Figure 2-22 need to be detected.

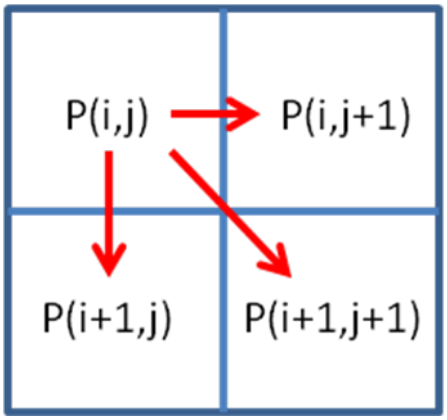

Figure 2-22. Detection of inconsistent areas

The inconsistent areas detected are shown in Figure 2-21C with a threshold value of 1.3. When comparing it with the residue or quality map, the positions of the false or broken fringes agreed well. Additional, this method has the ability to detect those areas with high noise.

After the inconsistent areas are detected, phase interpolation using Laplace's equation can be implemented within these areas. However, in order to obtain more trusted boundary pixels for the interpolation, the inconsistent areas can be extended several pixels via image dilation. Figure 2-21D shows the dilated inconsistent areas with 4 pixels extended.

Figure 2-21E shows the unwrapped phase map after repair of inconsistent areas. The difference of the unwrapped phase before and after repair is shown in Figure 2-21F. It's seen that the repairs only occur within the inconsistent areas with no affect to other pixels.

The procedure of detection and repair of inconsistent areas are briefly listed in Table 2-6.

Table 2-6. Procedure of detection and repair of inconsistent areas

Step	Features
Step 1	Perform quality guided phase unwrapping to obtain the unwrapped phase. And create the mask array with all 0 values.
Step 2	Calculate the absolute phase difference between neighboring pixels and compare it with the predefined threshold value. If it is larger than the threshold, these two pixels are marked as inconsistent pixels in the mask array with 1.
Step 3	Expand the inconsistent areas in the mask array with dilation.
Step 4	Interpolate the phase values within the inconsistent areas using Laplace's equation.

The automatic detection and repair of inconsistent areas locates them, removes the misrepresented phase values and interpolates them with reliable phase information from the boundary pixels. It can reduce the affect caused by the inconsistent areas such as false and broken fringes effectively. Therefore, it can improve the quality of the unwrapped map.

In practical applications, the automatic detection method may over detect the inconsistent areas. Currently, the solution is to have use interaction when necessary. Future improvement of this method is still needed.

Summary

Phase shifting is one of the phase extraction techniques. At least 3 phase shifted fringe patterns are required to calculate the phase information. A stage is designed to add a certain phase ramp to the fringe patterns. PDV quality map can measure the "goodness" of each pixel. Based on PDV map, quality guided phase unwrapping algorithm is adopted and improved to convert the discontinued wrapped phase to continuous unwrapped phase. The inconsistent areas can be detected. And Laplace's equation is used to interpolate the phase values within the inconsistent areas.

Displacement and Strain Calculation

The unwrapped phase can be easily converted to displacement via Equation (2-25). It's easily seen that the displacement filed distribution is directly proportional to the unwrapped phase distribution. When an in-plane displacement field is obtained using Equation (2-25), the corresponding strain field is often required to complete the deformation analysis. However, the existence of noise always makes it difficult to obtain a perfect strain result.

$$\begin{cases} U(x,y) = \dfrac{1}{2f}\dfrac{\phi_U(x,y)}{2\pi} \times 10^3 (\mu m) \\ V(x,y) = \dfrac{1}{2f}\dfrac{\phi_V(x,y)}{2\pi} \times 10^3 (\mu m) \end{cases} \tag{2-25}$$

Traditional Method

Based on the principles of moiré Interferometry, the strain distribution can be calculated from the full-field displacement field by Equation (2-25),

$$\begin{cases} \varepsilon_{xx}(x,y) = \dfrac{\partial U(x,y)}{\partial x} \cong \dfrac{10^6}{2f}\dfrac{\Delta\phi_U(x,y)}{2\pi\Delta x} \bullet scale \quad (\mu\varepsilon) \\ \varepsilon_{yy}(x,y) = \dfrac{\partial V(x,y)}{\partial y} \cong \dfrac{10^6}{2f}\dfrac{\Delta\phi_V(x,y)}{2\pi\Delta y} \bullet scale \quad (\mu\varepsilon) \\ \varepsilon_{xy}(x,y) = \dfrac{1}{2}\left[\dfrac{\partial U(x,y)}{\partial y} + \dfrac{\partial V(x,y)}{\partial x}\right] \cong \dfrac{10^6}{2f}\left[\dfrac{\Delta\phi_U(x,y)}{2\pi\Delta y} + \dfrac{\Delta\phi_V(x,y)}{2\pi\Delta x}\right] \bullet scale \quad (\mu\varepsilon) \end{cases} \tag{2-26}$$

where ε is the engineering strain, Δx and Δy are the gage lengths (pixels) along x and y direction, $scale$ is the conversion from image coordinates (pixels) to the real specimen dimension (mm).

Generally, the displacement or unwrapped phase field contains optical and electrical noise. The noise may not significantly affect the displacement field; however, it can result in large errors when calculating strain. The traditional method to calculate the strain map using gage selection is highly sensitive to the noise existing in the phase map. Gaussian Low Pass Filter may be used to attenuate the noise in the strain map [105]. At the same time, the gage length will also greatly affect the result.

A 4-point bending test was conducted here. The material is aluminum and the dimension of the specimen and the test scheme are shown in Figure 2-23A. The height of the specimen is 11.89mm. The fringe pattern taken for analysis is in dimension of 22.95mmx10.40mm. The dimension scale of the fringe pattern is 41.44pixels/mm. Figure 2-23B shows 4 consecutive fringe patterns for the U field of the specimen under 4-point bending condition with a line drawn in the position of y=10 pixels.

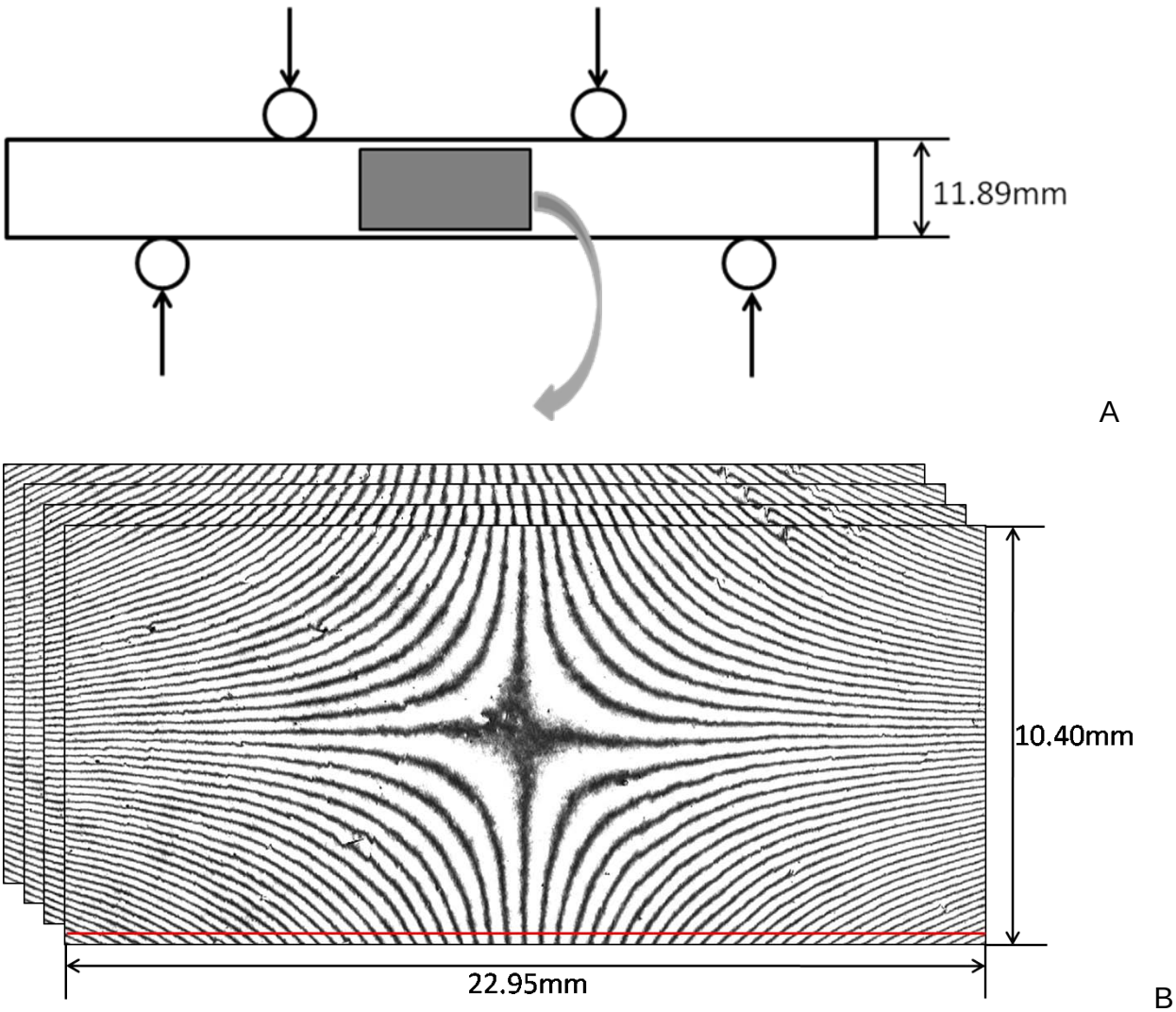

Figure 2-23. 4-point bending. A) Test scheme. B) 4 consecutive phase shifted fringe patterns

The traditional method to calculate strain was used with a gage length of 10 and 30 pixels respectively, and strains are illustrated in Figure 2-24A and B. Noise obviously exists in most areas. At the same time, the gage length selection affects the result. Generally, large gage length will smooth the result somehow, but still bring great noise into the strain maps as shown in Figure 2-24C. Based on the results in Figure 2-24, a better strain calculation method is needed and the technique based on surface fit can provide a better solution.

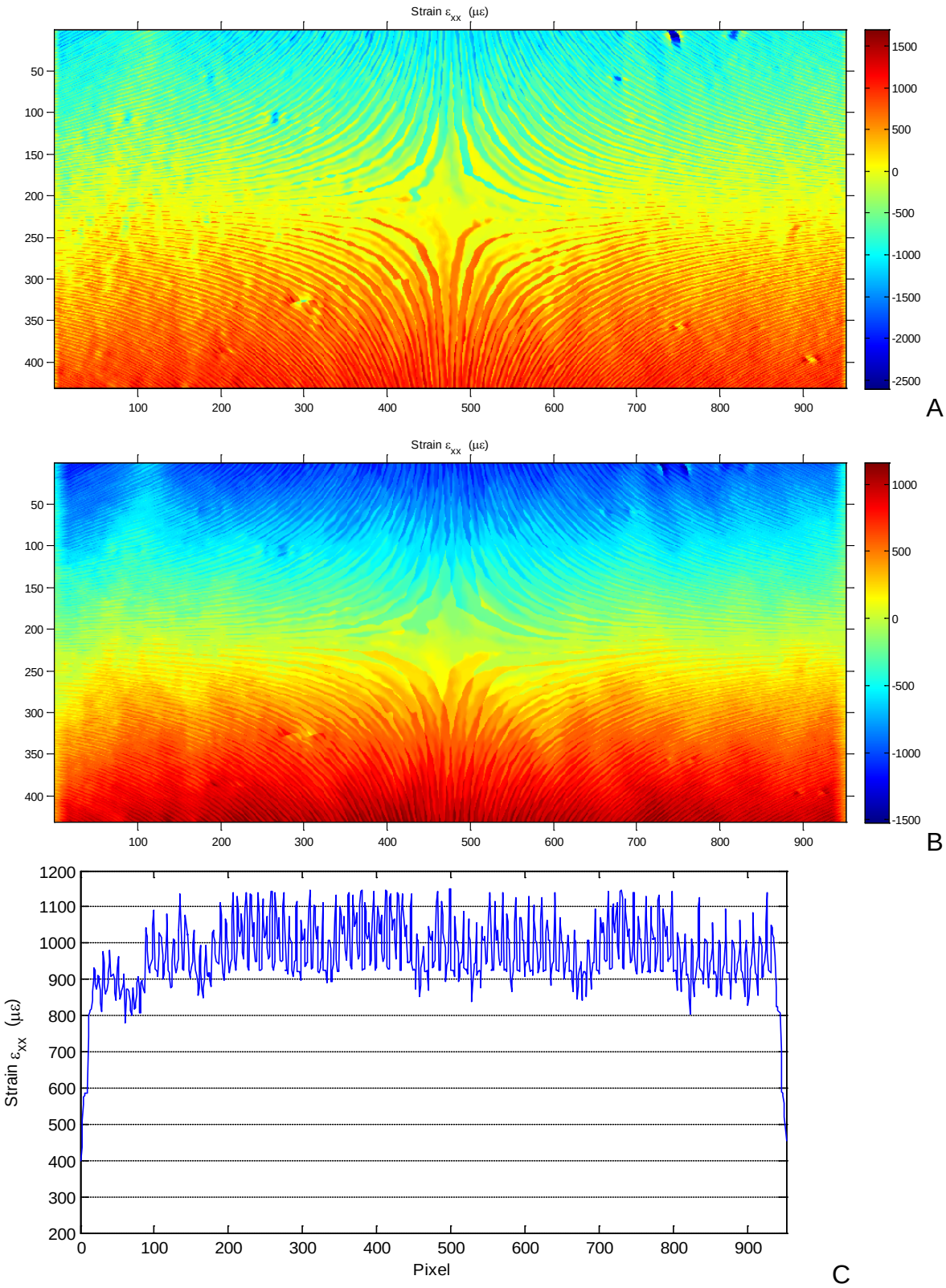

Figure 2-24. Calculation of normal strain ε_{xx}. A) Gage length = 10 pixels. B) Gage length = 30 pixels. C) Strain along y=10 pixels

Global Surface Fit Based Strain Calculation

Generally, the deformation of the specimen measured via moiré Interferometry is continuous, which indicates that the unwrapped phase, displacement, strain and stress should also be continuously distributed. However, the existing noise from an optical or electric device will break the continuity and bring significant error in strain calculation. Surface fit can attenuate the noise effectively. And most importantly, it can calculate gradient (strain) analytically. The Equation (2-27) shows the strain is proportional to the gradient.

$$\begin{cases} \varepsilon_{xx}(x,y) = \dfrac{\partial U(x,y)}{\partial x} = \dfrac{10^6}{2f2\pi} \bullet \dfrac{\partial \phi_U(x,y)}{\partial x} \bullet scale \quad (\mu\varepsilon) \\ \varepsilon_{yy}(x,y) = \dfrac{\partial V(x,y)}{\partial y} = \dfrac{10^6}{2f2\pi} \bullet \dfrac{\partial \phi_V(x,y)}{\partial y} \bullet scale \quad (\mu\varepsilon) \\ \varepsilon_{xy}(x,y) = \dfrac{1}{2}\left[\dfrac{\partial U(x,y)}{\partial y} + \dfrac{\partial V(x,y)}{\partial x}\right] = \dfrac{10^6}{2f2\pi}\left[\dfrac{\partial \phi_U(x,y)}{\partial y} + \dfrac{\partial \phi_V(x,y)}{\partial x}\right] \bullet scale \quad (\mu\varepsilon) \end{cases} \tag{2-27}$$

Some research papers implement a local surface fit technique to smooth the unwrapped phase field or displacement field. These techniques may obtain favorable result over small areas but the overall strain map is not continuous. Global surface fit algorithms are developed here to obtain more accurate strain information.

Thin plate splines (TPS) were introduced to geometric design by Duchon [106] and mainly applied to the area of computer and vision science [107-109]. The name thin plate spline refers to a physical analogy involving the bending of thin sheet metal. In the physical setting, the deflection is in the z-direction, orthogonal to the plane. In order to apply this idea to the problem of coordinate transformation, one interprets the lifting of the plate as a displacement of the x or y coordinates within the plane. Given a set of P corresponding points, the TPS warp is described by P+3 parameters which include 3

global affine motion parameters and P coefficients for correspondences of the control points. These parameters are computed by solving a linear system, in other words, TPS has closed-form solution.

The theory of thin plate spline is briefly reviewed below,

Let v_i denote the target function values at locations (x_i, y_i) in the plane, with $i = 1, 2, ..., P$. The TPS interpolant $\phi(x, y)$ minimizes the bending energy shown in Equation (2-28)

$$I_\phi = \iint_{R^2} \left(\phi_{xx}^2 + 2\phi_{xy}^2 + \phi_{yy}^2 \right) dxdy \tag{2-28}$$

And has the form

$$\phi(x, y) = a_1 + a_x x + a_y y + \sum_{i=1}^{P} w_i U\left(\left\| (x_i, y_i) - (x, y) \right\| \right) \tag{2-29}$$

where $U(r) = r^2 \log r$. In order for $\phi(x, y)$ to have square integrable second derivatives, it requires that

$$\begin{cases} \sum_{i=1}^{P} w_i = 0 \\ \sum_{i=1}^{P} w_i x_i = \sum_{i=1}^{P} w_i y_i = 0 \end{cases} \tag{2-30}$$

Together with the interpolation conditions, $\phi(x_i, y_i) = v_i$, this yields a linear system for the TPS coefficients:

$$\begin{pmatrix} K & P \\ P^T & O \end{pmatrix} \begin{Bmatrix} w \\ a \end{Bmatrix} = \begin{Bmatrix} v \\ 0 \end{Bmatrix} \tag{2-31}$$

where $K_{i,j} = U\left(\left\| (x_i, y_i) - (x, y) \right\| \right)$, the ith row of P is $(1, x_i, y_i)$, O is a 3×3 matrix of zeros, 0 is a 3×1 column vector of zeros, w and v are column vectors formed from w_i

and v_i, respectively, and a is the column vector with elements a_1, a_x, a_y. Denote the $(P+3)\times(P+3)$ matrix by L which is nonsingular [110], and denote the upper left $P\times P$ block of L^{-1} by L_p^{-1}, then it can be shown that

$$I_f \propto v^T L_p^{-1} v = w^T K w \tag{2-32}$$

When there is noise in the specified values v_i, one may wish to relax the exact interpolation requirement by means of regularization. This is accomplished by minimizing

$$H[\phi] = \sum_{i=1}^{n} \left(v_i - \phi(x_i, y_i)\right)^2 + \lambda I_\phi \tag{2-33}$$

The regularization parameter λ, a positive scalar, controls the amount of smoothing; the limiting case of $\lambda = 0$ reduces to exact interpolation. As demonstrated in [111], the TPS coefficients in the regularized case by replacing the matrix K by $K + \lambda I$, where I is the $p\times p$ identity matrix.

Figure 2-25 shows the normal strain via global surface fit. Obviously it's smoother than that in Figure 2-24. One limitation of global surface fit is the poor performance on those areas close to the edges perpendicular to the direction of strain calculated. This is due to the poor information extracted in these areas.

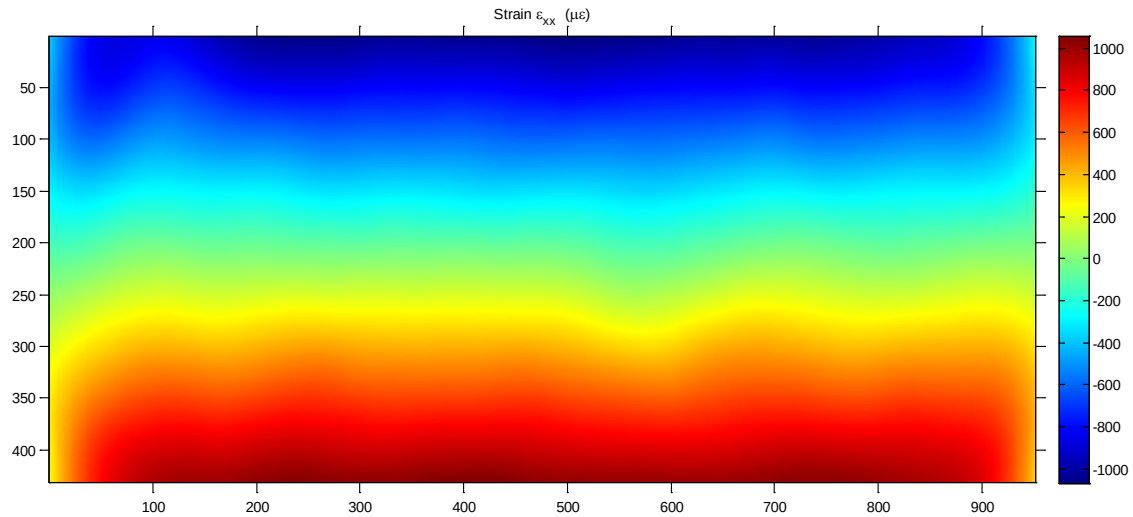

Figure 2-25. Normal strain ε_{xx} obtained via global surface fit.

Global surface fit using TPS is always better to calculate the strain map and obtain the smooth displacement map. It has a number of advantages: the interpolation is smooth with derivatives of any order; the model has no free parameters that need manual tuning; it has closed-form solution for both wrapping and parameter estimation; there is a physical explanation for its energy function. At the same time, one drawback of the TPS model is that its solution requires the inversion of a large, dense matrix of size P×P, where P is the number of points in the data set.

TPS is an effective tool for the global surface fit and gradient calculation. However, the solution requires the inversion of a $P \times P$ matrix, thus making it impractical for large scale application. One obvious solution to this problem is to use the subset of the data. A trade-off between the resolution and computational efficiency has to be made to obtain reasonable result for large images.

B-spline can also be used to construct the global surface fit. It is incorporated into the system as one option for the global surface fit. And in order to make use of all the data, local surface fit based strain calculation is developed.

Local Surface Fit Based Strain Calculation

Local surface fit based strain calculation method will first divide the unwrapped phase map into small patches. Surface fit is processed separately on each patch to obtain displacement and strain analytically from the expression of the surface fit. Then all the patches can be connected by the boundary points.

Low order polynomials such as bilinear, quadric or cubic function can be used to fit the 2D data within small patches. Here we illustrated the procedure of using quadric function. The format of bilinear and cubic can be found in appendix A and B. The unwrapped phase is assumed to have the quadric distribution within one patch as shown in Equation (2-34)

$$f\left(i,j\right)=c_1+c_2i+c_3j+c_4ij+c_5i^2+c_6j^2 \tag{2-34}$$

where $f\left(i,j\right)$ is the smoothed unwrapped phase. i,j is the image coordinate system with unit of pixel. c_1,c_2,c_3,c_4,c_5,c_6 are the coefficients calculated from the surface fit.

All the points within the patch of size $m\times n$ pixels are used to form the equation group,

$$\begin{cases} f_1\left(i_1,j_1\right)=c_1+c_2i_1+c_3j_1+c_4i_1j_1+c_5{i_1}^2+c_6{j_1}^2 \\ f_2\left(i_2,j_2\right)=c_1+c_2i_2+c_3j_2+c_4i_2j_2+c_5{i_2}^2+c_6{j_2}^2 \\ \ldots\ldots \\ f_{mn}\left(i_{mn},j_{mn}\right)=c_1+c_2i_{mn}+c_3j_{mn}+c_4i_{mn}j_{mn}+c_5{i_{mn}}^2+c_6{j_{mn}}^2 \end{cases} \tag{2-35}$$

$\left[B\right]_{mn,6}$, $\left[C\right]_{6,1}$ and $\left[Y\right]_{mn,1}$ matrix can be formed,

$$\left[B\right]_{mn,6}=\begin{bmatrix} 1 & i_1 & j_1 & i_1j_1 & i_1^2 & j_1^2 \\ 1 & i_2 & j_2 & i_2j_2 & {i_2}^2 & {j_2}^2 \\ & & \ldots\ldots & & & \\ 1 & i_{mn} & j_{mn} & i_{mn}j_{mn} & {i_{mn}}^2 & {j_{mn}}^2 \end{bmatrix} \tag{2-36}$$

$$[C]_{6,1} = \begin{Bmatrix} c_1 \\ c_2 \\ c_3 \\ c_4 \\ c_5 \\ c_6 \end{Bmatrix} \tag{2-37}$$

$$[Y]_{mn,1} = \begin{Bmatrix} f_1(i_1, j_1) \\ f_2(i_2, j_2) \\ \ldots\ldots \\ f_{mn}(i_{mn}, j_{mn}) \end{Bmatrix} \tag{2-38}$$

Then the coefficients can be calculated as,

$$[C] = \left[B^T B\right]^{-1} \left[B^T Y\right] \tag{2-39}$$

Finally the gradients (strains) can be calculated analytically as,

$$\begin{cases} \dfrac{\partial f}{\partial x} = \dfrac{\partial f}{\partial j}(i, j) = c_3 + c_4 i + 2c_6 j \\ \dfrac{\partial f}{\partial y} = -\dfrac{\partial f}{\partial i}(i, j) = -(c_2 + c_4 j + 2c_5 i) \end{cases} \tag{2-40}$$

The negative sign expression of $\partial f / \partial y$ comes from the opposite direction in image system and rectangular coordinate system.

Figure 2-26 shows the normal obtained with the local surface fit with 20x20 patch size and overlap 10. When compared to the result in Figure 2-24, the result from local surface fit is better and more accurate. When compared to the result in Figure 2-25, they agree well. The result from global surface fit is smoother in most areas. However, local surface fit can obtain more accurate results on areas close to the edges. This is because local surface can use all the pixels close to the edge to predict the strain.

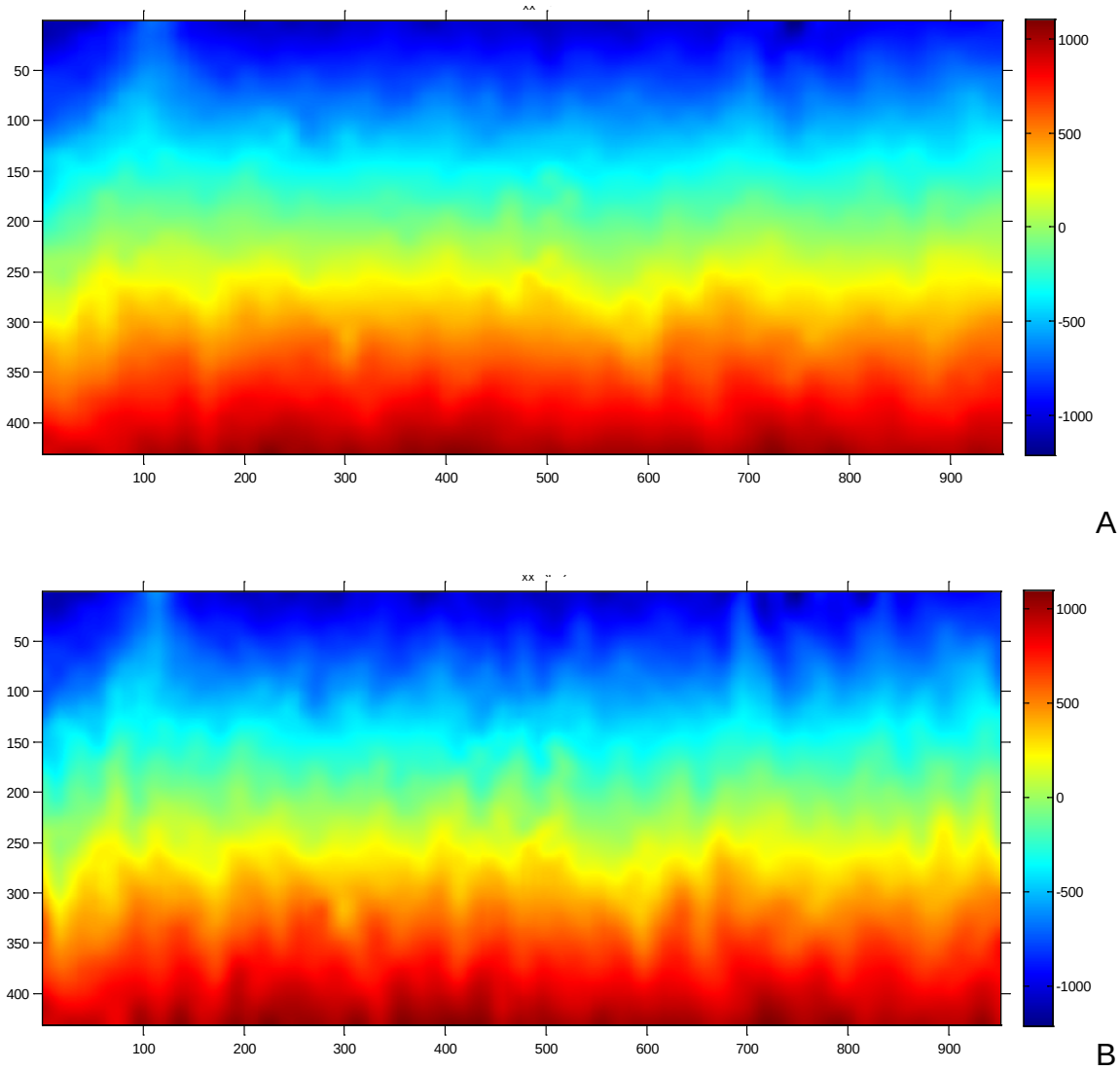

Figure 2-26. Normal strain ε_{xx} obtained via local surface fit. A) Quadric. B) Bilinear.

In real applications of local surface fit method, the selection of the function may affect the result a little as shown in Figure 2-26. All of these functions are incorporated into the system as options.

One big problem of using local surface fit is how to connect the patches smoothly. There are big variances of the strain values along the neighboring boundary. A procedure of overlapping between the neighboring patches and then calculating the average values within the overlapped areas is developed to attenuate the variance along the boundary. This procedure works well for most applications.

Summary

The traditional method to calculate the strain map is highly sensitive to the noise existing in the phase map. At the same time, the gage length will also greatly affect the result. The idea of using global surface fit technique to smooth the unwrapped phase map can attenuate the noise effectively. And most importantly, it can calculate gradient (strain) analytically. TPS was chosen for global surface fit because it is insensitive to noise in the data and it has high capability of constructing complex surface shapes. Theoretically, all of the pixels obtained in the CCD camera can be used in TPS surface fit to keep the spatial and strain resolution; however, the calculation of parameters of TPS may be time-consuming or even fail for large images. One obvious solution to this problem is to use the subset of the data, which will reduce spatial resolution somehow. A trade-off between the resolution and computational efficiency has to be made to obtain reasonable results for large images. Local surface fit using polynomial functions is also developed here to utilize all the pixels. Among the polynomial functions, the quadric function has the best performance. A procedure of overlapping is developed to reduce the discontinuity of the points along the boundary of each patch.

When comparing two methods, the data points along the line of y=10 pixel are extracted and plotted together in Figure 2-27. Since this is a 4-point bending test, the strain along y=10 is approximate 981 $\mu\varepsilon$ (average strain along the line y=10 calculated manually with 54 fringes within 22.95mm). The plot shows both methods can obtain more reliable strain values than traditional method as shown in Figure 2-24C for most areas with strain values close to the theoretical strain. The ranges of strain for most areas from global and local surface fit are (981 ± 30) and (981 ± 60) respectively, which

indicates that global surface fit can give smoother or more accurate strain calculation than the local surface fit method for most areas. However, local surface fit has better performance on those areas close to the edges. At the same time, the results indicate moiré has a better resolution of strain than other optical method such as digital image correlation which generally has strain resolution of $\pm 200\mu\varepsilon$.

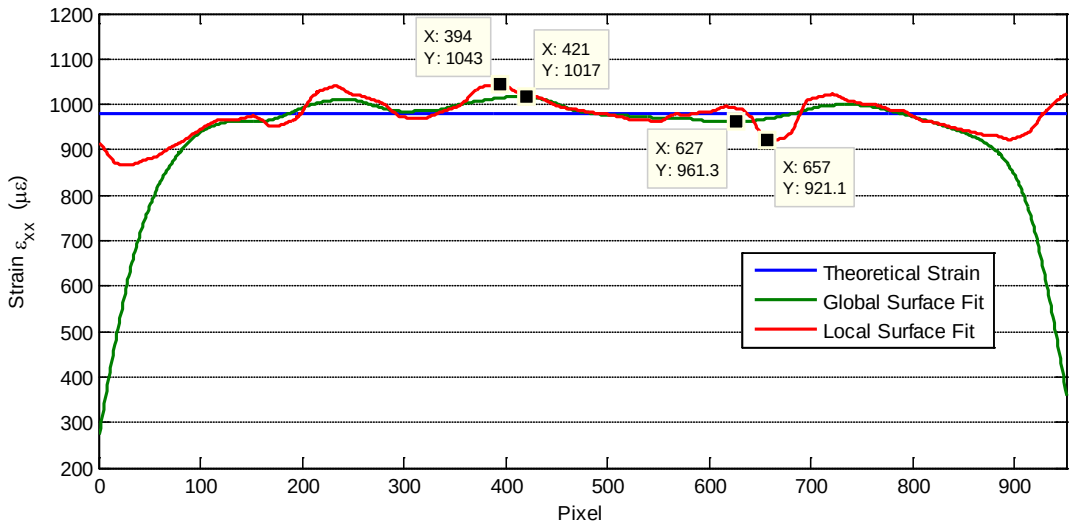

Figure 2-27. Plot of strain along y=10 pixels

Optical/Digital Fringe Multiplication (O/DFM) Method

The following sections will cover the procedure associated with the O/DFM method to analyze the fringe patterns.

Theory of O/DFM Method

O/DFM is an improved intensity based technique to analyze fringe patterns. In O/DFM, a series of N fringe patterns with phase shifting are used [1, 21]. For a series of N shifted fringe patterns, the phase of each moiré pattern is shifted by $2\pi / N$ relative to its neighbors. When N is an even number, the fringe patterns can be divided into two groups: the patterns of the first half and their complements. The intensity distributions of these two groups are shown in Equation (2-41),

$$\begin{cases} I_i(x,y) = I_b(x,y) + I_m(x,y)\cos\left[\phi(x,y) + \dfrac{2i\pi}{N}\right] \\ I_i^{\pi}(x,y) = I_b(x,y) - I_m(x,y)\cos\left[\phi(x,y) + \dfrac{2i\pi}{N}\right] \end{cases} \quad (i = 0,1,2.....\frac{N}{2}-1) \qquad (2\text{-}41)$$

where I_i is the intensity distribution of the ith shifted pattern which is shifted by $2i\pi / N$ with respect to the original pattern. I_i^{π} is the intensity distribution of the corresponding complementary pattern which is shifted by π with respect to the ith shifted pattern.

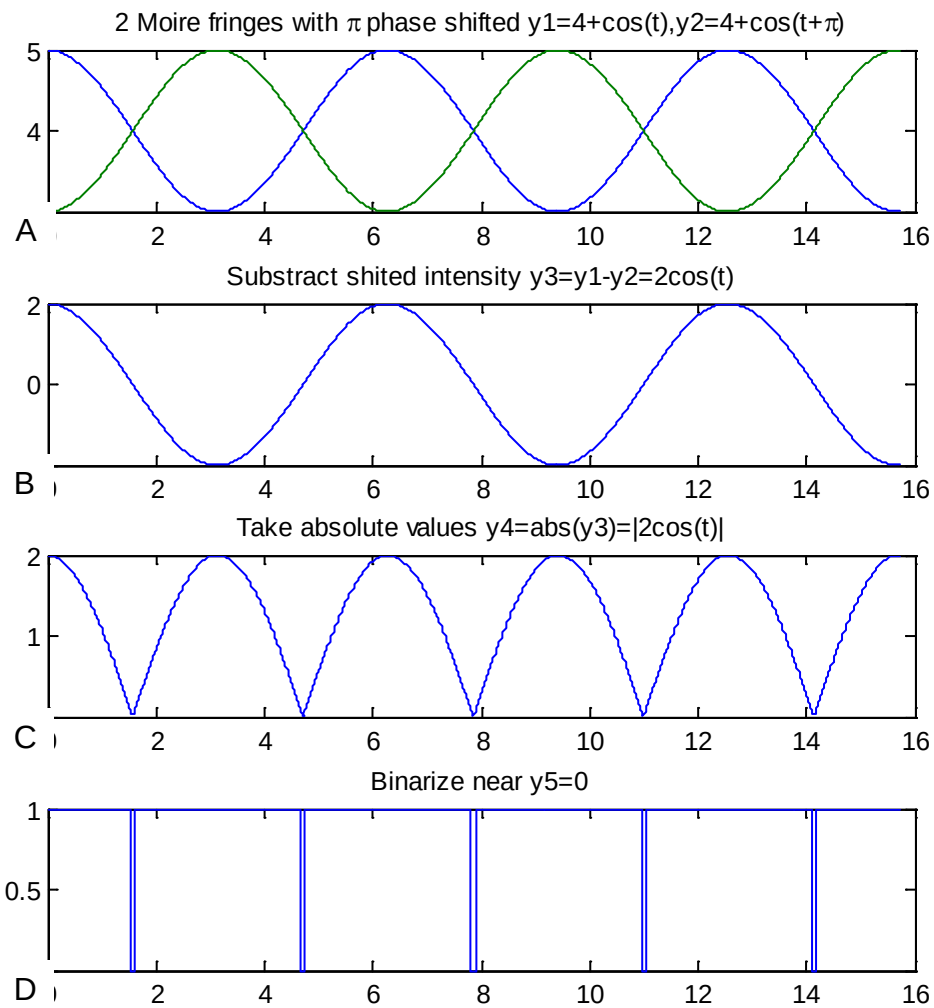

Figure 2-28. Explanation of O/DFM. A) 2 complementary fringes. B) Subtraction of each other. C) Absolute value of B). D) After binarizing

The complementary patterns are used in O/DFM method and explained in Figure 2-28. When the two complementary patterns are subtracted from each other at each point, as illustrated in Figure 2-28B. Then it takes the absolute values as illustrated in Figure 2-28C. The algorithm proceeds by truncating the data near 0 and binarizing intensities of 0 and 1 to points below and above the truncation value [13-14], respectively, as shown in Figure 2-28D. Obviously the result is a sharpened contour map that has twice as many contour lines as the number of fringes in the initial pattern. The sharpened contours occur at the crossing points of the complementary fringe patterns, where the intensities are equal. O/DFM method can provide N times fringe density than the original fringe pattern which will bring more accurate analysis result.

The O/DFM algorithm in this dissertation includes the following 5 steps; fringe skeleton detection, fringe thinning, fringe order assignment, fringe order interpolation, and strain calculation. 4 consecutive fringe patterns with $\pi/2$ phase ramp are used below for illustration.

Fringe Skeleton Detection

Because of the existence of noise in the fringe pattern, the binarizing procedure shown in Figure 2-28 generally does not work well. Figure 2-29 shows the skeleton detected using binarizing method for only 2 complementary fringe patterns $\left(\left|I_0 - I_1\right|\right)$. Obviously, the skeleton thickness is not uniform and in many places it is very thick.

Local minimum detection algorithm [6, 12, 15-20, 28] can provide a better solution to the fringe skeleton detection. In this algorithm, the fringe skeleton is represented as the local minimum pixels which can be found using the following procedure.

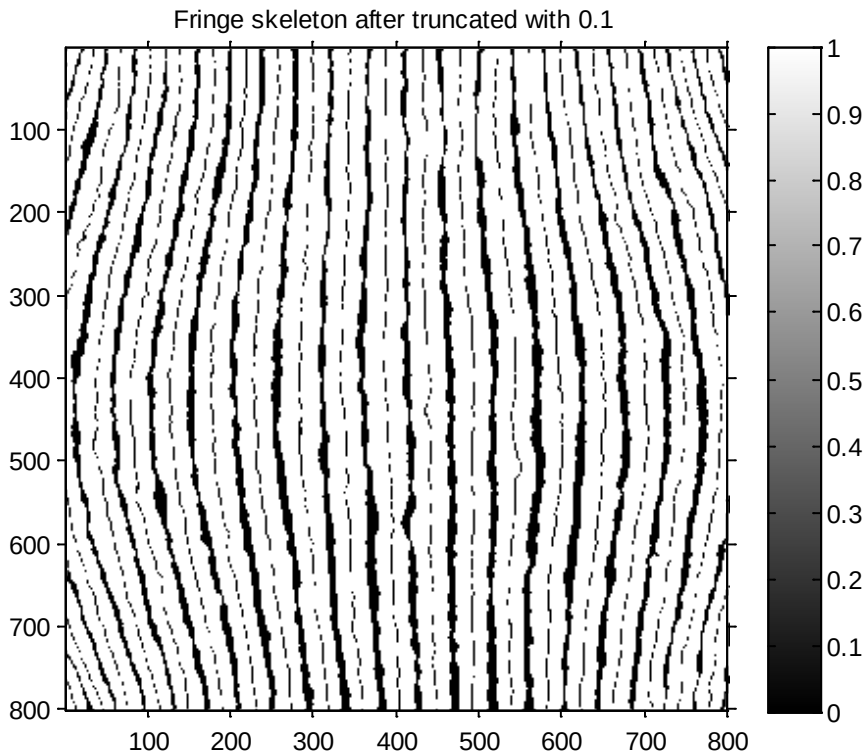

Figure 2-29. Fringe skeleton detected using binarizing method for $\left(\left|I_0 - I_2\right|\right)$

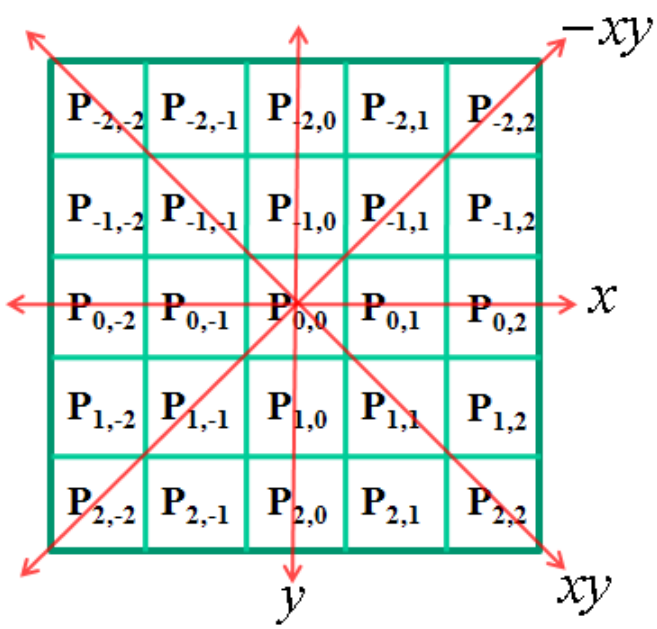

Figure 2-30. Fringe skeleton detected local minimum

Figure 2-30 shows the four directions which will be tested. $P_{i,j} \quad (i, j = -2, -1, 0, 1, 2)$ represents the intensity of the pixels around the center pixel $P_{0,0}$. The test of each direction is shown in Equation (2-40). If 2 of the above 4 conditions are satisfied, pixel $P_{0,0}$ is regarded as the local minimum pixel and its value is set to 0.

$$
\begin{aligned}
x \text{ direction: } & \begin{cases} P_{-1,0} + P_{0,0} + P_{1,0} < P_{-1,2} + P_{0,2} + P_{1,2} \\ P_{-1,0} + P_{0,0} + P_{1,0} < P_{-1,-2} + P_{0,-2} + P_{1,-2} \end{cases} \\
y \text{ direction: } & \begin{cases} P_{0,-1} + P_{0,0} + P_{0,1} < P_{2,-1} + P_{2,0} + P_{2,1} \\ P_{0,-1} + P_{0,0} + P_{0,1} < P_{-2,-1} + P_{-2,0} + P_{-2,1} \end{cases} \\
xy \text{ direction: } & \begin{cases} P_{1,-1} + P_{0,0} + P_{-1,1} < P_{2,1} + P_{2,2} + P_{1,2} \\ P_{1,-1} + P_{0,0} + P_{-1,1} < P_{-2,-1} + P_{-2,-2} + P_{-1,-2} \end{cases} \\
-xy \text{ direction: } & \begin{cases} P_{-1,-1} + P_{0,0} + P_{1,1} < P_{-2,1} + P_{-2,2} + P_{-1,2} \\ P_{-1,-1} + P_{0,0} + P_{1,1} < P_{2,-1} + P_{2,-2} + P_{1,-2} \end{cases}
\end{aligned}
\tag{2-42}
$$

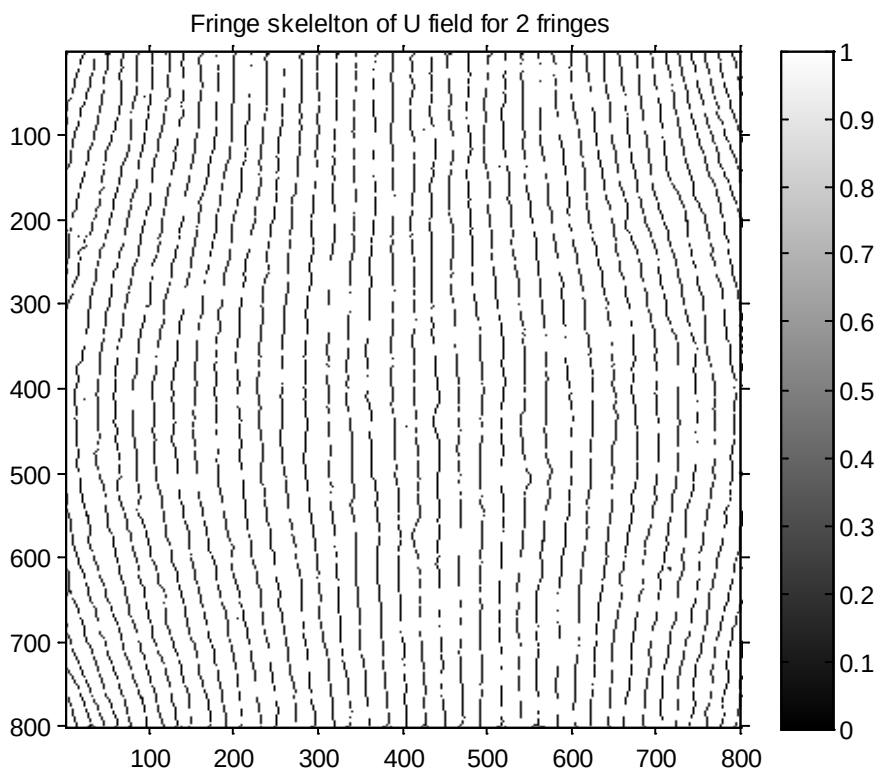

Figure 2-31. Fringe skeleton detected using local minimum detection method for $(|I_0 - I_2|)$

Figure 2-31 shows the fringe skeleton resulted from this method and obviously the skeleton is much thinner than that from binarizing procedure as shown in Figure 2-29.

Figure 2-31 also shows some isolate noise and the thickness of the skeleton is more than 1 pixel in most fringes. Appropriate fringe thinning algorithm is needed to obtain the best fringe skeleton.

Fringe Thinning

Generally, the fringe skeleton obtained from the binarizing or local minimum detection method is wider than the width of one pixel. Fringe thinning is the process to reduce the skeleton width and thus to obtain a true fringe skeleton [22-23, 112-113]. Figure 2-32 shows the fringe skeleton after thinning. When compared to Fig. 2-31, it's thinner and cleaner.

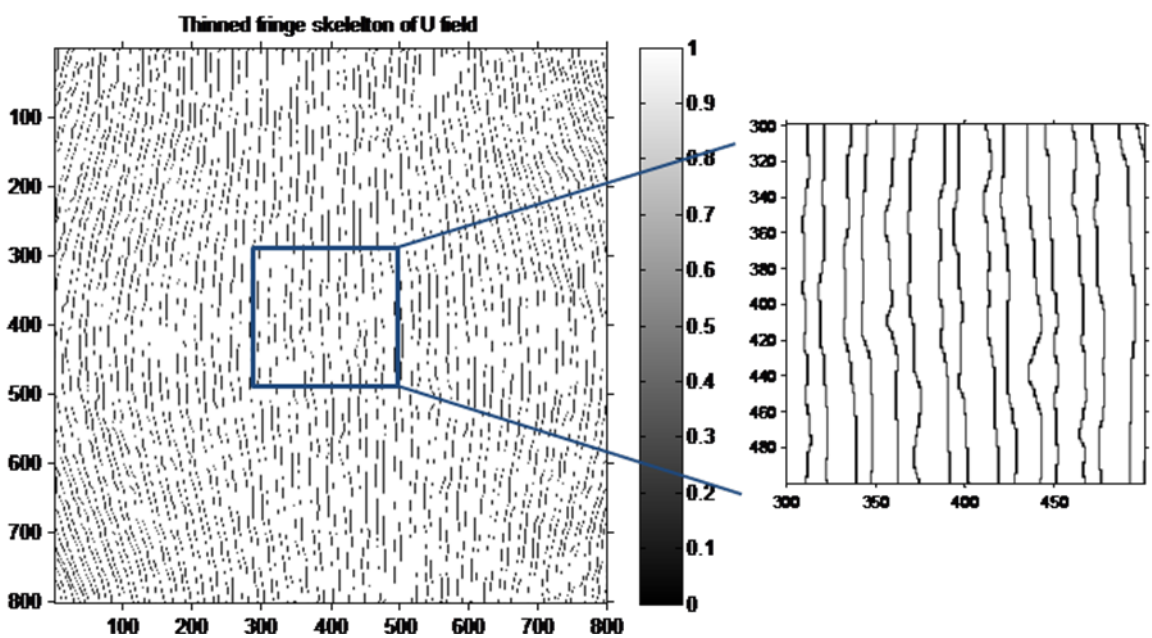

Figure 2-32. Fringe skeleton after fringe thinning for $\left(\left|I_0 - I_2\right|\right)$

Fringe Order Assignment

Fringe skeletons represent the contours of equal displacements and they don't contain any information of fringe orders. Therefore, fringe order assignment is needed for the whole-field fractional fringe order calculation.

Semi automatic fringe order assignment algorithms were developed by some researchers [10-11]. These methods require the user to inform the program the tilting direction of the fringe skeleton interactively. Extra effort is needed to determine the tilting direction beside the phase shifting experiment.

A new method to assign the fringe orders is developed here. It uses the unwrapped phase obtained from phase shifting. Since the unwrapped phase map contains the full-field information, it also contains the contours of equal displacement.

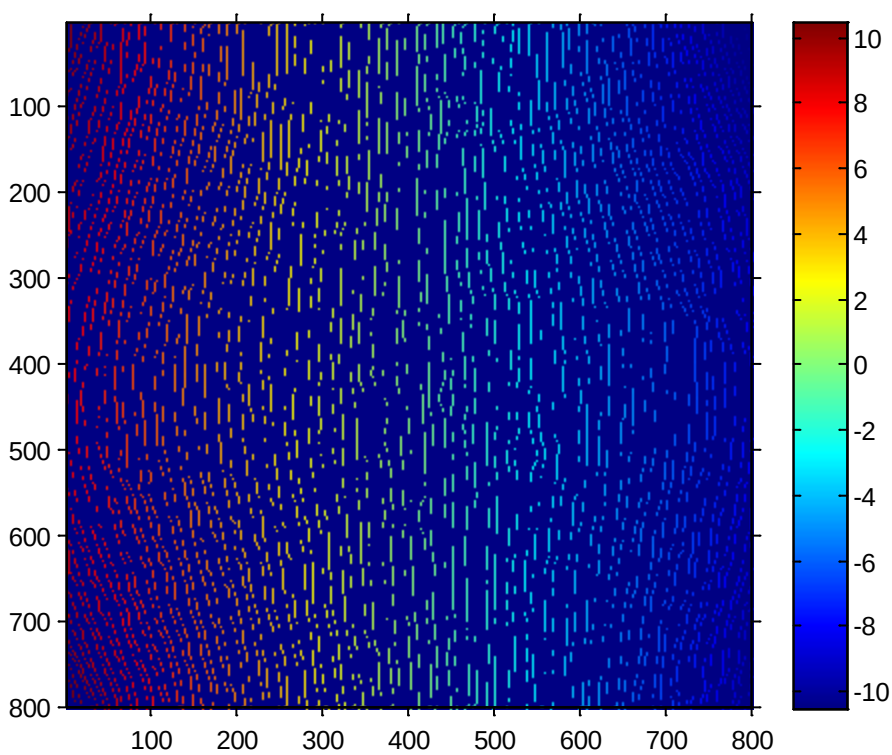

Figure 2-33. Fringe order assignment

Fringe Order Interpolation

Fringe order assignment procedure can only determine the fringe order of the skeletons. To obtain the full-field fractional fringe orders, appropriate fringe order interpolation is needed.

A 1-D interpolation algorithm using cubic spline has been applied to fringe order interpolations [8, 11]. It can result in continuous 1st and 2nd derivative of the fringe order. However, it's not sufficient to describe the 2-D fringe patterns. The main disadvantage of 1-D interpolation is that interpolations along x-direction and y-direction do not yield the exactly same results. So a 2-D fringe order interpolation is necessary.

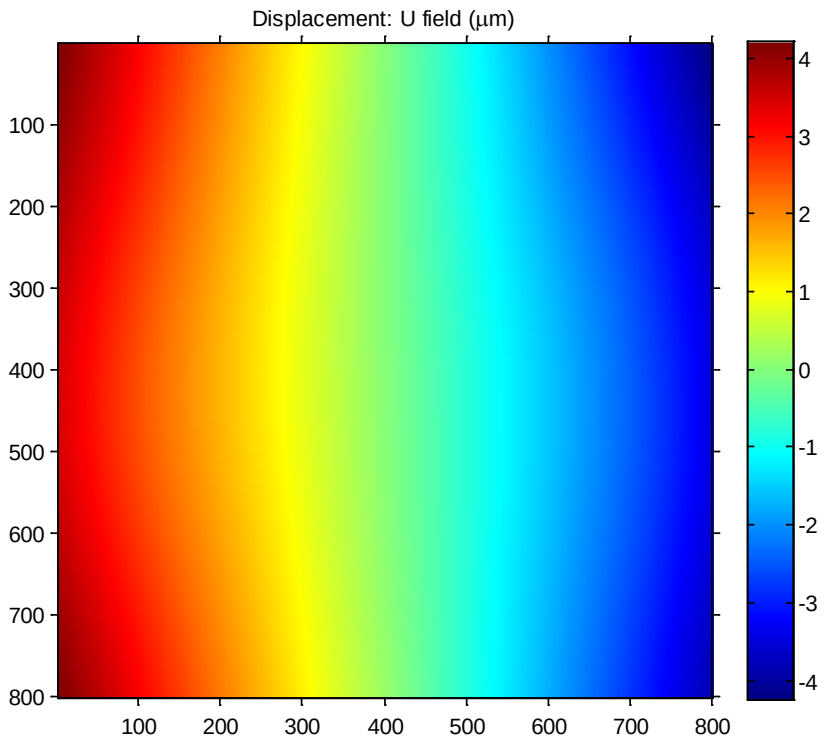

Figure 2-34. Fringe order interpolation

The idea of global or local surface fit from strain calculation of phase shifting is reused here. The surface fit interpolation can obtain the full-field information, and provide an effective way to calculate the gradient (strain) of the fringe order.

Strain Calculation

Based on the fringe interpolation above using surface fit method, the strain (gradient) can be easily obtained as shown in Figure 2-35B.

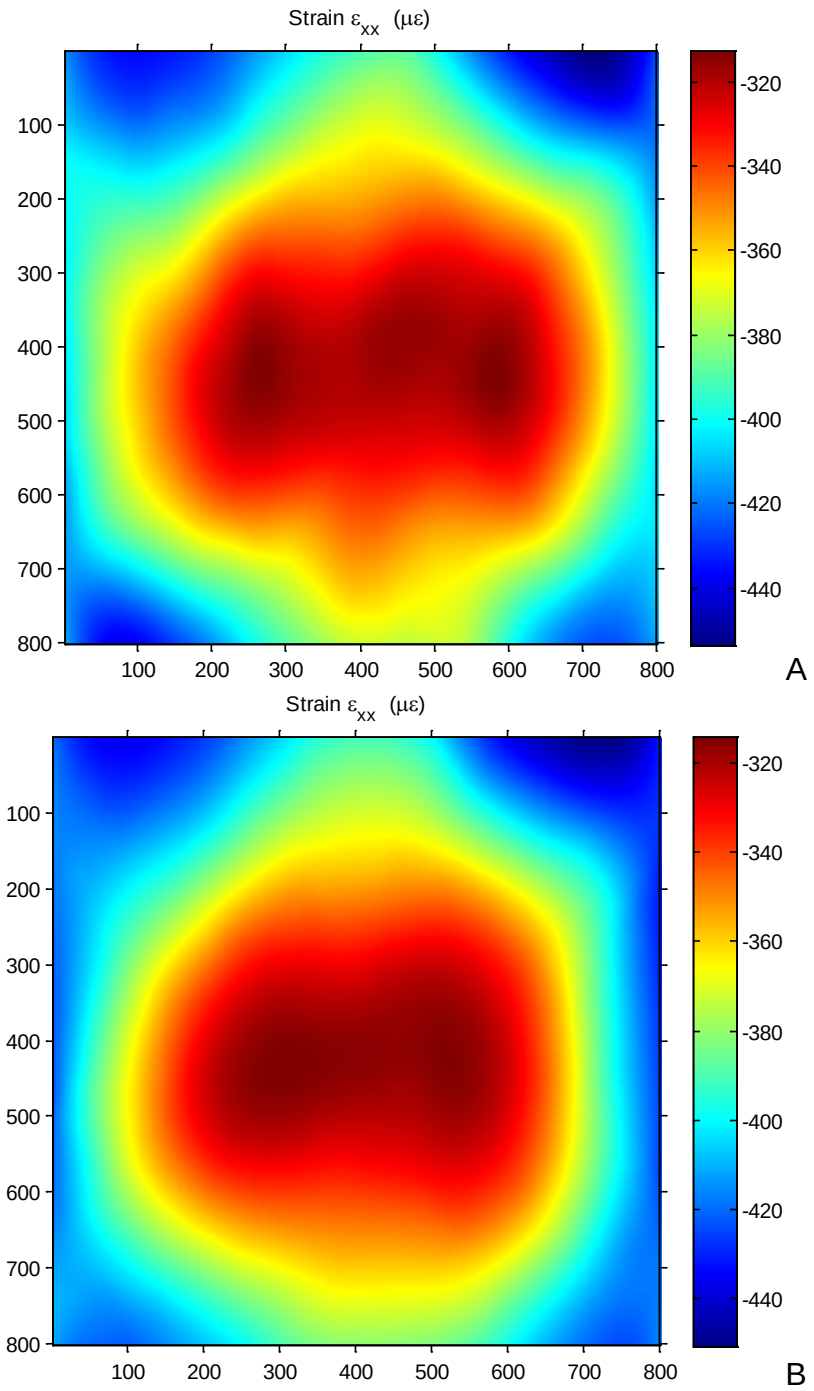

Figure 2-35. Strain calculated. A) By phase shifting. B) By O/DFM

The strain map is smoother than that obtained by phase shifting as shown in Figure 2-35A. This is because most data points in O/DFM method are from the interpolation. Fewer seed points can be used to construct global surface fit.

Summary

The theory of O/DFM to obtain high density fringe skeleton is reviewed. All of the necessary procedures associated with this technique are developed. It requires even number of fringe patterns with phase shifted. Since it uses fringe order interpolation to calculate displacement and strain, the effect of noise can attenuate. However, to determine the fringe order accurately and automatically, it requires the unwrapped phase map obtained from phase shifting method. This way the O/DFM method is a hybrid method combining the techniques of phase extraction and intensity based methods. And since most global surface interpolation is used to obtain the fringe order for most of the data points, smoother displacement and strain field can be obtained.

Summary

This chapter investigated the existing fringe analysis techniques and improved or developed new techniques to analyze the fringe patterns automatically. The following subjects are coved in this chapter,

- Pre-processing of fringe pattern
- Phase shifting
- Displacement and strain calculation
- O/DFM

Pre-processing of fringe pattern involves spatial or frequency filters applied on fringe patterns to remove various noise. Phase shifting is a one phase extraction

method to analyze fringe pattern automatically. It requires at least 3 consecutive fringe patterns with phase shifted. A stage was designed to apply phase ramp to the fringe patterns. A phase unwrapping algorithm based on quality map was adopted and improved to calculate the unwrapped phase map. Inconsistent areas in the unwrapped phase map were detected and repaired. Global surface fit and local surface fit based on thin-plate theory and polynomials separately were developed to calculate displacement and strain maps with higher accuracy instead of the qualitative analysis provided by most of the existing systems. O/DFM method is a hybrid method suitable to analyze fringe patterns with low density of fringes. By combining with the unwrapped phase result from phase shifting, O/DFM can also analyze fringe pattern automatically.

CHAPTER 3
AUTOMATED STRAIN ANALYSIS SYSTEM

Platform

The automated strain analysis system is developed as a form of software. The software is developed using MATLAB R2009a. It is based on Windows Graphic User Interface (GUI) which is menu-driven and mouse-driven, and can be executed on Microsoft Windows NT/2K/XP/Win 7 operating systems.

Functions of the System

The software system includes all the algorithms discussed in previous chapters and other additional image processing functions. The main functions of the software are listed in Table 3-1,

Table 3-1. List of functions in the software

Category	Features
File	U field (N)
	V field (N)
	U field (N+1)
	V field (N+1)
	U field (O/DFM)
	V field (O/DFM)
	Close
Image Processing	Noise Smooth
	Image Crop
Boundary	No Boundary
	Define Boundary of Circle/Ellipse/Rectangle
	Define Boundary using Line
	Define Boundary using Spline
	Load Boundary
Phase Unwrapping	Quality-Guided PU
	Phase Smoothing
O/DFM	Fringe Skeleton
	Fringe Thinning
	Fringe Order Assignment
	Fringe Order Interpolation
Tool	Data Along A Line
	Phase Repair
	Binary Image Repair
	Complex Boundary

Displacement/Strain	U Displacement
	V Displacement
	Strain xx
	Strain yy
	dU/dy
	dV/dx
	Shear Strain
	R Displacement
	Theta Displacement
	Strain rr
	Strain Theta
	Shear Strain rTheta
Display	Filtered Fringe
	Wrapped Phase
	Unwrapped Phase
	U Displacement
	V Displacement
	Deformation Plot
	Strain xx
	Strain yy
	Shear Strain exy
	R Displacement
	Theta Displacement
	Strain rr
	Strain Theta
	Shear Strain rTheta
Help	About
	Demo video

Demonstration of the System

A demonstration of the system for the analysis of the fringe patterns from a tension test on an open-hole aluminum specimen is shown here. The dimensions of the test specimen and fringe patterns of the V field are shown in Figure 3-1.

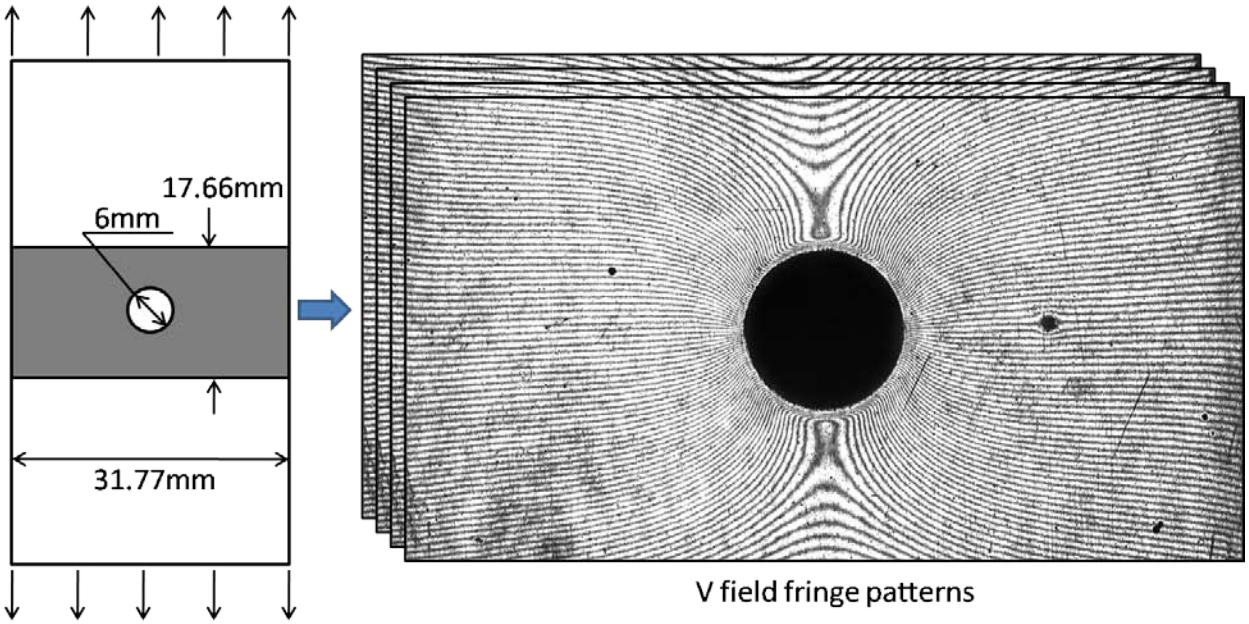

Figure 3-1. Open-hole test specimen and fringe patterns

Figure 3-2~8 show some screen captures of the software.

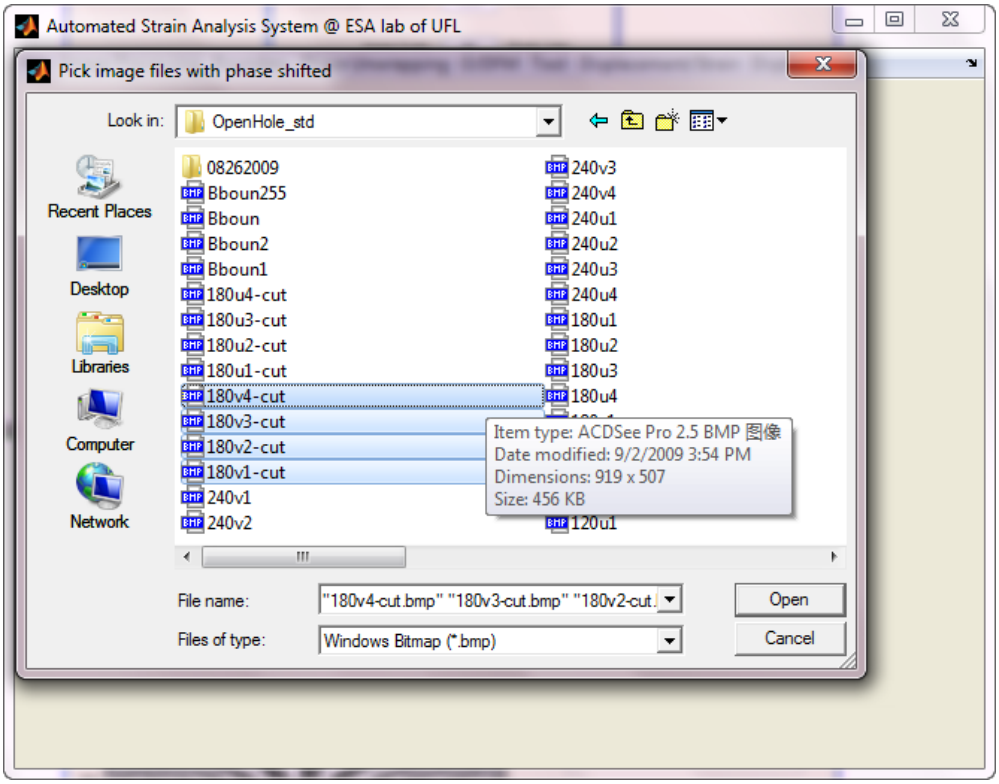

Figure 3-2. Open image files

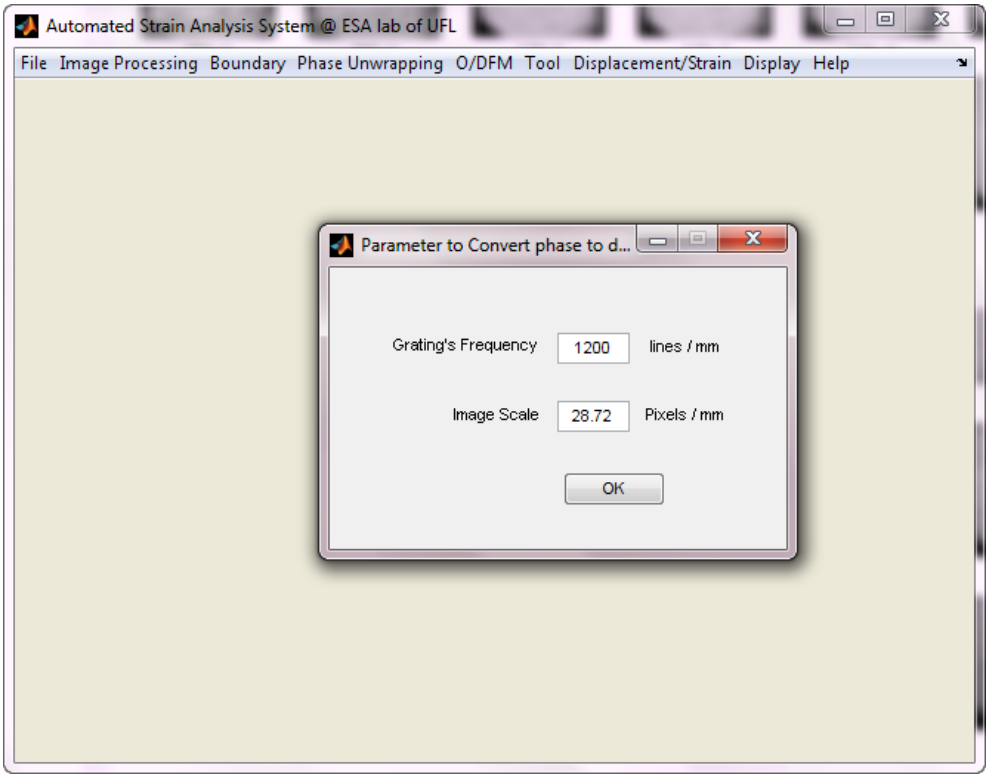

Figure 3-3. Coordinate system translating parameters

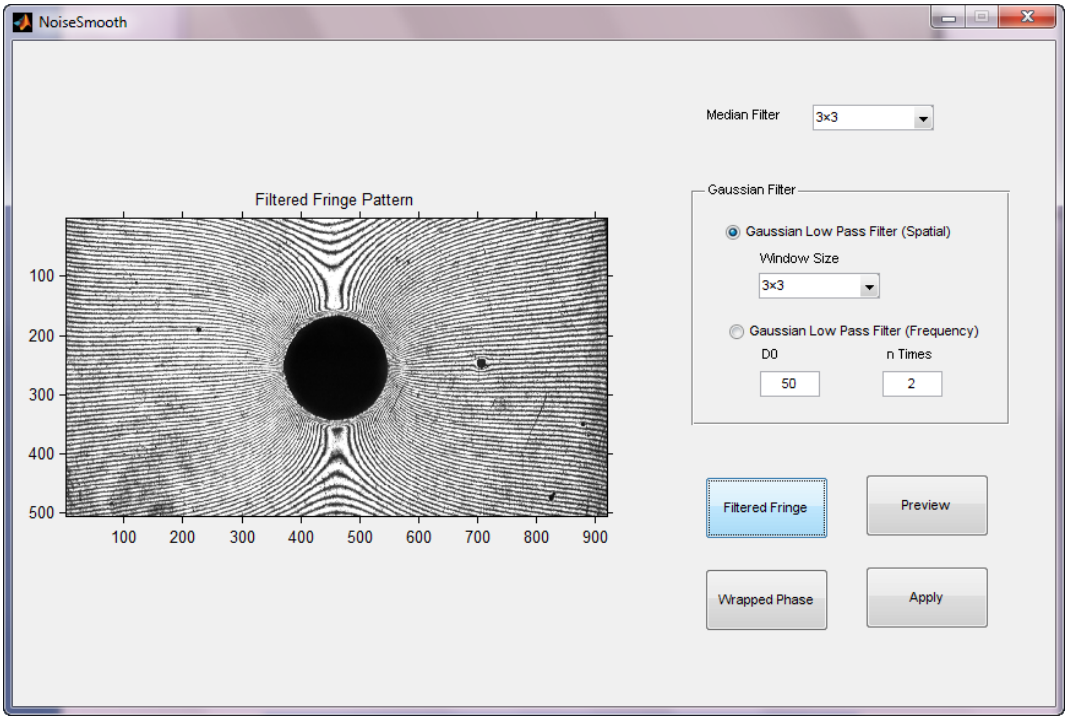

Figure 3-4. Noise removal

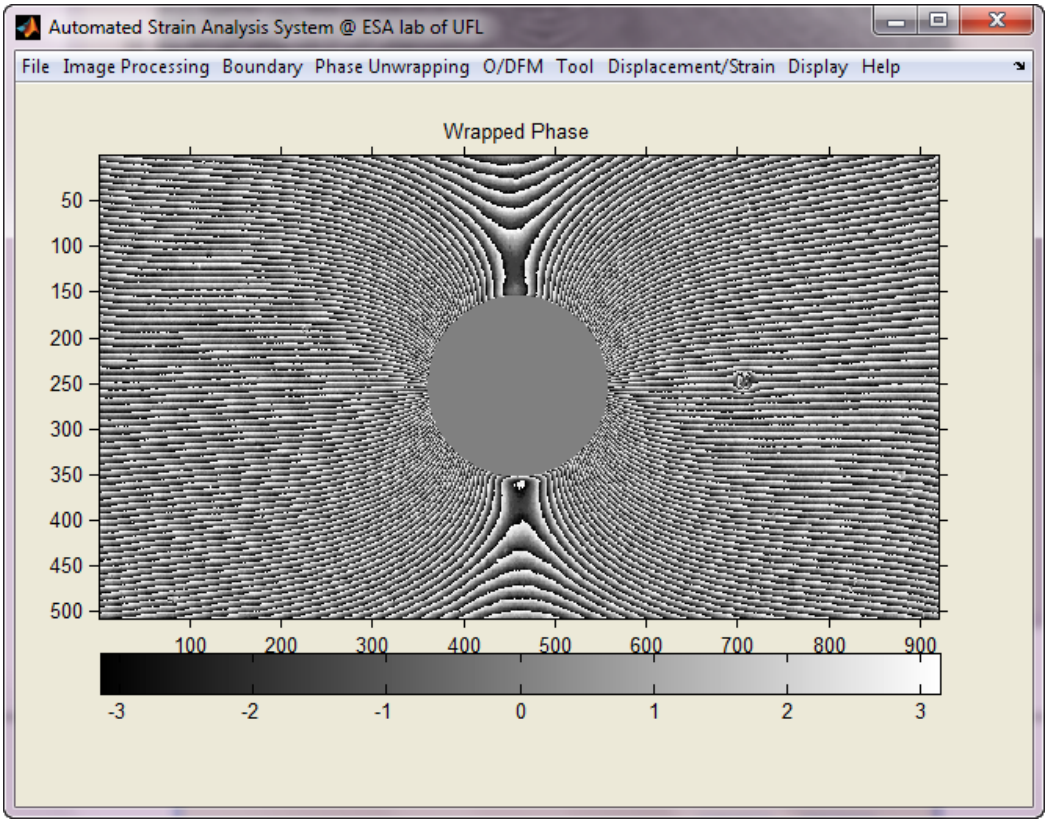

Figure 3-5. Define the boundary

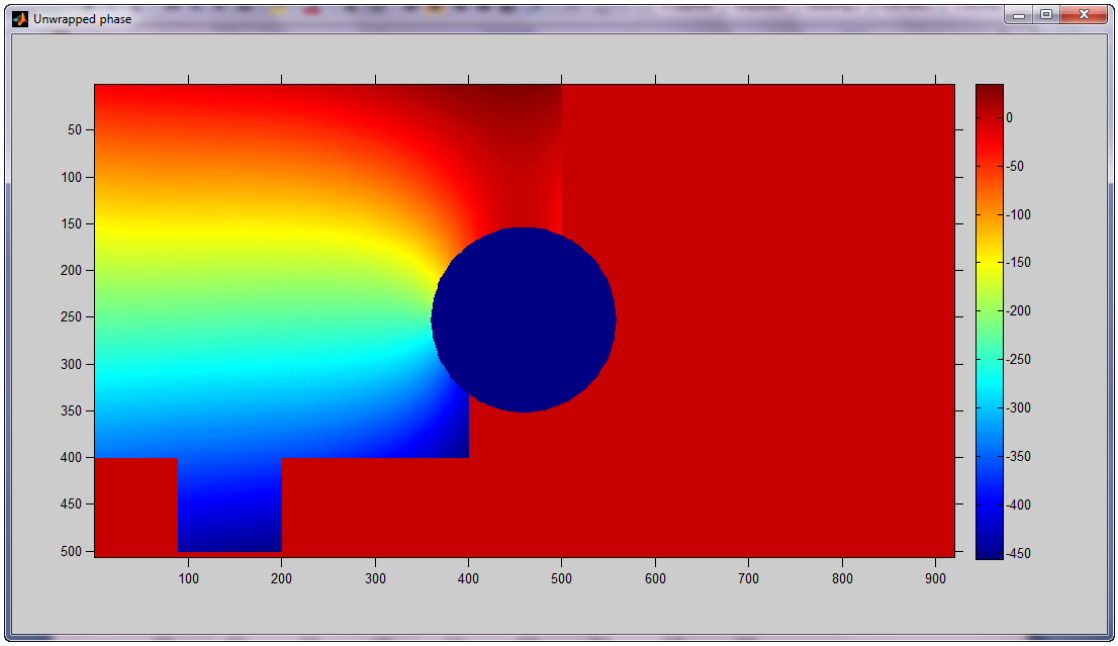

A

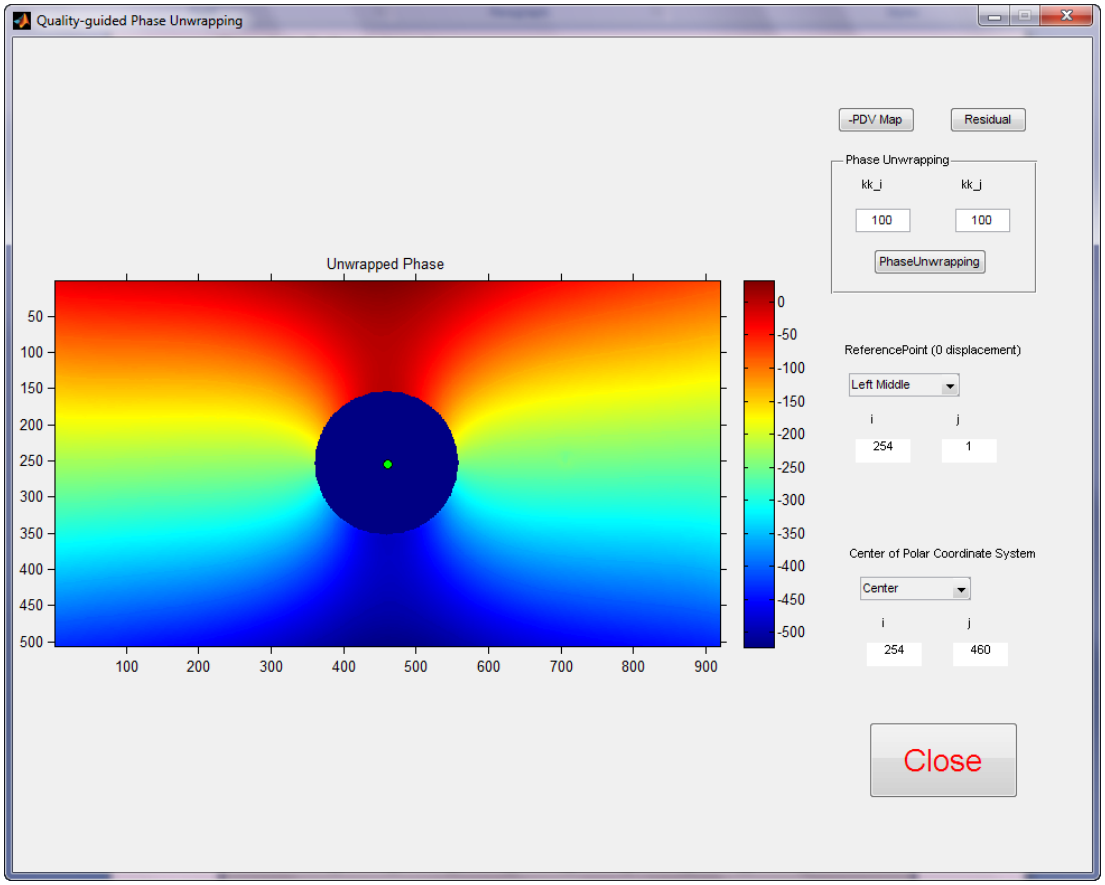

B

Figure 3-6. Quality guided phase unwrapping. A) Unwrapping progress. B) Final unwrapped phase

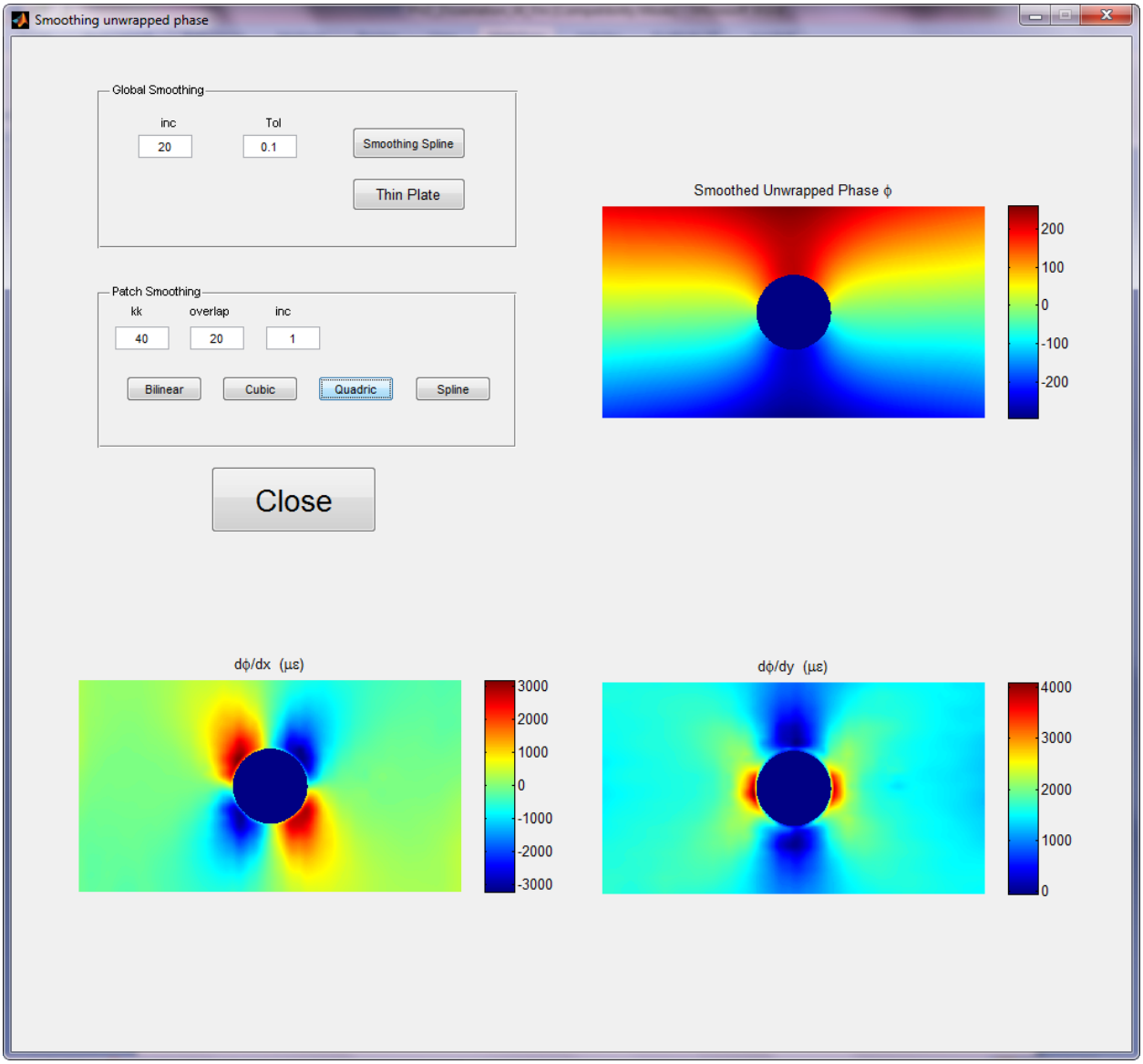

Figure 3-7. Phase smoothing

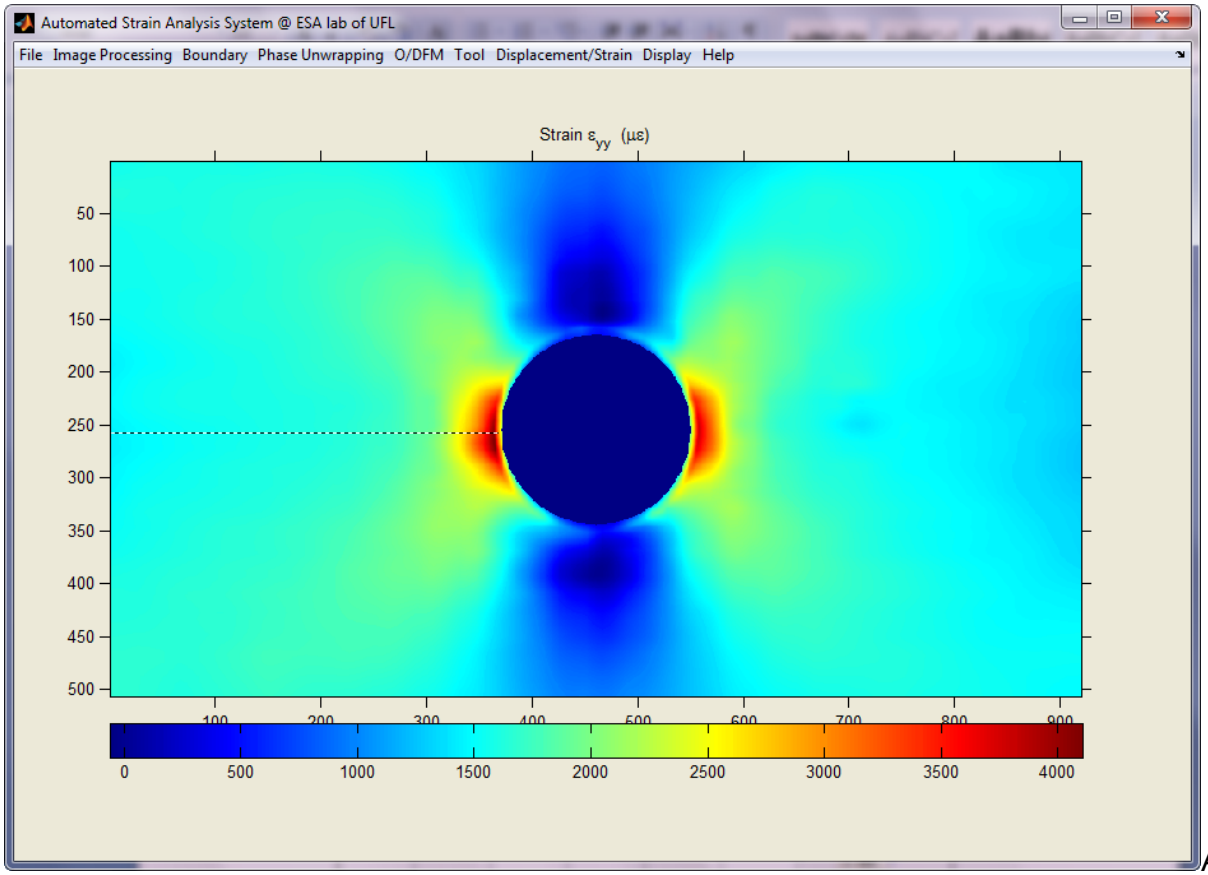

A

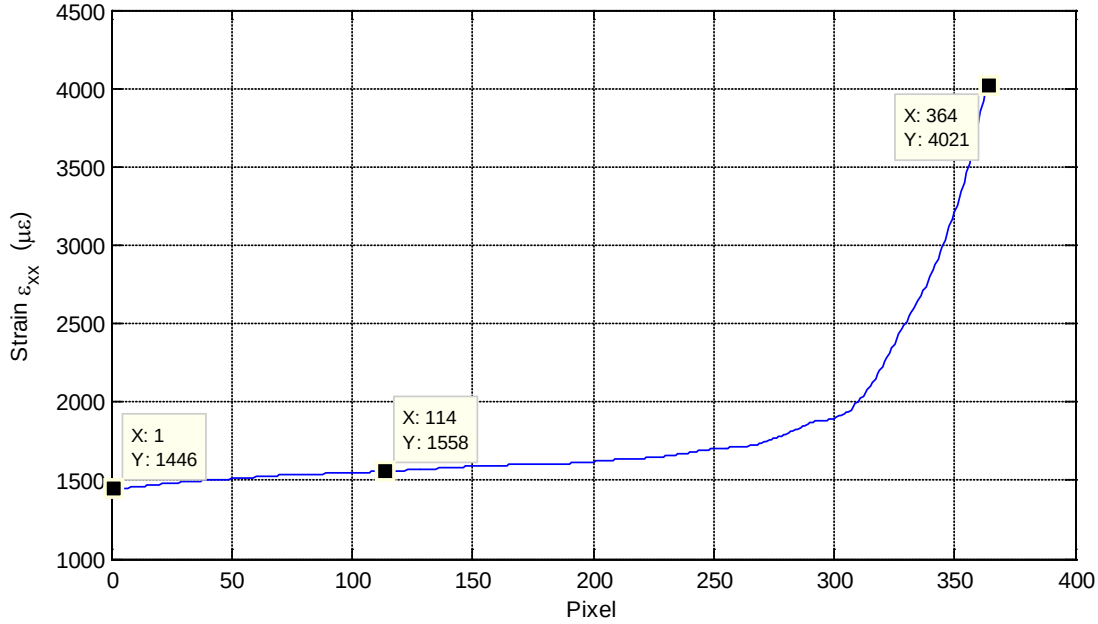

B

Figure 3-8. Data extraction. A) Define the data path. B) Data along the data path

Validation

Two tests, 4-point bending test and open-hole test, were conducted to validate the system. The fringe patterns for the tests were analyzed using the system. The results are compared with those results obtained from manual calculation or finite element (FE) simulation.

4-point Bending Test

The dimension of the 4-point bending test specimen is shown in Figure 2-23. The fringe patterns for the U and V field are shown in Figure 3-9.

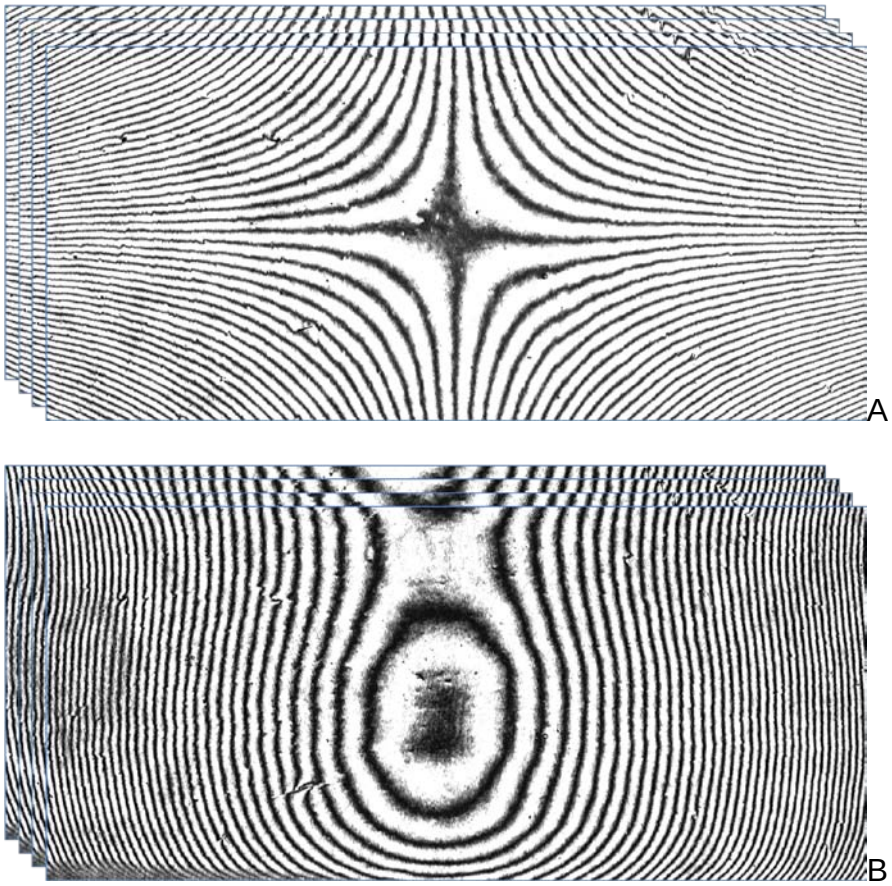

Figure 3-9. Fringe pattern. A) U field. B) V field

These fringe patterns were inputted into the automated strain analysis system and the result strain maps are shown in Figure 3-10.

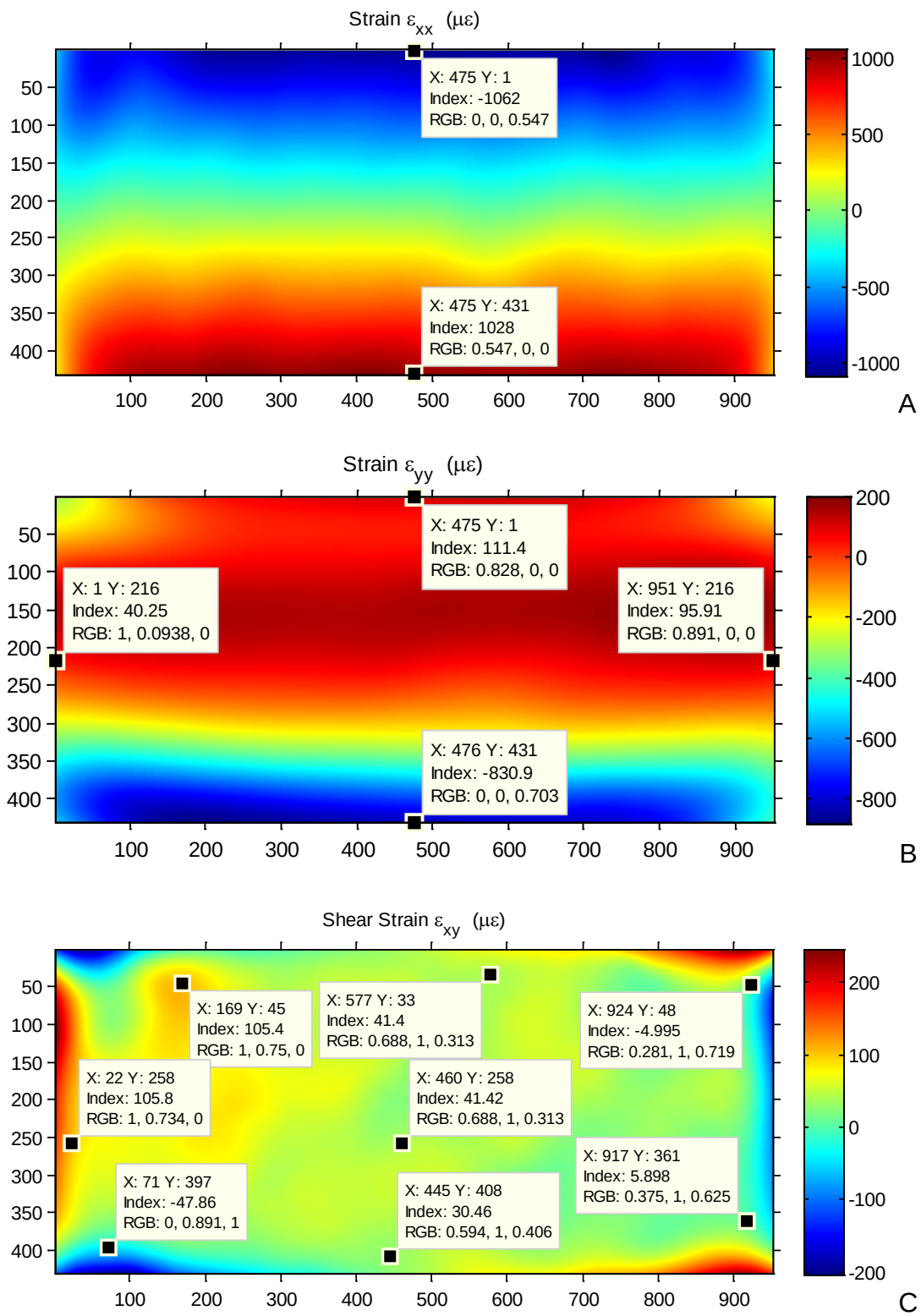

Figure 3-10. Strain maps from automated strain analysis system. A) Strain ε_{xx}. B) Strain ε_{yy}. C) Strain ε_{xy}

A FE model was developed to simulate the 4-point bending test. The strain maps within the same area are shown in Figure 3-11. When compared to the results in Figure 3-10, they agree very well for most areas.

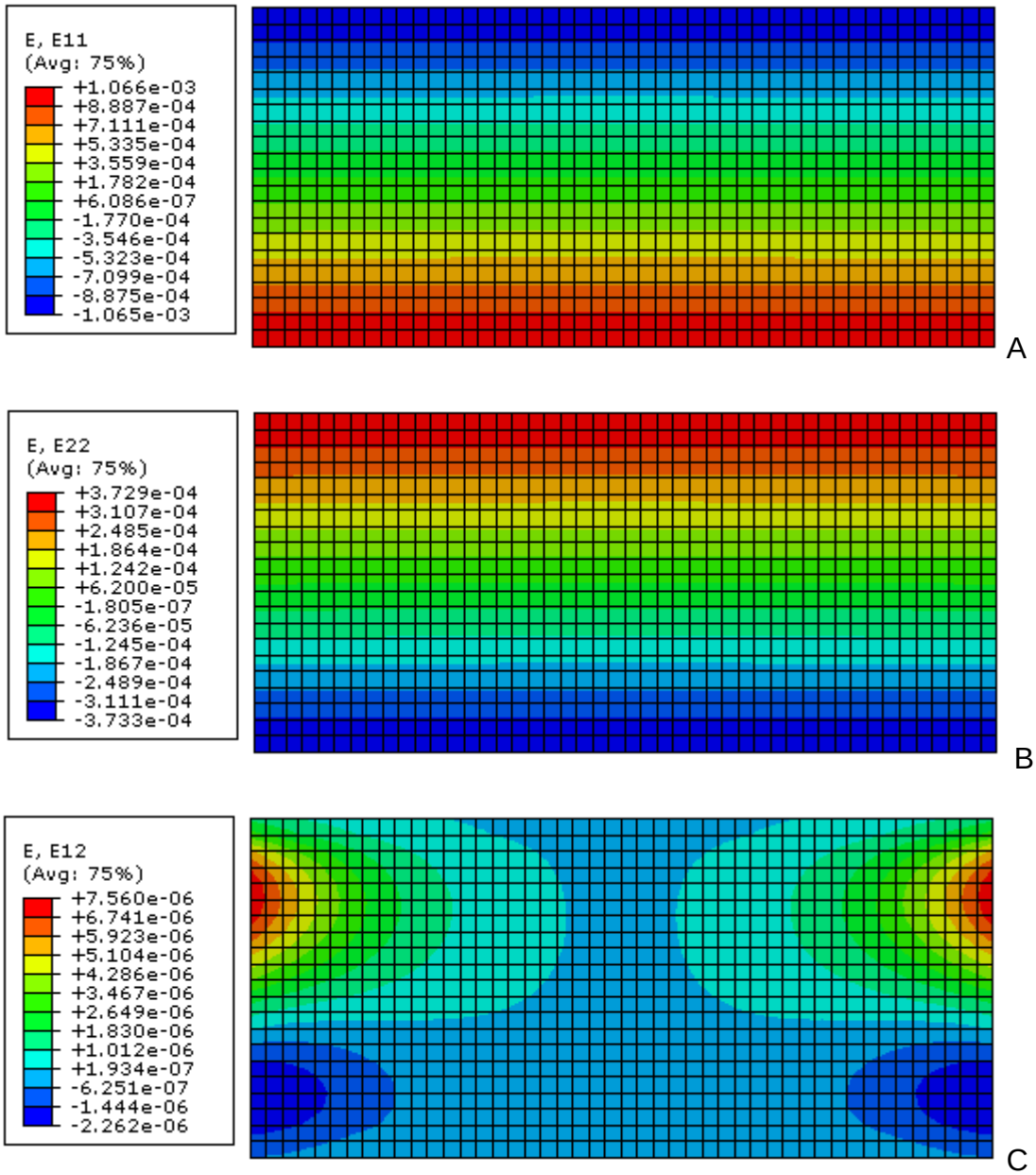

Figure 3-11. Strain maps from FE. A) Strain ε_{xx}. B) Strain ε_{yy}. C) Strain ε_{xy}

Furthermore, the result can be compared to the manual calculation for several discrete points as shown in Figure 3-12.

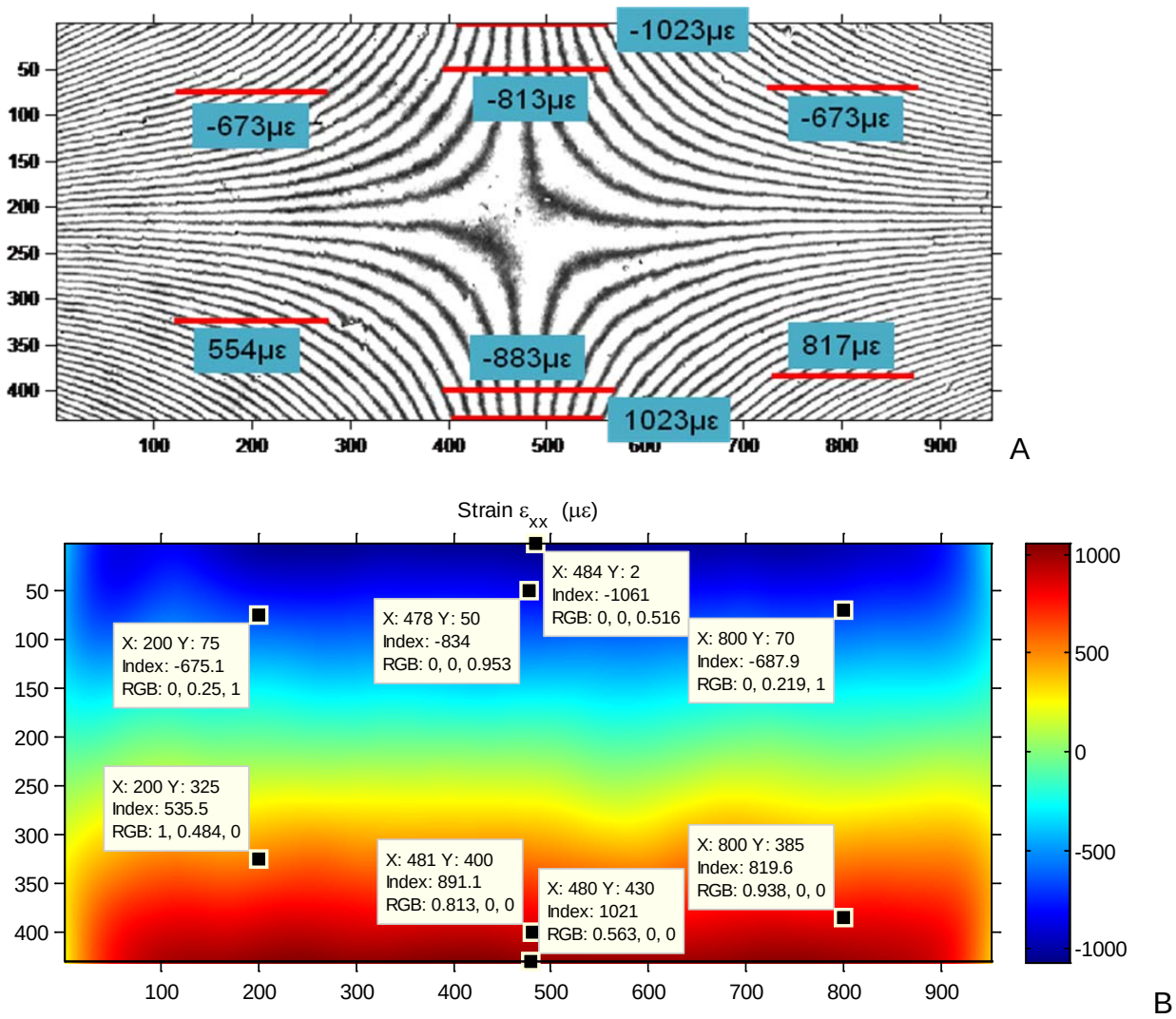

Figure 3-12. Strain result from manual calculation and analysis system. A) Strain ε_{xx} from manual calculation. B) Strain ε_{xx} from the analysis system

The strain results from manual calculation and the automated strain analysis system match very well for these discrete points.

Open-hole Tension Test

The dimension of the 4-point bending test specimen is shown in Figure 3-1. The fringe pattern for the V field is also shown in Figure 3-1.

These fringe patterns were inputted into the automated strain analysis system and the result strain map (ε_{yy}) are shown in Figure 3-13A. A FE model was developed to

simulate the Open-hole tension test. The strain map (ε_{yy}) within the same area are shown in Figure 3-13B. It matches very well with the result from the analysis system for most areas except the extremely high strains in the small areas close to the edge of the hole due to the low resolution and low quality of fringe patterns within these areas.

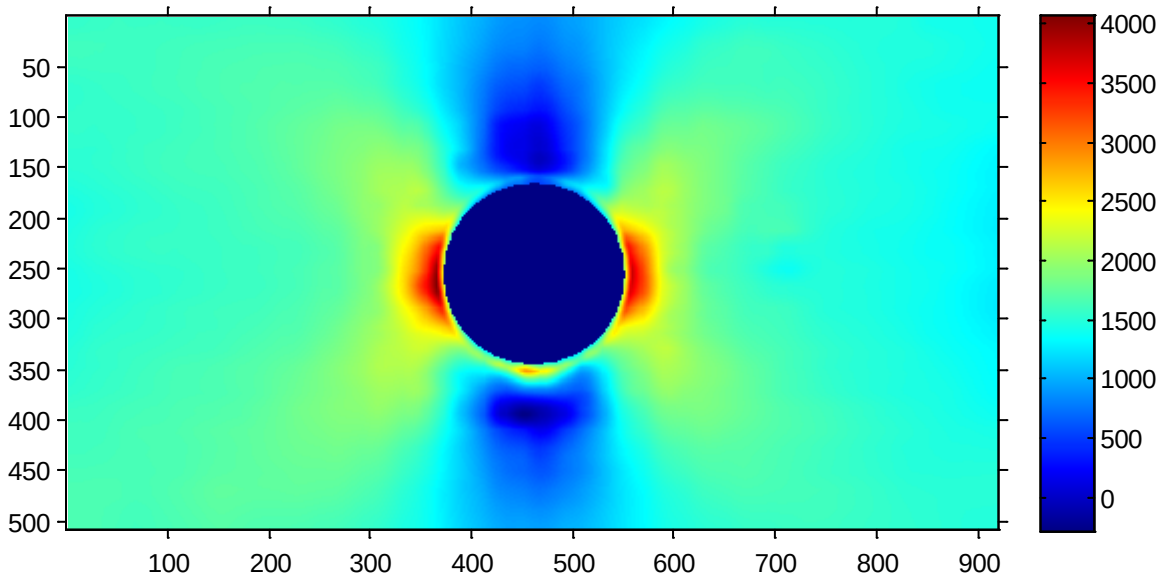

A

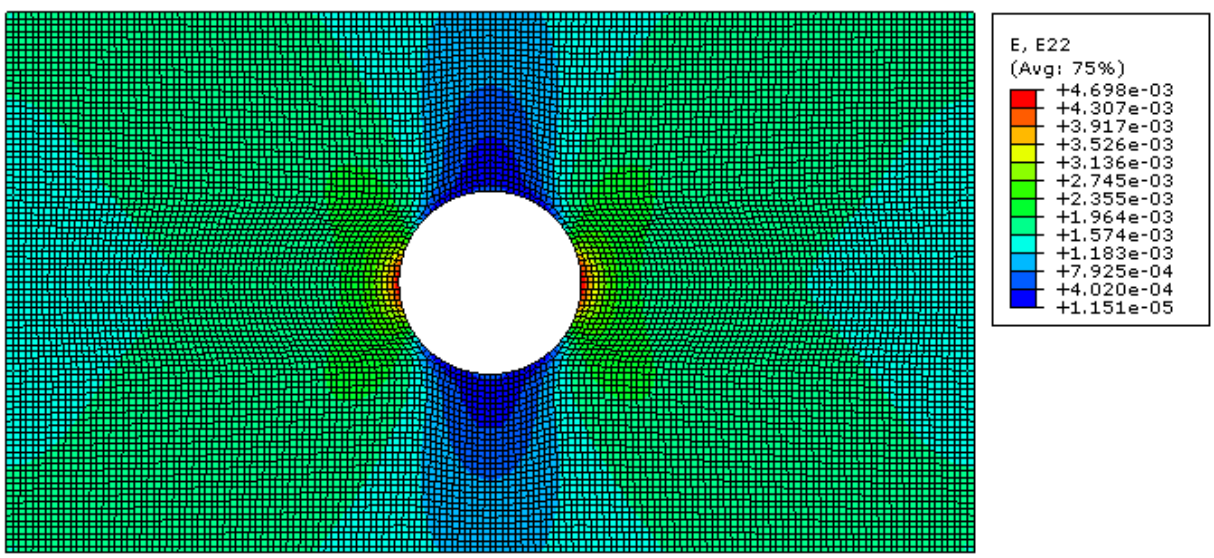

B

Figure 3-13. Strain map (ε_{yy}) from automated strain analysis system and FE simulation. A) From automated strain analysis system. B) From FE simulation

Furthermore, the result can be compared to the manual calculation for several discrete points as shown in Figure 3-14.

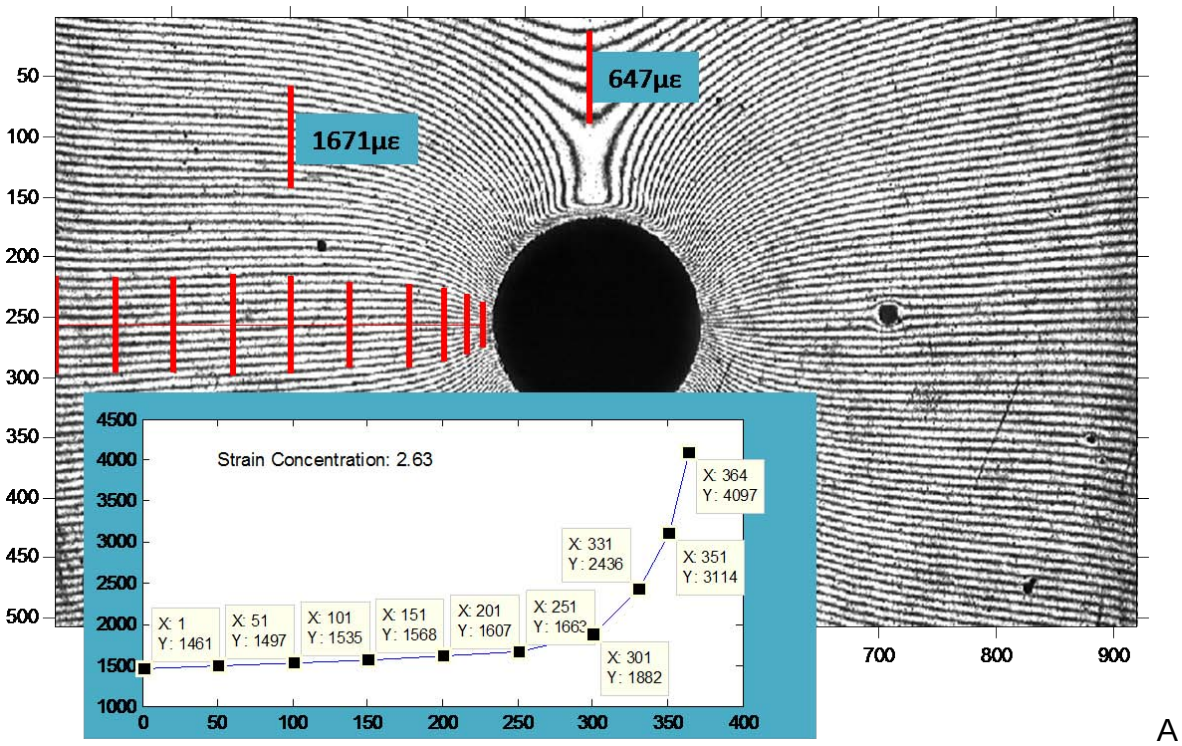

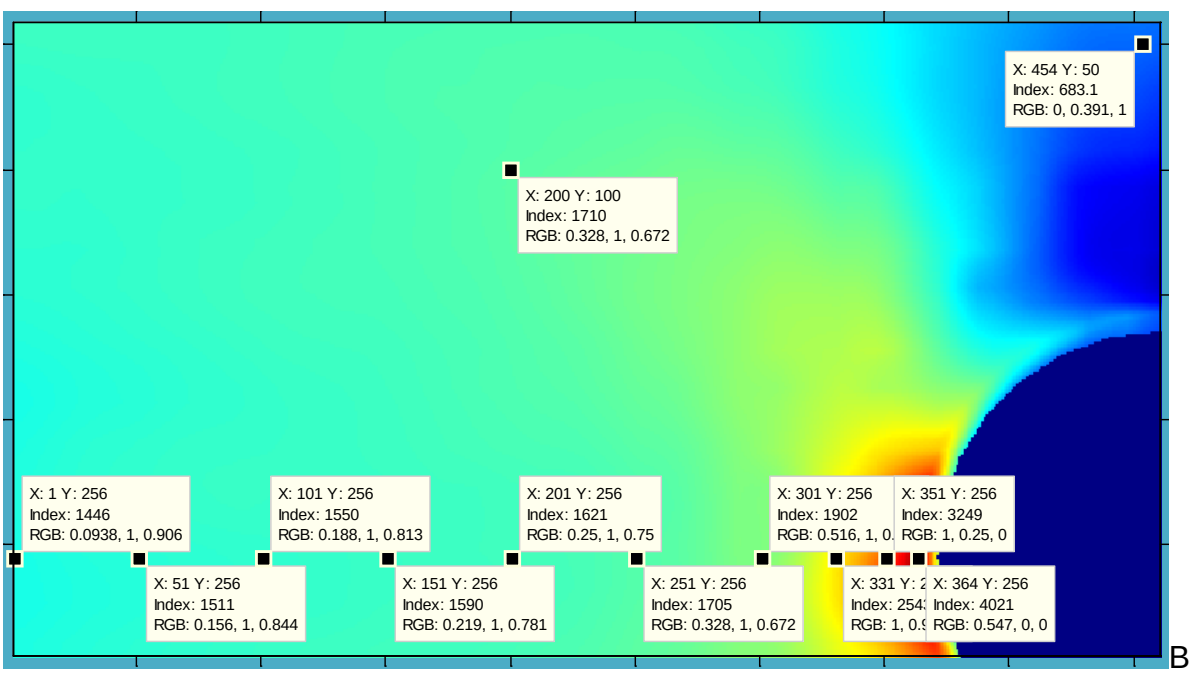

Figure 3-14. Strain result from manual calculation and analysis system. A) Strain ε_{xx} from manual calculation. B) Strain ε_{xx} from the analysis system

The strain results from manual calculation and the automated strain analysis system match very well (≤ 5% variance) for these discrete points. The strains along the narrowest section from the automated strain analysis system, manual calculation and FE simulation are shown in Figure 3-15. Good agreement between them is observed.

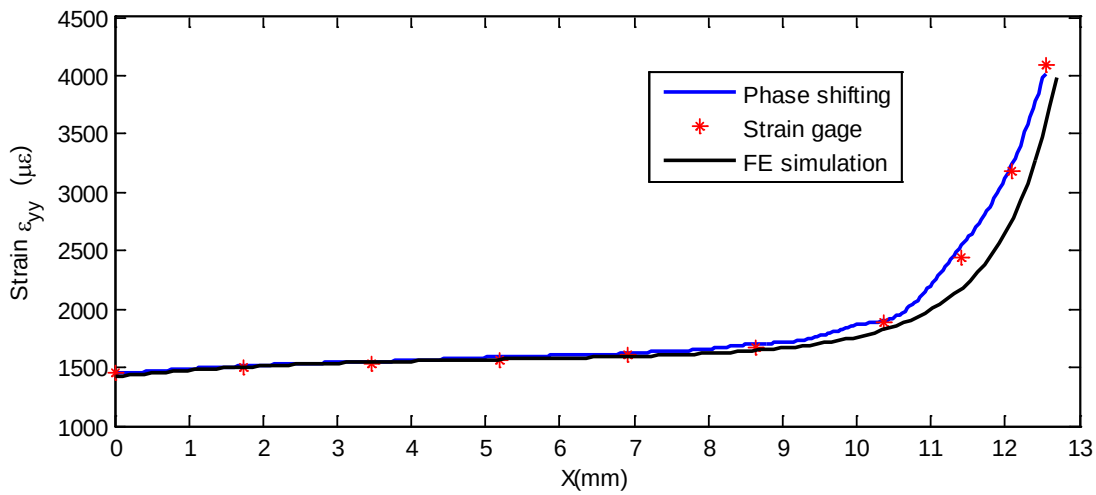

Figure 3-15. Strains along the narrowest section

The stress or strain concentration factors from the FE simulation, manual calculation and the analysis system are calculated and shown in Table 3-2. They agree well with each other.

Table 3-2. Concentration for the open-hole aluminum test

	Theoretical (Mechanics of Materials)	FE	Manual	System
Stress Concentration	2.65	2.54		
Strain Concentration		2.64	2.62	2.59

Summary

The automated strain analysis system is developed as a Windows GUI-based software to analyze fringe patterns automatically. It includes all the algorithms

presented in the previous chapters. With the use of this expert system, full-field displacement and strain information can be effectively and accurately extracted from the phase shifted fringe patterns. And the system can be updated step by step with the development or improvement of new algorithms in the future.

Two tests were conducted to validate the system. The fringe patterns were analyzed via the system and manual calculation. FE models were conducted for both tests. The results obtained from the system, manual calculation and FE simulation are compared and they show great agreement with each other.

CHAPTER 4
APPLICATIONS OF AUTOATED STRAIN ANALYSIS SYSTEM

Residual Stress Characterization of Plain Woven Composites

Introduction

Composite materials are widely used by various industries. There are two categories of composites, plies composed of unidirectional or randomly scattered chopped fibers (laminates), and fiber bundles woven into a regular pattern (textiles). As the desire increases for advanced material properties that composites provide, more research needs to be performed so that they can be fully characterized and understood. The residual stresses resulting from the manufacturing process of composite gain a lot of attention because they will reduce the life time of the composite structures and neglecting them will overestimate the performance prediction. Much research has been devoted to determining the residual strains that develop after the cure of laminated composites. However, with the growing popularity of woven composites, attention in research must be shifted. In order to fully understand how the woven structure will behave after cure, the residual strains associated with the curing process must be measured. By understanding the residual stresses that develop, one can better assess the structural life remaining in the specimen in question.

Residual stresses within composites come from the requirement of high temperature heating cycle during the manufacturing process. Those high temperatures are required so that the resin can fully heat and complete its polymerization process as well as wet the fibers and finally cure into a hard structure. This necessary process introduces a significant amount of residual stresses into the composite specimen after the heating cycle completes and the specimen cools down to room temperature. The

residual stresses in composites arise from both chemical and thermal shrinkage [114]. The chemical shrinkage is due to polymerization of the resin in which the two monomers in the epoxy come together to form the final compound. The majority of the chemical shrinkage occurs during the initial heating period of the curing cycle and therefore does not contribute to the overall residual stresses. This is because stresses cannot exist before the composite fully cures and the resin transforms to the solid state. However, there is some additional chemical shrinkage that does contribute to the final residual stress levels in the specimen that occurs after the solidification of the resin. On the ply level, a significant amount of the residual stresses develop because of the mismatch that naturally exists between the coefficients of thermal expansion (CTE) of the two materials. The resin typically has a much higher CTE value than the fiber; therefore a large amount of thermally induced shrinkage would develop in the matrix. However, the higher stiffness fibers restrict the contraction of the matrix. That restriction is what introduces the residual stresses into the composite.

Unlike the uniform strain distribution of laminates, significant strain variation within the representative volume element (RVE) of textile composites, as shown in Figure 4-1, is proven under a tension loading test [1, 105]. And the residual strain distribution should have the same difference between laminate and woven textile. Since the strain variation exists in woven textiles, an experimental technique with full-field measurement capability is desired.

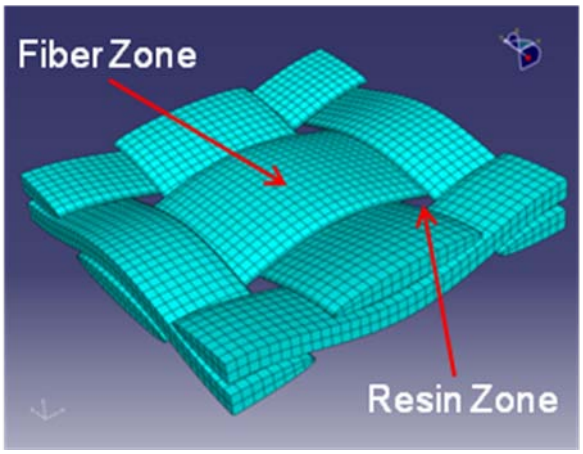

Figure 4-1. Representative volume element of the plain woven textile

Many methods exist to determine the residual stresses of composite materials. They can be divided into destructive methods and non-destructive methods. Destructive methods include hole-drilling [115-116] and first ply failure test [117-118]. Non-destructive methods include X-Ray diffraction [119], imbedding sensors [120], neutral diffraction method. The destructive methods will destroy the specimen and can only do the measurement of several points. X-Ray diffraction will introduce foreign materials to the specimen. The result from imbedding sensors is localized and the expense of neutron diffraction method is extremely high. In order to measure the residual strain for woven textiles, a non-destructive method with full-field measurement capability is desired. Cure reference method (CRM) is such a method.

Classical laminate theory (CLT) is suitable to calculate the residual stresses of traditional laminate composites once the material properties and strain data are known [103, 121]. However, it cannot be applied to woven composite because the complexity of woven geometry no longer allows these straightforward calculations. To predict the residual stresses associated with the residual strains of woven composite, Finite

Element (FE) modeling is the preferred analysis method [122-123]. And FE model can compare the residual strains obtained experimentally by simulating the curing cycle.

Cure Reference Method

CRM was originally developed by Ifju, et al. at the University of Florida as a non-destructive technique to measure full-field residual strains of composite materials as the composite cools via moiré interferometry [124]. By using CRM, the residual strains could be measured for the woven composite geometry on a full-field scale, and for the RVE. Because of the regular repeating pattern exhibited by woven composites, it has been shown that a distinct regular fringe pattern should develop that would aid in the strain characterization [125]. Additionally, the use of CRM does not reinforce the specimen and avoids destruction of the specimen. The focus of this work is on plain woven composites. The prepreg is CYCOM 97714A made by CYTEC company.

To use moiré interferometry in CRM, the autoclave tool shown in Figure 4-2 was used firstly to tune the interferometer to obtain null field fringe pattern. Then it was removed and the specimen was placed in the same position. By this way, the absolute residual strain in room temperature referred to the cure temperature can be measured.

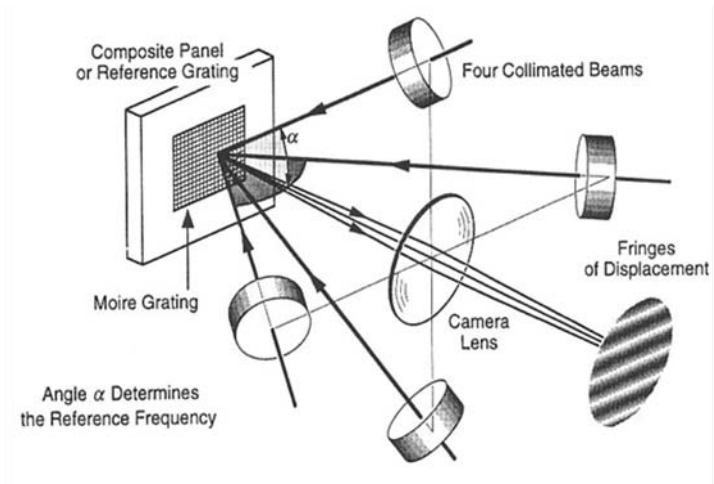

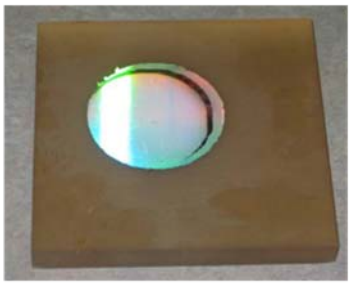

Figure 4-2. Cure reference method

The displacement field is obtained via CRM which requires a moiré interferometry diffraction grating be attached to the composite during cure. A diffraction grating was transferred from the autoclave tool to the prepreg at the cure temperature while the specimen was at a free stress state. When the specimen cools to room temperature, the grating records the complete strain development.

Ifju et al. [124] described a procedure of creating an autoclave tool for the CRM. Each grating made by the process required approximately 78 hours, including the cure times, aluminization steps and dwelling times. Significant work was done by Strickland [126] to reduce the production time to approximately 45 hours. This reduction allowed quicker production and enhanced the grating quality with fewer processes and fewer opportunities for errors as shown in Figure 4-3. The technique yielded mixed results in terms of grating quality.

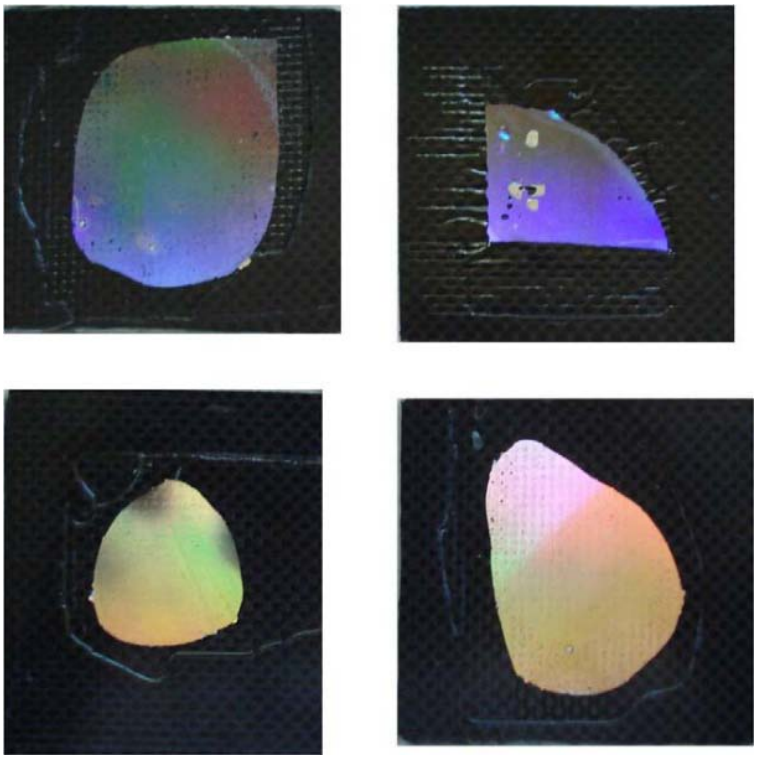

Figure 4-3. 4 CRM gratings

Result of Residual Strains from Experiment

One of the specimens in Figure 4-3 was placed in front of the moire interferometer and fringe patterns are recorded by the CCD camera and shown in Fig. 4-4.

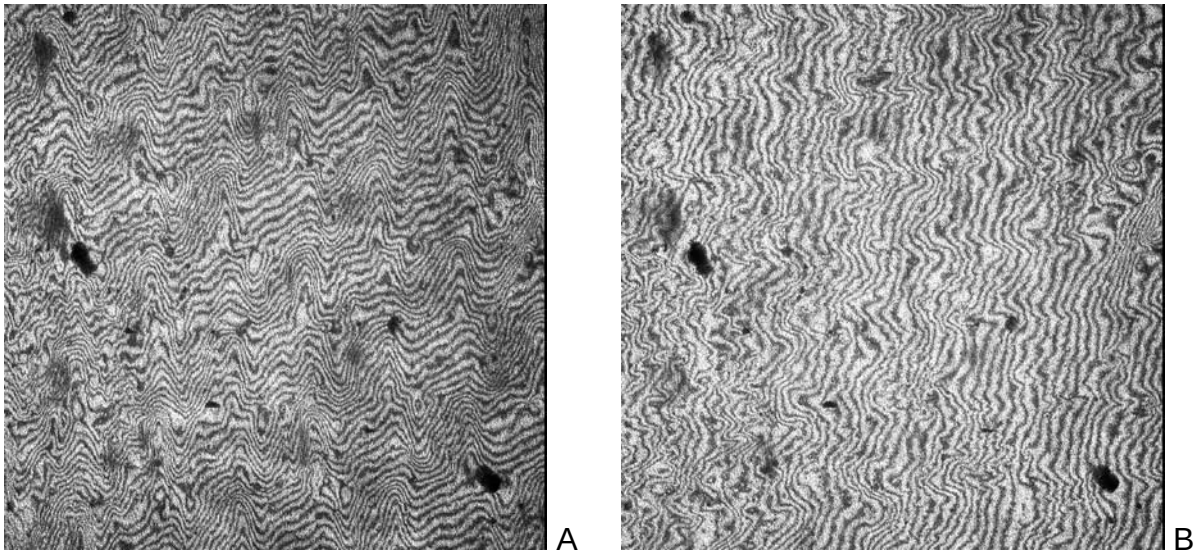

Figure 4-4. Fringe patterns. A) U field B) V field

The automated strain analysis system was used to obtain the displacement and strain maps. Figure 4-5 shows the displacement distribution for the U and V field.

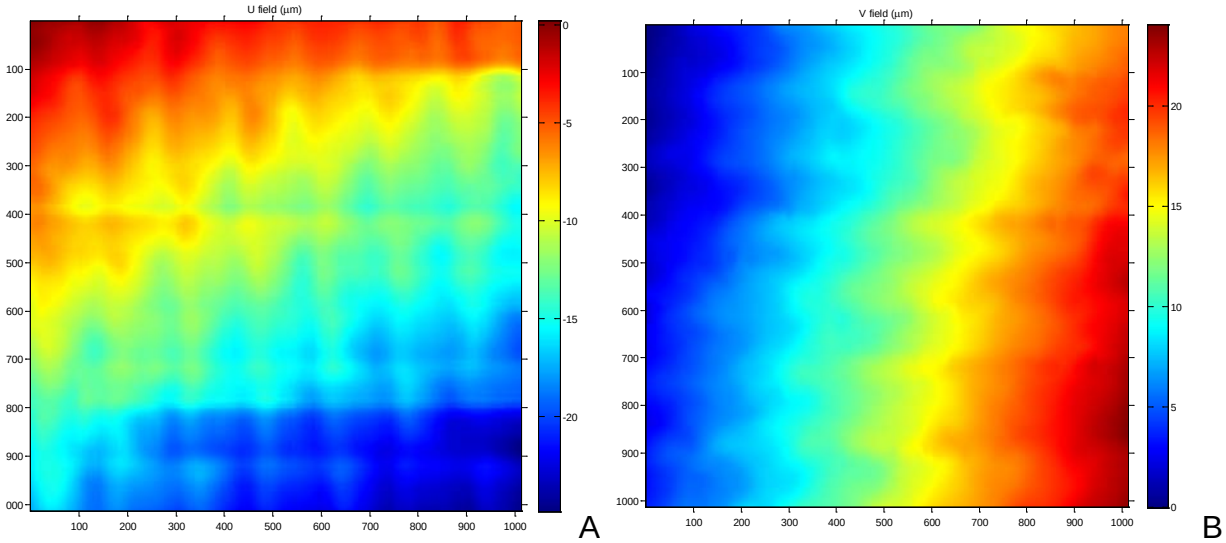

Figure 4-5. Displacement field. A) U field B) V field

Based on the displacement field, the strain field can be obtained as shown in Figure 4-6. It's seen that the maximum repeating tensile strains developed were approximately 500 $\mu\varepsilon$ and the maximum repeating compressive strains were approximately -1400 $\mu\varepsilon$ in both the U and V fields. The strain map that developed can be explained by relating the trends to the geometry of the woven textile. There are two main regions within the RVE, the resin and the fiber regions. The resin zone expands the entire length of the RVE between fiber bundles. However, along that length, the resin depth from the surface changes as it crosses over transverse bundles. The fiber regions have much lower surface resin content levels since they are much closer to the surface.

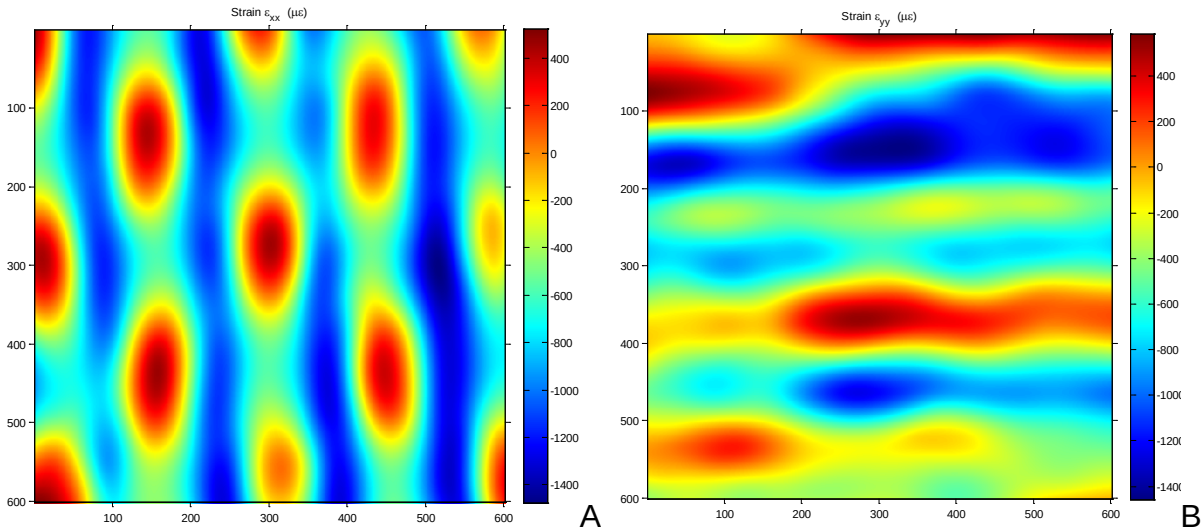

Figure 4-6. Strain map. A) Strain ε_{xx} B) Strain ε_{yy}

The regions of tensile strains occurred along the top of the fiber bundles in the fiber regions in both fields of view, whereas the compressive strains were developing throughout the resin zones. The CTE value for the resin is significantly larger than that of the fiber, so as the composite cools to room temperature, a considerable amount of

residual strains develop within the resin because the fiber bundles restrict free contraction in those areas. The tensile regions that developed along the fiber bundles were a direct result from the compressive resin regions. To maintain static equilibrium, the thin resin zones that cover the fibers must undergo tension to accommodate for the large compressive areas. At the same time, it can also be noted that the strain patterns and values are similar for the U and V fields. That was expected to occur because of the symmetry of the woven geometry.

The strain within one RVE can be extracted via averaging the four RVEs in Figure 4-6 and they are shown in Figure 4-7. Furthermore, the average strain of the RVE can be obtained as -596 $\mu\varepsilon$ for U field and -450 $\mu\varepsilon$ for V field.

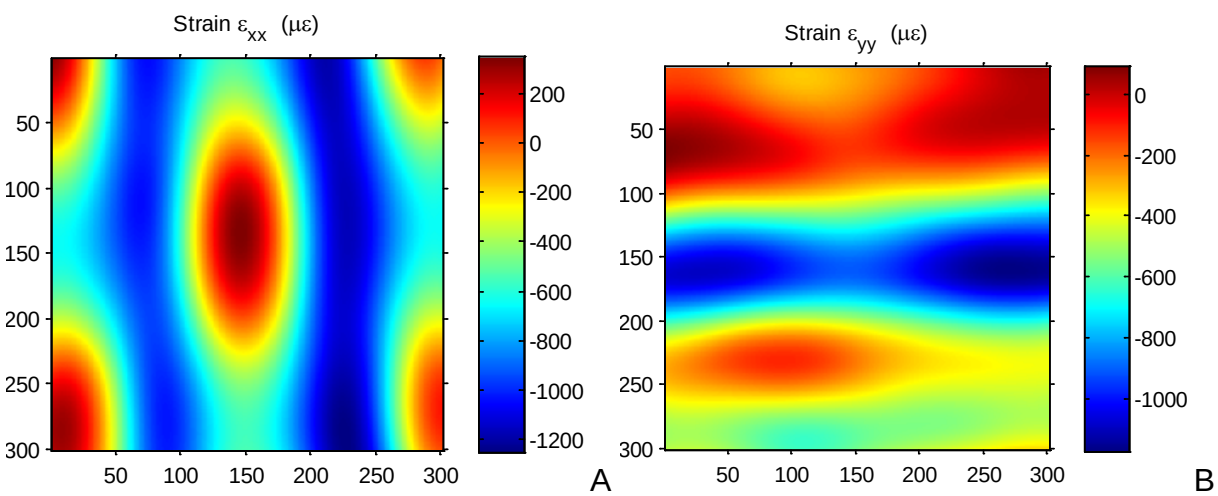

Figure 4-7. Strain map within one RVE. A) Strain ε_{xx} B) Strain ε_{yy}

Finite Element Model Description

To predict the corresponding residual stresses, finite element model can be used to simulate the complex geometry of textile composites. The finite element model developed by Karkkainen [123] of the representative volume element for the plain weave composite was used with the adjustment of the dimension and boundary

conditions. The geometry shape of the FE model for the representative volume element (RVE) as shown in Figure 4-8 was taken from a literature source that had documented the dimensions required when constructing the woven pattern [127]. The real dimensions were measured via digital caliper along with the assistance of microscope.

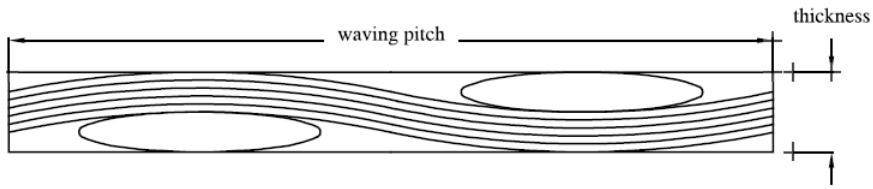

$$\begin{cases} z = 0.1\cos\left(\dfrac{x}{4}\times 2\pi\right) & x \in [0,4](mm) \\ R_a = 1(mm), & R_b = 0.05(mm) \\ h_f = 0.1(mm), & h_m = 0.36(mm) \end{cases}$$

Figure 4-8. Geometry shape

Parametric modeling using Pro/Engineering is used to construct the 3-D structure, which can better simulate the geometry of textile and easily adjust the geometry which are shown in Figure 4-9. By this way, the dimension of the geometry structure can be easily modified to make it close to the real dimension. The CAD file is imported into Abaqus software separately and assembled together. Contact condition between fiber and matrix is defined as glued together under the assumption that no slip occurs between them.

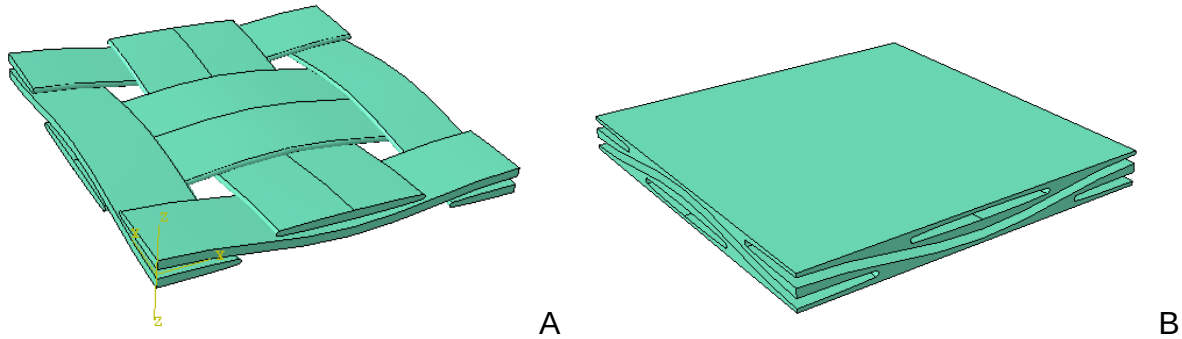

Figure 4-9. Geometry model of fiber and matrix. A) Fiber B) Matrix

Two materials were created within the model for the matrix and the yarns. The yarn was assigned the properties of a unidirectional laminate, AS4/3501-6, taken from experimental data [103]. However, because of the undulation that occurs in the weave, the properties could not be assigned directly to the entire fiber bundle. A local material coordinate system to each element was built to guarantee the laminate properties aligned correctly with the local direction of the fibers. Only one material needed to be defined for the weave by this mean. The temperature dependent properties for the matrix, 3501-6, were taken from the literature [128].

To simulate the curing cycle, the application of temperature and pressure fields were required to simulate both the change in temperature and releasing of the vacuum surrounding the specimen. When the temperature dependent Coefficient of Thermal Expansion (CTE) data was input into the model, the reference temperature was set to be 126.7^{o}C so that any temperature field applied would simulate cooling from the cure temperature. The room temperature conditions were modeled by applying a full field temperature of 22°C and a hydrostatic pressure load of 101.3kPa. To avoid rigid body motion, while allowing full deformations of the model, the center node was fixed in all

three translational directions. All of the material properties used in the model can be found in Table 4-1.

Table 4-1. Material properties used in FE model for plain weave composite RVE

	Temperature (C°)	$E_1(GPa)$	$E_2(GPa)$	$G_{12}(GPa)$	ν_{12}	$\alpha_1(\mu\varepsilon / C^\circ)$	$\alpha_2(\mu\varepsilon / C^\circ)$
AS4/3 501-6	120	138.00	7.67	4.07	0.30	0.59	27.32
	20	138.00	9.34	5.30	0.30	0.45	23.03
3501-6	120	3.10			0.41	52.94	52.94
	20	4.55			0.36	41.30	41.30

The automated strain analysis system provides displacement and strain information at every pixel. Theoretically the full-field displacement data can be input to the FE model to obtain the resulting full-field stress data. However, due to the large number of data points from the experiment and number of nodes in the FE model, the Periodic Boundary Conditions (PBC) was used to import the displacement information as follows:

$$\begin{cases} u_R = u_L + \delta_1, \\ v_R = v_L, \\ u_T = u_B, \\ v_T = v_B + \delta_2, \end{cases} \tag{4-1}$$

where R,L,T,B and δ_1 and δ_2 are the right, left, top, bottom edges and the U and V displacement, respectively. Because the displacements constantly vary throughout the RVE, the average overall displacements were used for each direction. Using this method, the displacements that were used for the model in the U and V directions were $\delta_1 = -2.33\mu m$ and $\delta_2 = -1.75\mu m$ respectively. Those values were achieved by taking the average displacement occurring in each direction along the length of the RVE.

Result of Residual Strain and Stress from FE Model

Figure 4-10 shows the normal strain for the surface elements of matrix within the RVE calculated in ABAQUS. When comparing the corresponding plots in Figure 4-7, the overall trends throughout the surface are in good agreement. The values differ slightly in most regions, but significantly for the area along the fiber bundles. It would not be expected for the results to match perfectly as the FE model didn't account for any chemical shrinkage that would be occurring in the actual specimen. Another possible reason that could cause such a difference would be the amount of resin in the specimen as opposed to that in the FE model. Having low resin content over the fibers would yield higher strains due to the lack of material to support the surrounding compressive strains. Therefore, it does seem reasonable that such a large discrepancy would occur in the values for the maximum tensile strains.

The displacement information obtained from experiment is inputted into the FE model as the PBCs. The residual stress contours are shown in Figure 4-11.

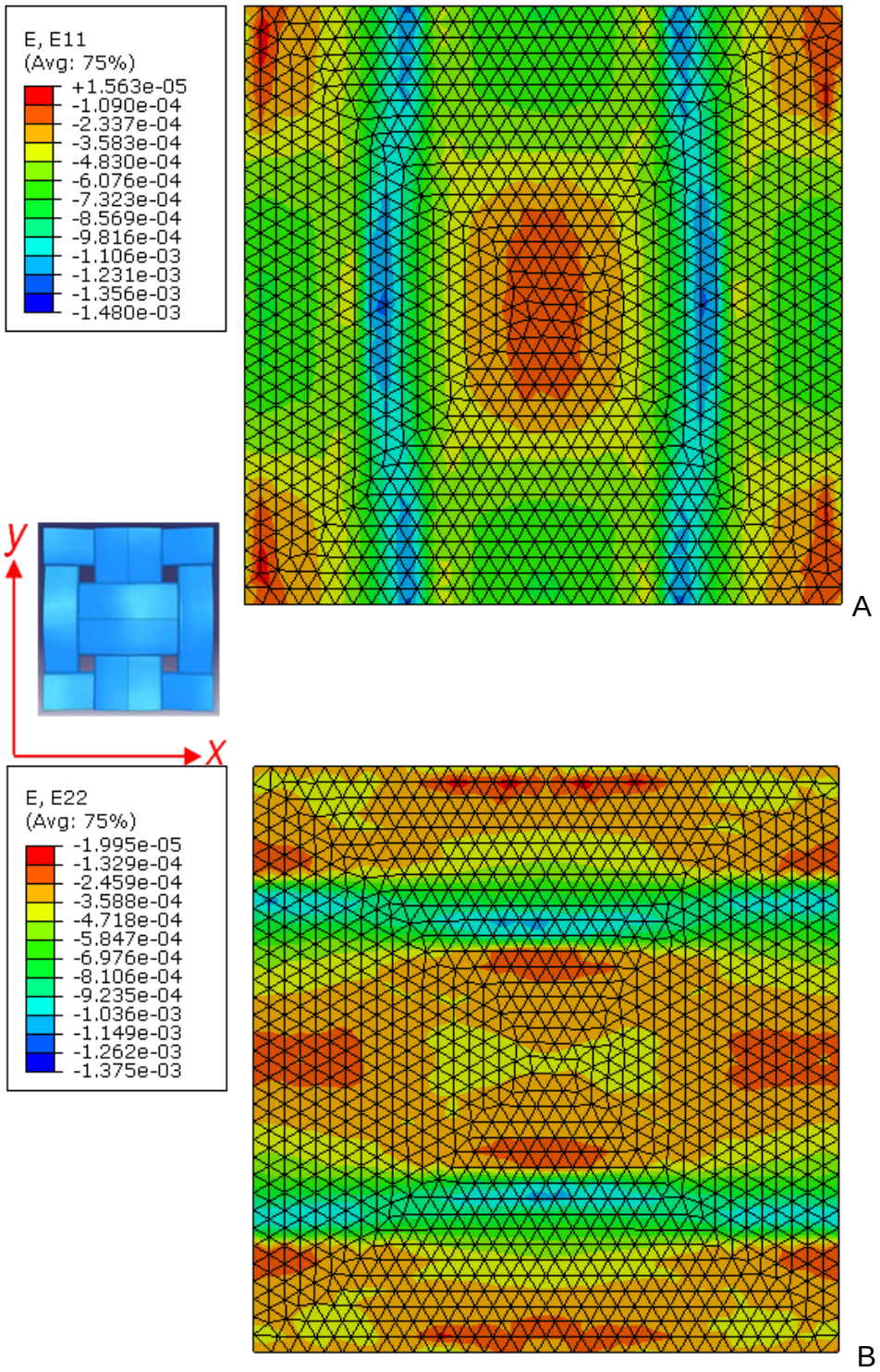

Figure 4-10. Strain map from FE modeling. A) Strain ε_{xx} B) Strain ε_{yy}

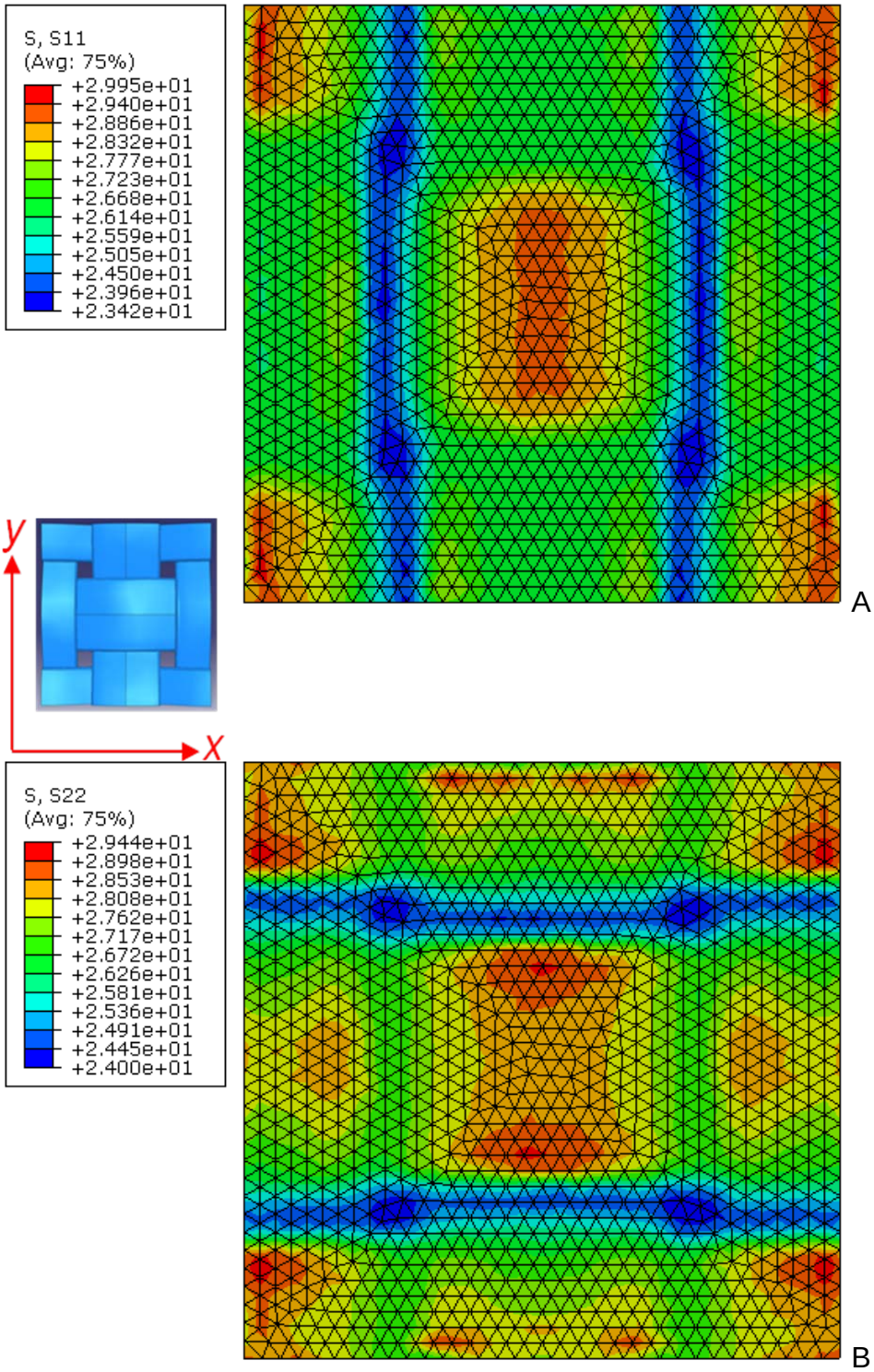

Figure 4-11. Residual stress maps from FE modeling. A) Stress σ_{xx} B) Stress σ_{yy}

From the contours above, it's seen that the residual stress maps have similar color contour maps as residual strains. However, the residual stresses on the surface are all tension with distribution variation. Peak tensile values are occurring over the fiber bundles and the smaller values are within the resin rich areas. The peak tensile stress was approximately 29MPa and that was located in the very center of the RVE over the fiber bundle where the resin content is lowest. Although the values are relatively low, those are the stresses within the resin on the surface. According to the data sheet provided by the prepreg manufacturer, the tensile strength of the resin is 82.7MPa. Although the actual stresses developed were below that value, they are still important to be understood since they limit the usable strength remaining in the structure.

Summary

The improved CRM was utilized to measure the process induced residual strains for the plain weave composite specimen. An automated strain analysis system was developed to calculate the full-field residual strains throughout the entire region of interest. Significant strains were found within the RVE, both in compression and in tension. After examining the strain maps for several specimens, it is seen that fairly repeatable strain values were obtained in the extreme strain regions. A FE model was developed to simulate the curing cycle and the results from the FE model shows similar overall trends as the experiment data. The displacement information obtained from the experiment was inputted to the FE model as PBCs. Residual stresses corresponding to the residual strains were predicted. Although the residual stresses developed were small, they are still important to be understood since they limit the usable strength remaining in the structure.

Shrinkage Measurement of Concrete Material

CRM was used here to determine the shrinkage that develops in concrete during the curing process. A moiré interferometry diffraction grating was replicated on the specimen during the curing process and the specimen was stored in the chamber which controlled specific drying condition for six days after it was demolded. Shrinkage as a function of time, humidity and temperature was measured. During this period, the specimen was removed from the chamber and a quick measurement of shrinkage was made using moiré Interferometry every 24 hours. Consecutive phase shifted fringe patterns were recorded by a digital camera and analyzed using the automated strain analysis system to obtain the full-field strain information.

Introduction

Shrinkage is one of the fundamental characteristics of concrete which mainly results from moisture diffusion and self-desiccation. Moreover, shrinkage depends on many factors, such as water/cement ratio, surrounding relative humidity and temperature, aggregate quantity, and the size and shape of specimen. This crucial characteristic influences the development of stress and induces subsequent cracking of concrete. In order to better assess the structural life of concrete, the shrinkage, which is also time-dependent, must be measured in different drying conditions.

Much research has been devoted to determining the shrinkage that develops in concrete. ASTM C157 is the standard test method for measuring the length change of concrete using comparator [129]. However, this method only measured the averaged shrinkage of concrete and did not provide information on the local area. In 1998, J.K. Kim and C.S. Lee used embedded strain gauges to measure internal shrinkage at the specific location [130]. In 2003, F. Yılmaztürka measured the shrinkage in concrete

samples using digital photogrammetric method [131]. Despite a full field measurement, this optical technique does not have high resolution.

The Curing Reference Method (CRM) was invented in 1996 to determine full-field residual strains that develop as the laminated composite cools via moiré Interferometry [124]. It also could be applied successfully on woven composites [132-134]. Moreover, post-gel chemical shrinkage of epoxy could be determined in the similar principle [133-135]. By using CRM, the in-plane deformation of the concrete can be recorded on a full-field scale. The use of CRM does not reinforce the specimen and avoid destruction of the specimen. Additionally, the grating does not degrade as time. Therefore, time dependent deformation could be measured.

Specimen Preparation

To determine the shrinkage, the full-field of displacement is obtained via moiré Interferometry and the Curing Reference Method. Chen et al. [136] developed an effective procedure to prepare the specimen and take the measurement in the ESA lab. First, a diffraction grating was replicated onto the specimen from a submaster grating while the specimen was at a free stress state. After the specimen was separated from the submaster grating, the submaster grating was used as the reference grating for adjustment of moiré interferometer to obtain null field. Then the specimen was mounted before moiré interferometer and the initial fringe pattern was recorded to determine the initial deformation. Then the specimen was stored in the chamber which provided a specific drying condition for six days. During this period, every 24 hours the specimen was removed from the chamber and a quick measurement was taken to observe how the shrinkage responds to the drying condition. The diffraction grating used had a

frequency of 1200 lines/mm. The detail of the procedure for the grating replication can be found in reference [136].

In the experiment, a 100% air tight food storage container was used as the chamber. Sufficient desiccates were put into the container to create nearly 0% relative humidity (RH) inside. On the other hand, 100% RH was easily created by replacing desiccates with some water. 50% RH is room relative humidity. As to temperature control, the oven and refrigerator were used to provide 40°C and 5°C respectively.

Result for Cement without Aggregate

The cement paste specimens with w/c ratio=0.5 were used for the testing to determine the shrinkage under different drying environment.

For each test, both U and V field were recorded to show similar deformation in both x and y direction because of symmetric condition. Figure 4-12~13 shows the fringe patterns for U and V field under 50% RH and room temperature (23°C).

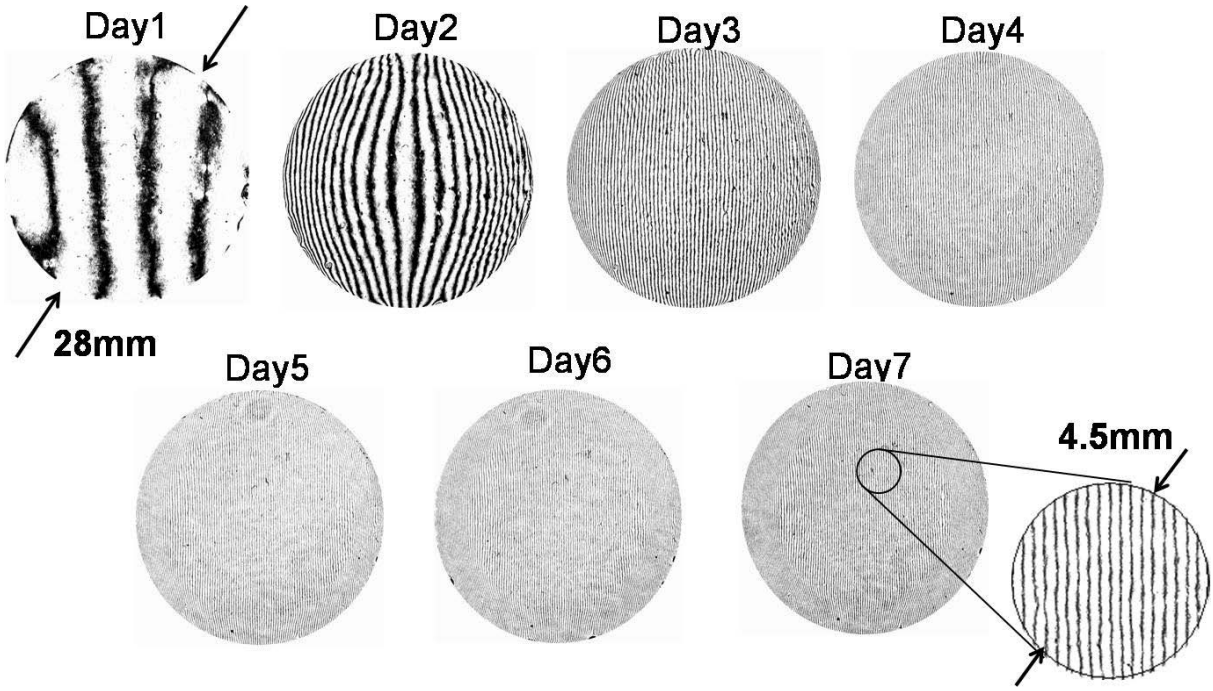

Figure 4-12. U field under 50% RH and 23°C

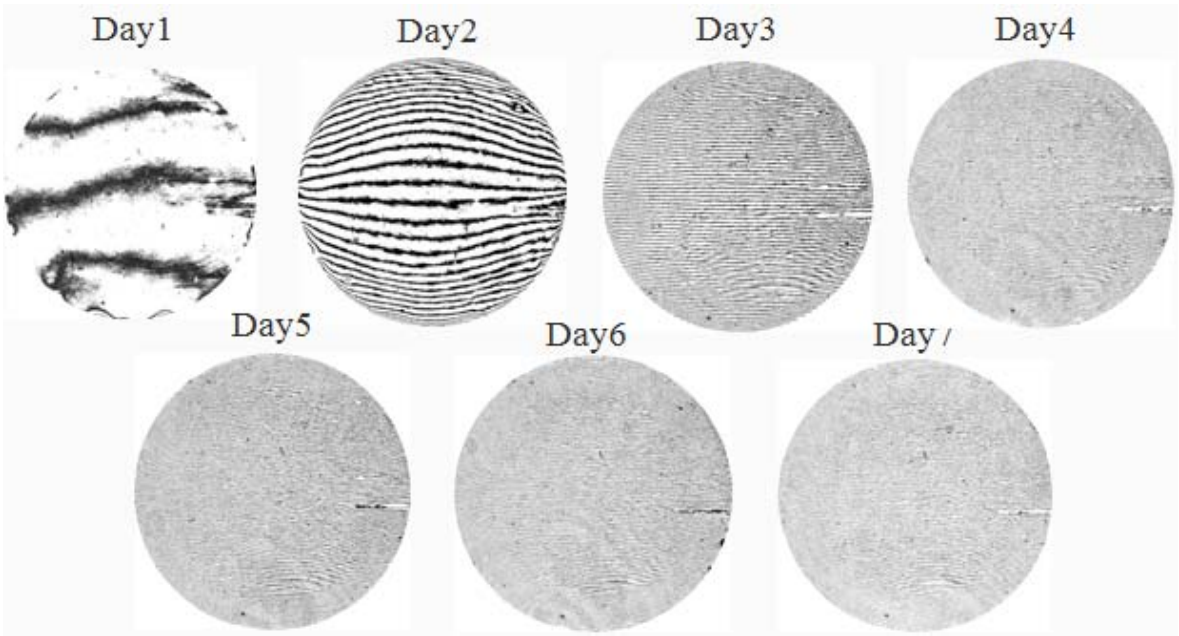

Figure 4-13. V field under 50% RH and 23°C

Automated strain analysis system was used to analyze the fringe patterns to obtain the full-field displacements and strains for each day. Figure 4-14~15 only shows the full-field displacements on day2 for both U and V field under RH=50% and 23°C.

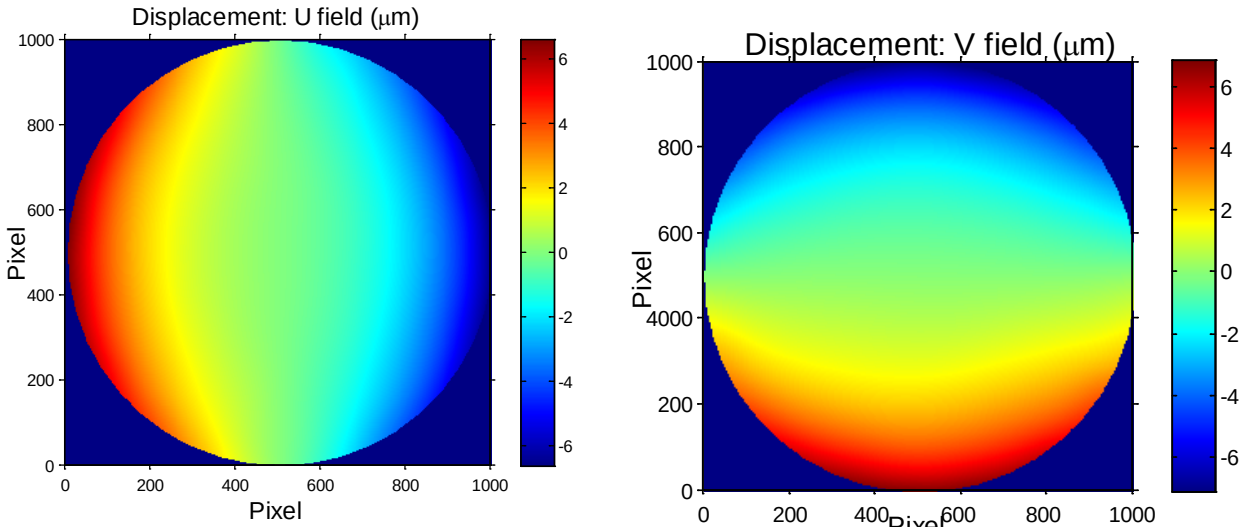

Figure 4-14. Displacement field in the Rectangular Coordinate system for day 2

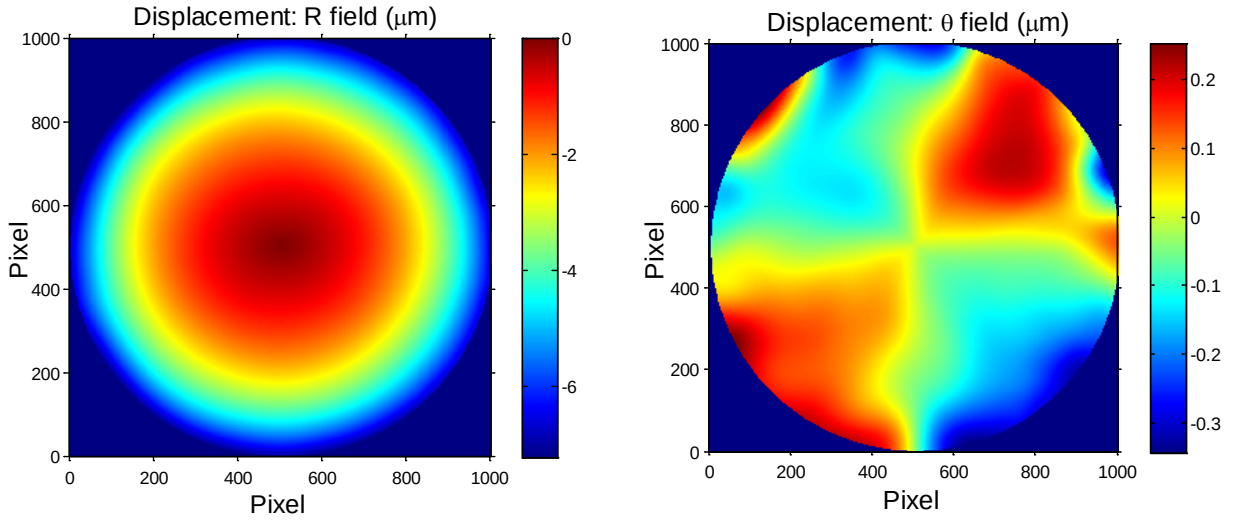

Figure 4-15. Displacement field in the Polar Coordinate system for day 2

Figure 4-16~17 shows the corresponding strain field in both coordinate systems. Again, the results from U and V field are very similar because of the symmetry.

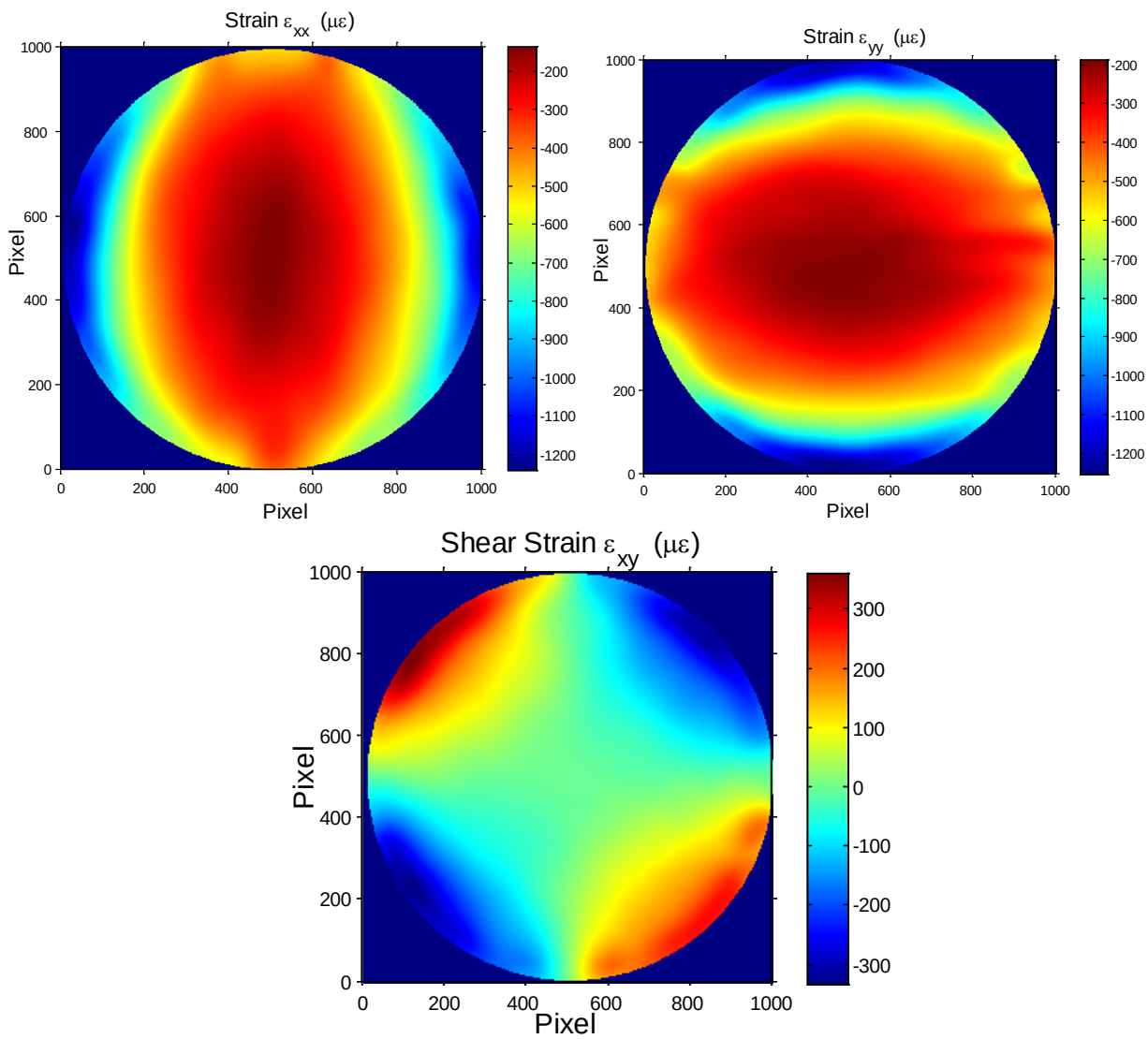

Figure 4-16. Strain field in the Rectangular Coordinate system for day 2

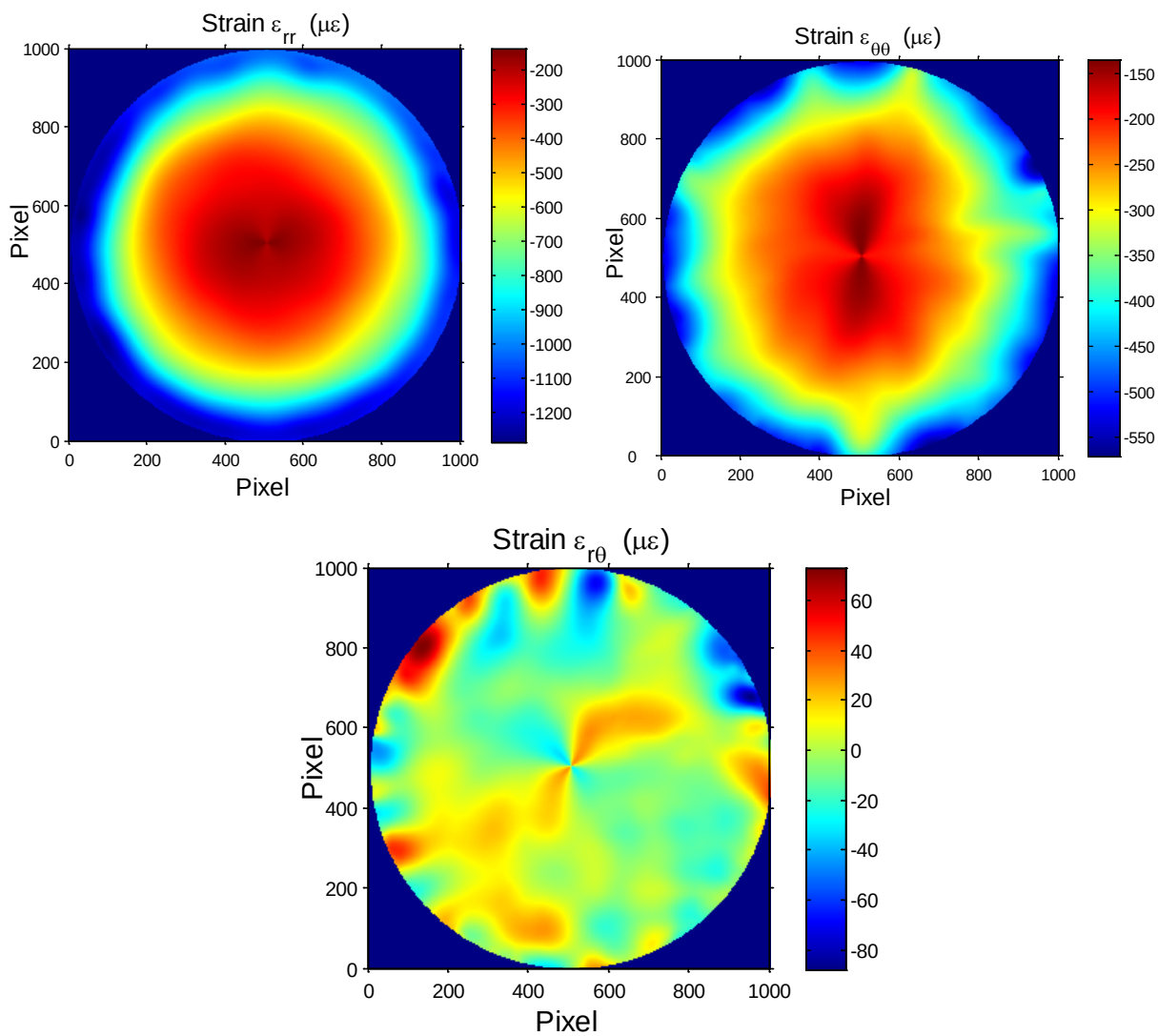

Figure 4-17. Strain field in the Polar Coordinate system for day 2

Fig. 4-18 shows the shrinkage data from the center of the specimen to the expose surface from day 2 to day 7 under RH=50% and 23°C. Clearly, shrinkage is larger in the area close to the exposed surface than that in the center. This is due to faster drying in the area close to the exposed surface. For RH=0%, the result has the same trend as RH=50% except for larger shrinkage.

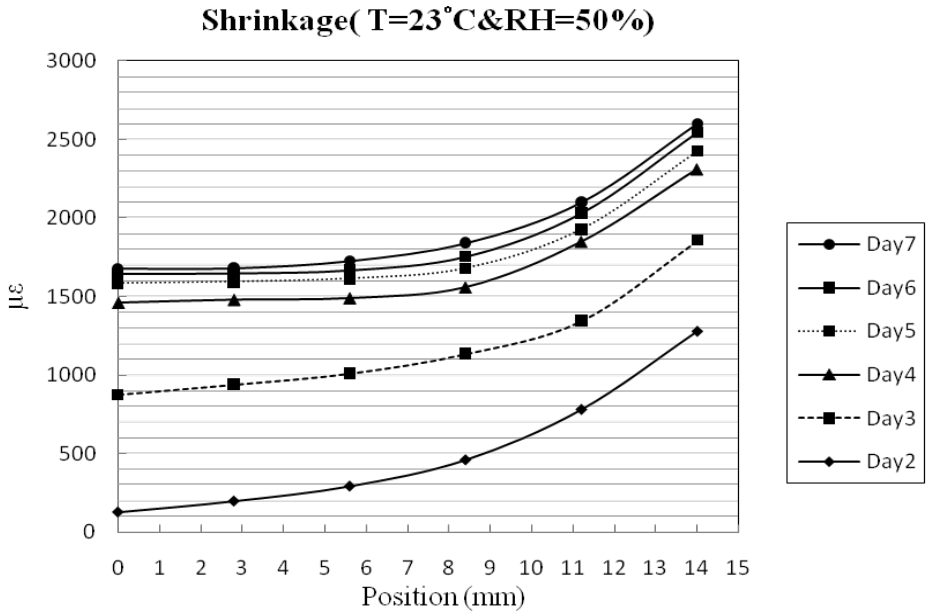

Figure 4-18. Shrinkage from center to expose surface

In the same experimental and analytical technique, temperature effect was also investigated. The fringe patterns are not shown here. Fig. 4-19~20 shows the results for temperature and relative humidity effect on the shrinkage of concrete specimens in average sense.

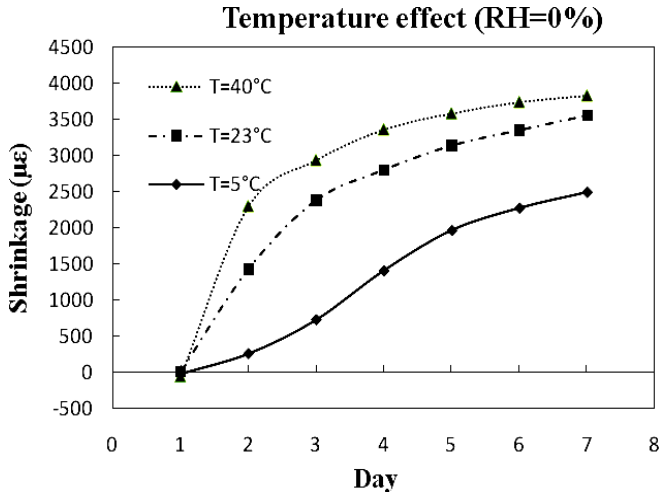

Figure 4-19. Temperature effect

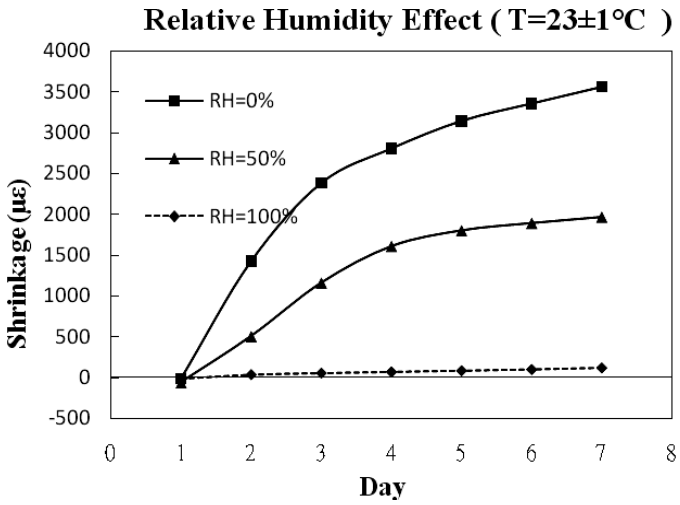

Figure 4-20. Relative humidity effect

Result for Cement with Coarse Aggregate

Gravel was embedded into cement paste (w/c=0.5) close to the grating, but did not contact with the grating. The arrangement of the gravel is shown as Figure 4-21 with a side view and top view. The specimen was stored in relative humidity 0% and room temperature.

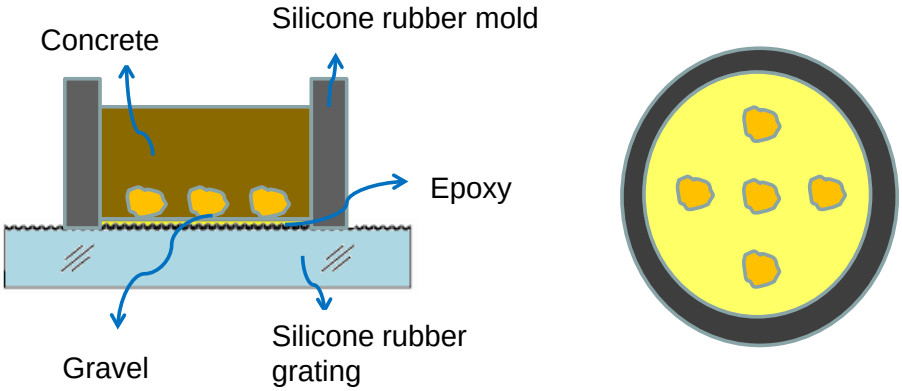

Figure 4-21. The side and top views of gravel test

Moiré fringe patterns from Day 1 to Day 5 were recorded. Only day 5 moiré fringe patterns are shown here in Figure 4-22. There were some areas of lower fringe density marked by blue boxes. These areas corresponded to the locations of the embedded

gravels. A crack occurred within the area of the red circle. This was due to the constraint from the embedded gravel.

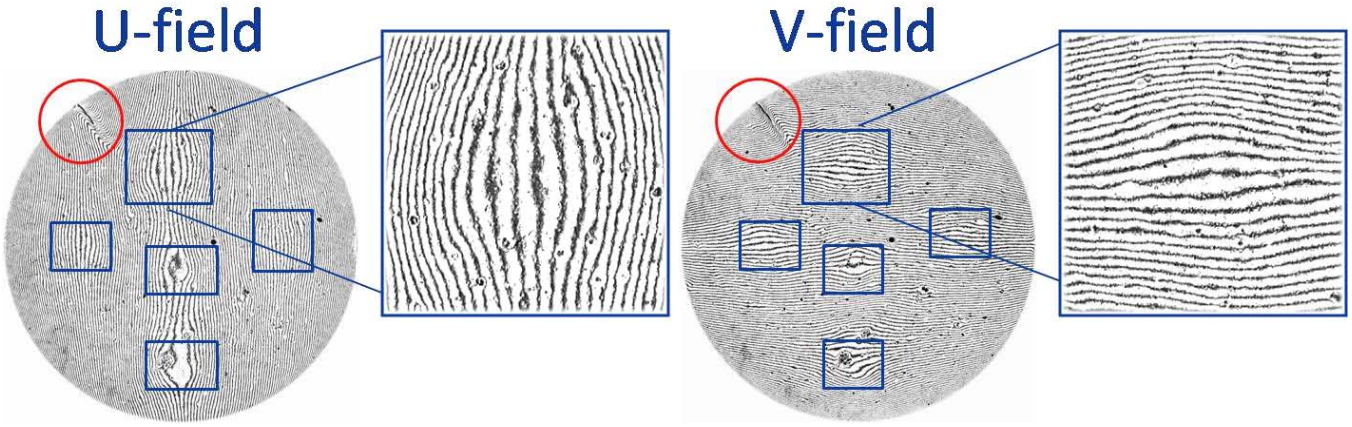

Figure 4-22. Day 5 moiré fringe patterns for the gravel test

Normal strain analysis was performed in Figure 4-23. Clearly, the locations of gravel show lower shrinkage. The plots just displayed the normal strain distributions along the horizontal centerline in U field and the vertical centerline in V field. More result for cement with fine aggregate can be found in [137].

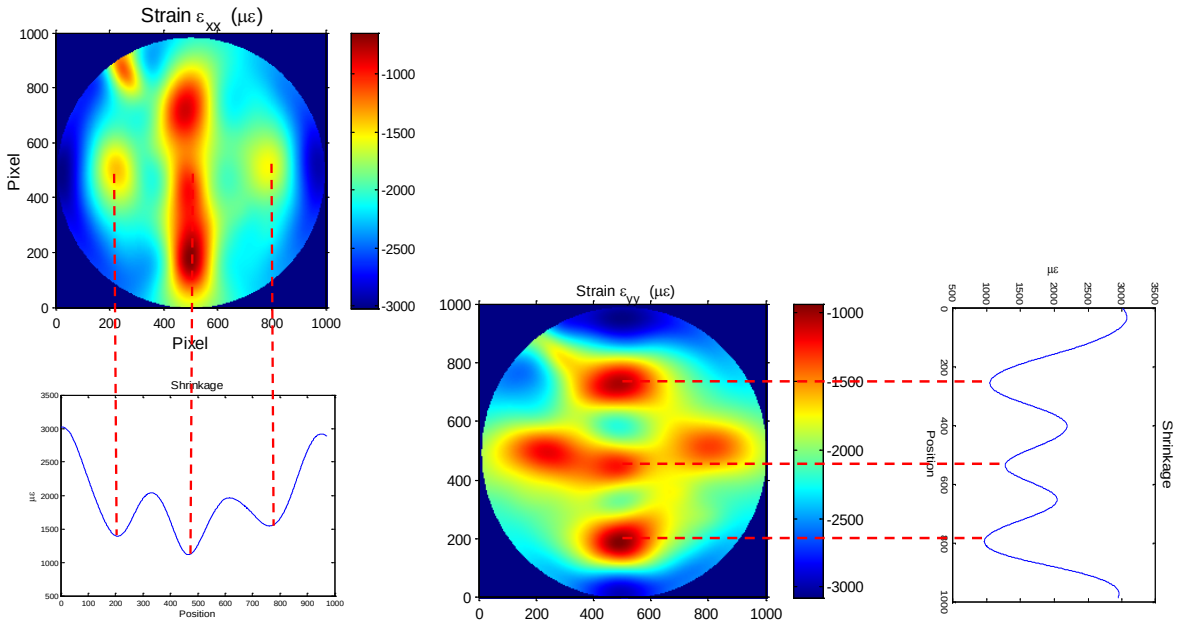

Figure 4-23. The normal strain analysis for gravel test

Summary

The experimental technique for measuring the shrinkage of concrete has been developed based on curing reference method and moiré interferometry. The automated strain analysis system was applied to obtain the full-field displacement and strain maps successfully. The experimental data show that the shrinkage of concrete increases with time and is very sensitive to surrounding environment. It increases with temperature. And a decrease in relative humidity also increases the shrinkage. This experimental method was also employed to investigate the effect of coarse or fine aggregate on shrinkage of concrete. Different quantities of sands can be added to cement paste to see how shrinkage behaves. A numerical model can be developed in order to obtain material properties from the complex geometry used in our test.

Material Property Identification of Laminate Using Full Field Measurements

This section covers the cooperation work with Chiristian Gogu. The objective is to identify the four ply-elastic constants $E_1, E_2, G_{12}, \nu_{12}$ from the moiré full-field displacement measurements on a laminate plate with a hole using Bayesian identification approach. Only the experiment part is covered here. All the details of material property identification can be found in [138].

Introduction

Identification of the four orthotropic elastic constants of a composite from a tensile test on a plate with a hole was carried out by several authors in the past [139-140] using finite element model updating based on a least squares framework. Some of the advantages of doing the identification from measurements on a plate with a hole are the ability to identify all four properties at the same time from a single experiment. This is possible because of the heterogeneous strain field exhibited during this test which

involves all four elastic constants, unlike tension tests on simple rectangular specimen which exhibit uniform strain fields and usually involve only two of the elastic constants. A further advantage is that the heterogeneous fields can provide information on spatial variations of the material properties as well. Moiré interferometry was used to capture the displacement non-uniformity on the specimen used for identification because of its high spatial resolution.

The objective is to use Bayesian identification to for identification of the four ply-elastic constants from the full-field displacement measurements on a laminate plate with a hole. The interest of identifying ply properties is that it allows to obtain both the extensional and the bending stiffnesses of the laminate. Due however to the varying sensitivity of the strain and displacement fields to the different ply properties, it is of primary importance to estimate the uncertainty with which these properties are identified. The Bayesian approach developed by Gogu [138] will allow us to do this by taking into account the physics of the problem (i.e. the different sensitivities of the fields to the different properties), measurement uncertainty as well as uncertainty on other input parameters to the model such as the specimen geometry.

The experiment considered for the identification is a tensile test on a composite plate with a hole. The laminate is made of graphite/epoxy with a stacking sequence of $[45, -45, 0]_s$. The plate has the dimensions given in Figure 4-24, with a ply thickness of 0.16 mm. The applied tensile force is 1200 N. The full-field measurement takes place on a square area 20 x 20 mm^2 around center of the hole.

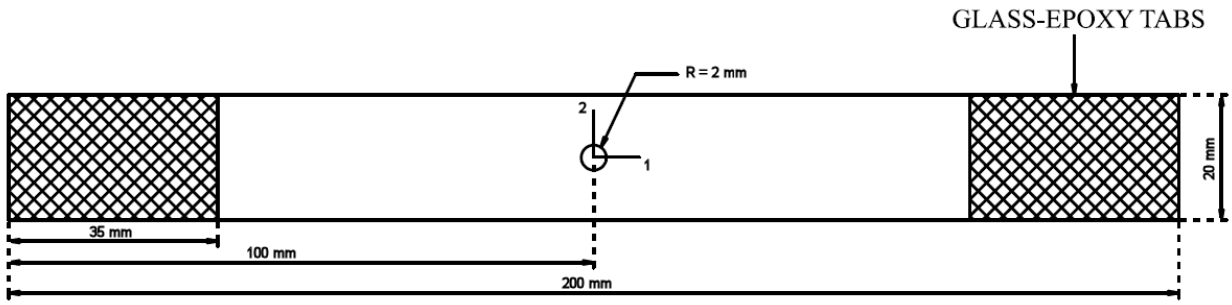

Figure 4-24. Specimen geometry. The specimen material is graphite/epoxy and the stacking sequence $[45, -45, 0]_s$

Experiment

The dimension of the test specimen is slightly different from the designed. The width of the specimen was 24.3 mm, the diameter of the hole was 4.10 mm, and the total laminate thickness was 0.78mm. The plate was made out of a Toray® T800/3631 graphite/epoxy prepreg. The manufacturer's specifications for this material are given in Table 4-2 together with the properties obtained by Noh [141]. Noh obtained the material properties based on a four points bending test at the University of Florida on a composite made from the exact same prepreg roll that we used.

Table 4-2. Manufacturer's specifications and properties found by Noh (2004) based on a four points bending test

Parameter	E_1(GPa)	E_2(GPa)	G_{12}(GPa)	v_{12}
Manufacture's specification	162	7.58	4.41	0.34
Noh (2004) values	144	7.99	7.78	0.34

A picture of our specimen with the diffraction grating (1200 lines/mm) is shown in Figure 4-25. The specimen was loaded at 700 N for the measurements to consider the safety of the material.

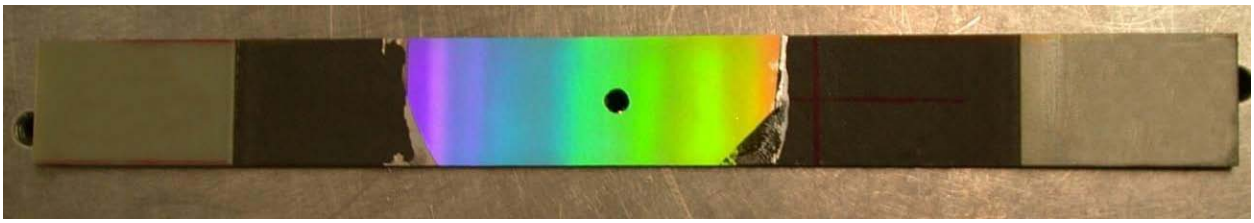

Figure 4-25. Test specimen with grating (1200 lines/mm)

The experiment setup is shown in Figure 4-26. PEMI II 2020-X Moiré interferometer using a Pulnix TM-1040 digital camera were utilized to capture phase shifted fringe patterns. MTI-30K machine was used to apply tension load. Rotations of the grips holding the specimen were allowed by using a lubricated ball bearing for the bottom grip and two lubricated shafts for the top grip. This allowed reducing parasitic bending during the tension test.

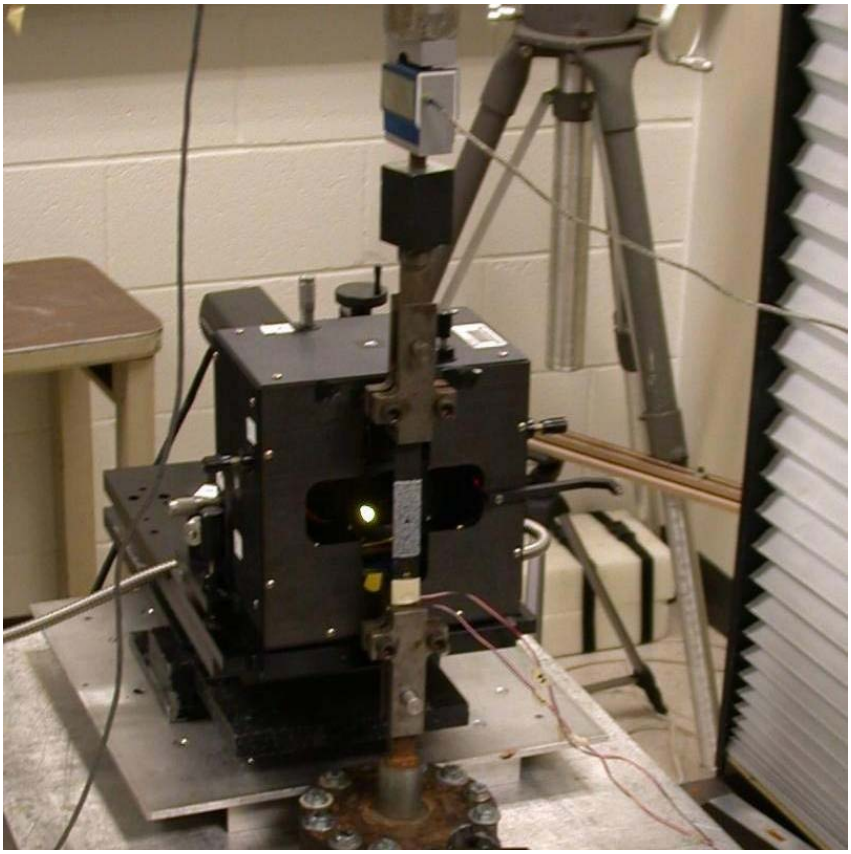

Figure 4-26. Experimental setup

Fringe Patterns and Result

The fringe patterns observed for a force of 700 N are shown in Figures 4-27. The two smaller holes in the fringe patterns and other parasitic lines are due to imperfections in the diffraction grating such as air bubbles and dust from the cover magic Scott tapes.

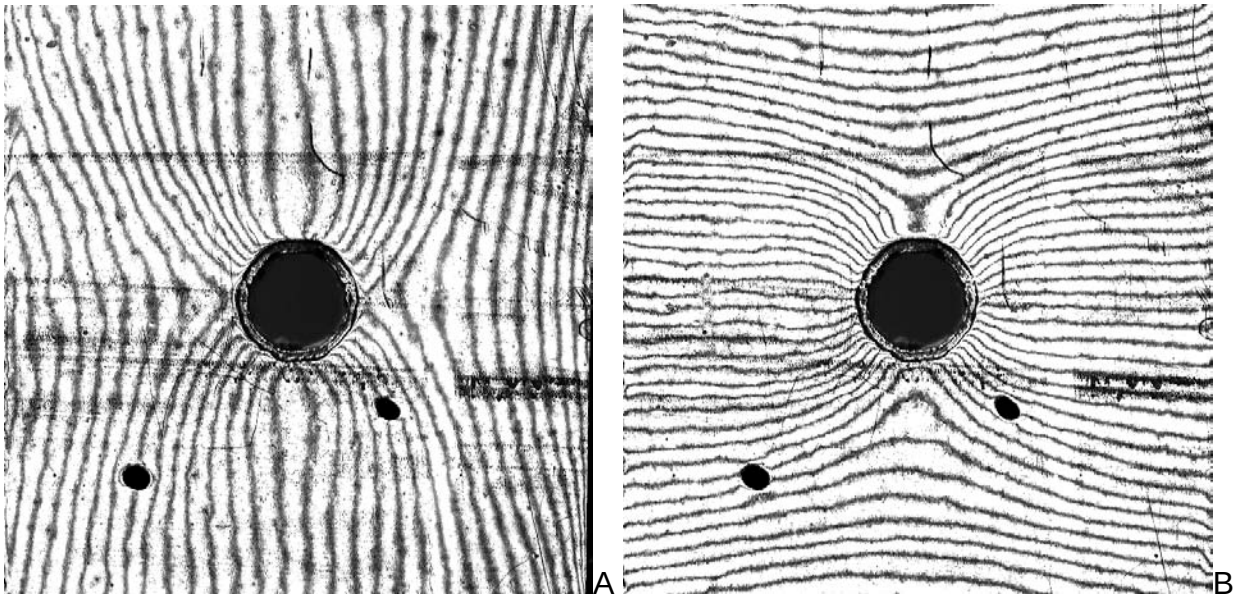

Figure 4-27. Fringe patterns. A) U field B) V field

The automated strain analysis system was used to analyze the fringe patterns and extract the displacement fields. The corresponding displacement maps are shown in Figures 4-28. Both of the U and V field displacement maps will be used in the Bayesian identification procedure.

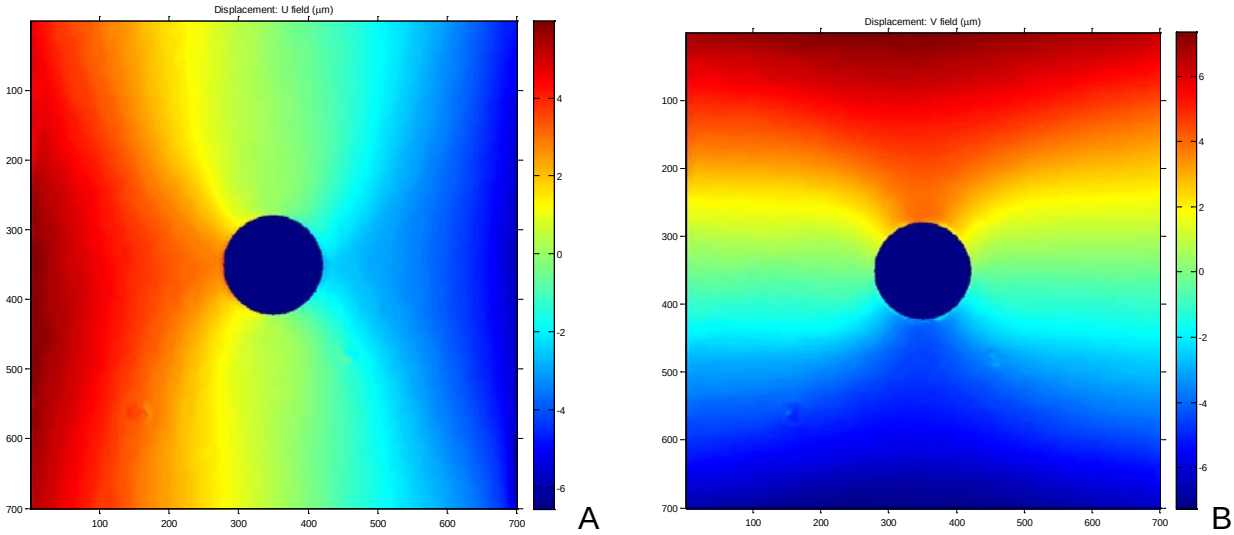

Figure 4-28. Displacement maps. A) U field B) V field

The results of the identification are provided in Tables 4-3.

Table 4-3. Mean values and coefficient of variation of the identified posterior distribution from the Moiré interferometry experiment

Parameter	E_1(GPa)	E_2(GPa)	G_{12}(GPa)	v_{12}
Mean value	138	7.48	5.02	0.33
COV (%)	3.12	9.46	4.29	10.3

Although strain maps are not necessary for the material property identification procedure, the strain maps obtained from the automated strain analysis system are shown in Figure 4-29. They have good agreement with those obtained in FE simulation for most the areas except the extremely large values close to the edges.

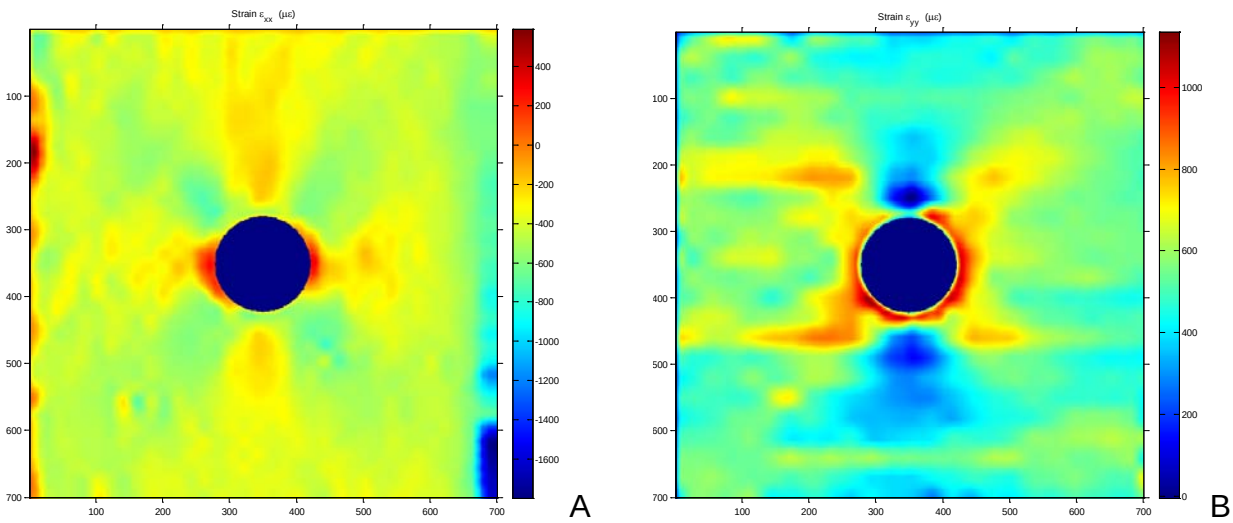

Figure 4-29. Strain maps. A) Strain ε_{xx} B) Strain ε_{yy}

Summary

Overall the mean values of the identified distribution are in agreement with the manufacturer's specifications. The largest difference is in longitudinal Young's modulus, which could seem somewhat surprising. However Noh[141] found a similar value on the exact same prepreg roll that we used. The mean values of E_2, v_{12} and G_{12} are close to the specification values. G_{12} is far however from Noh's values but it should be noted that the four point bending test is relatively poor for identifying G_{12}.

Summary

In the present chapter, selected three applications of Automated Strain Analysis System in the ESA lab were introduced and the results were illustrated. The system together with moiré interferometry can give accurate measurement of residual strain of textile composite and shrinkage of concrete material, and provide accurate displacement data for material property identification of laminate.

CHAPTER 5
CONCLUSIONS AND SUGGESTED FUTURE WORK

Conclusions

Moiré interferometry has been widely applied for industrial and scientific studies because of its capability of full-field displacement measurement, high sensitivity and high spatial resolution. The output of moiré is represented as interference fringe patterns which need to be analyzed to obtain the desired physical parameters such as displacement, strain, etc. Traditionally, the fringe pattern was analyzed manually via drawing the gage lines on some points and counting the number of fringes crossing them. To improve the efficiency of the experiments using moiré interferometry and enhance the accuracy of the fringe pattern analysis, an automated strain analysis system was developed in this dissertation.

The major contributions in this dissertation include:

- Complete survey and investigation on the existing image processing techniques for fringe pattern analysis; appropriate algorithms were adopted and improved.
- Implementation of the quality guided phase unwrapping
- Improvement of the quality guided phase unwrapping; enhancement of the efficiency of the algorithm for application of large image
- Development of phase repair for the inconsistent areas
- Development of automatic detection of the inconsistent areas
- Development of the hybrid method O/DFM.
- Development of global surface fit to calculate strain effectively
- Development of local surface fit to calculate strain effectively

- Development of a Windows GUI based software “Automated Strain Analysis System” using MatLab 2009 for automatic fringe pattern analysis. This software includes all the algorithms covered in the dissertation. It also includes some useful tools for post-processing of the data.
- Application of the system for residual stress characterization of plain woven textile composite.
- Application of the system for shrinkage measurement of concrete materials without and with aggregate.
- Application of the system for material property identification of laminate using open-hole test.

Suggested Future Work

So far the automated strain analysis system has been successfully applied for several projects in the ESA lab. Although some preliminary results were obtained, the following tasks may be completed in the future,

- Enhancement of the computational efficiency of global surface fit using thin plate spline. With the increased number of seed points on those areas close to the edge, it will calculate the strain within those areas better.
- Improvement of the algorithm for the automatic detection of inconsistent areas in the unwrapped phase map.

APPENDIX A
BILINEAR FUNCTION FOR LOCAL SURFACE FIT BASED STRAIN CALCULATION

Bilinear function can be used to fit the 2D data within small patches. The unwrapped phase is assumed to have the bilinear distribution within one patch as shown in Equation (A-1)

$$f\left(i, j\right) = c_1 + c_2 i + c_3 j + c_4 ij \tag{A-1}$$

where $f\left(i, j\right)$ is the smoothed unwrapped phase. i, j is the image coordinate system with unit of pixel. c_1, c_2, c_3, c_4 are the coefficients calculated from the surface fit.

All the points within the patch of size $m \times n$ pixels are used to form the equation group,

$$\begin{cases} f_1\left(i_1, j_1\right) = c_1 + c_2 i_1 + c_3 j_1 + c_4 i_1 j_1 \\ f_2\left(i_2, j_2\right) = c_1 + c_2 i_2 + c_3 j_2 + c_4 i_2 j_2 \\ \ldots\ldots \\ f_{mn}\left(i_{mn}, j_{mn}\right) = c_1 + c_2 i_{mn} + c_3 j_{mn} + c_4 i_{mn} j_{mn} \end{cases} \tag{A-2}$$

$\left[B\right]_{mn,4}$, $\left[C\right]_{4,1}$ and $\left[Y\right]_{mn,1}$ matrix can be formed,

$$\left[B\right]_{mn,4} = \begin{bmatrix} 1 & i_1 & j_1 & i_1 j_1 \\ 1 & i_2 & j_2 & i_2 j_2 \\ & \ldots\ldots & & \\ 1 & i_{mn} & j_{mn} & i_{mn} j_{mn} \end{bmatrix} \tag{A-3}$$

$$\left[C\right]_{4,1} = \begin{Bmatrix} c_1 \\ c_2 \\ c_3 \\ c_4 \end{Bmatrix} \tag{A-4}$$

$$[Y]_{mn,1} = \begin{Bmatrix} f_1(i_1, j_1) \\ f_2(i_2, j_2) \\ \ldots\ldots \\ f_{mn}(i_{mn}, j_{mn}) \end{Bmatrix} \tag{A-5}$$

Then the coefficients can be calculated as,

$$[C] = \left[B^T B\right]^{-1} \left[B^T Y\right] \tag{A-6}$$

Finally the gradients (strains) can calculated analytically as,

$$\begin{cases} \dfrac{\partial f}{\partial x} = \dfrac{\partial f}{\partial j}(i, j) = c_3 + c_4 i \\ \dfrac{\partial f}{\partial y} = -\dfrac{\partial f}{\partial i}(i, j) = -(c_2 + c_4 j) \end{cases} \tag{A-7}$$

The negative sign expression of $\partial f / \partial y$ comes from the opposite direction in image system and rectangular coordinate system.

APPENDIX B
CUBIC FUNCTION FOR LOCAL SURFACE FIT BASED STRAIN CALCULATION

Cubic function can be used to fit the 2D data within small patches. The unwrapped phase is assumed to have the cubic distribution within one patch as shown in Equation (B-1)

$$f\left(i,j\right)=c_1+c_2i+c_3j+c_4ij+c_5i^2+c_6j^2+c_7i^3+c_8i^2j+c_9ij^2+c_{10}j^3 \qquad \text{(B-1)}$$

where $f\left(i,j\right)$ is the smoothed unwrapped phase. i,j is the image coordinate system with unit of pixel. $c_1,c_2,c_3,c_4,c_5,c_6,c_7,c_8,c_9,c_1$ are the coefficients calculated from the surface fit.

All the points within the patch of size $m\times n$ pixels are used to form the equation group,

$$\begin{cases} f_1\left(i_1,j_1\right)=c_1+c_2i_1+c_3j_1+c_4i_1j_1+c_5i_1^2+c_6j_1^2+c_7i_1^3+c_8i_1^2j_1+c_9i_1j_1^2+c_{10}j_1^3 \\ f_2\left(i_2,j_2\right)=c_1+c_2i_2+c_3j_2+c_4i_2j_2+c_5i_2^2+c_6j_2^2+c_7i_2^3+c_8i_2^2j_2+c_9i_2j_2^2+c_{10}j_2^3 \\ \ldots\ldots \\ f_{mn}\left(i_{mn},j_{mn}\right)=c_1+c_2i_{mn}+c_3j_{mn}+c_4i_{mn}j_{mn}+c_5i_{mn}^2+c_6j_{mn}^2+c_{mn}i^3+c_8i_{mn}^2j_{mn}+c_9i_{mn}j_{mn}^2+c_{10}j_{mn}^3 \end{cases} \qquad \text{(B-2)}$$

$\left[B\right]_{mn,10}$, $\left[C\right]_{10,1}$ and $\left[Y\right]_{mn,1}$ matrix can be formed,

$$\left[B\right]_{mn,10}=\begin{bmatrix} 1 & i_1 & j_1 & i_1j_1 & i_1^2 & j_1^2 & i_1^3 & i_1^2j_1 & i_1j_1^2 & j_1^3 \\ 1 & i_2 & j_2 & i_2j_2 & i_2^2 & j_2^2 & i_2^3 & i_2^2j_2 & i_2j_2^2 & j_2^3 \\ & & & & \ldots\ldots & & & & & \\ 1 & i_{mn} & j_{mn} & i_{mn}j_{mn} & i_{mn}^2 & j_{mn}^2 & i_{mn}^3 & i_{mn}^2j_{mn} & i_{mn}j_{mn}^2 & j_{mn}^3 \end{bmatrix} \qquad \text{(B-3)}$$

$$[C]_{10,1} = \begin{Bmatrix} c_1 \\ c_2 \\ c_3 \\ c_4 \\ c_5 \\ c_6 \\ c_7 \\ c_8 \\ c_9 \\ c_{10} \end{Bmatrix} \tag{B-4}$$

$$[Y]_{mn,1} = \begin{Bmatrix} f_1(i_1, j_1) \\ f_2(i_2, j_2) \\ \ldots\ldots \\ f_{mn}(i_{mn}, j_{mn}) \end{Bmatrix} \tag{B-5}$$

Then the coefficients can be calculated as,

$$[C] = \left[B^T B\right]^{-1} \left[B^T Y\right] \tag{B-6}$$

Finally the gradients (strains) can calculated analytically as,

$$\begin{cases} \dfrac{\partial f}{\partial x} = \dfrac{\partial f}{\partial j}(i, j) = c_3 + c_4 i + 2c_6 j + c_8 i^2 + 2c_9 ij + 3c_{10} j^2 \\ \dfrac{\partial f}{\partial y} = -\dfrac{\partial f}{\partial i}(i, j) = -\left(c_2 + c_4 j + 2c_5 i + 3c_7 i^2 + 2c_8 ij + c_9 j^2\right) \end{cases} \tag{B-7}$$

The negative sign expression of $\partial f / \partial y$ comes from the opposite direction in image system and rectangular coordinate system.

LIST OF REFERENCES

1. D. Post, B. Han and P. Ifju, *High Sensitivity Moire: Experimental Analysis for Mechanics and Materials*, Springer-Verlag, New York (1994).

2. A. Livnat and D. Post, "The Governing Equations for Moire Interferometry and Their Identity to Equations of Geometrical Moire," *Exp Mech* 25(4), 360-366 (1985)

3. G. Peacock, *Miscellaneous Works of the Late Thomas Young*, John Murray Publishers, London (1855).

4. J. Dyson, "The Rapid Measurement of Photographic Records of Interference Fringes," *Appl Optics* 2(5), 487-489 (1963)

5. G. D. Dew, "Method for Precise Evaluation of Interferograms," *J Sci Instrum* 41(3), 160-165 (1964)

6. A. F. Bastawros and A. S. Voloshin, "Thermal Strain Measurements in Electronic Packages through Fractional Fringe Moire Interferometry," *Journal of Electronic Packaging, Trans. ASME* 112(4), 303-308 (1990)

7. T. Kreis, *holographic interferometry*, Academic Verlag, Berlin (1996).

8. D. Malacara, M. Servin and Z. Malacara, *Interferogram analysis for optical testing*, Marcel Dekker Inc., New York (1998).

9. A. Jain, *Fundamentals of digital image processing*, Prentice-Hall International Inc., London (1989).

10. G. Jin, *Computer-aided optical measurements*, Tsinghua University Press, Beijing (1997).

11. T. Yatagai, "Intensity based analysis methods. In Interferogram Analysis (Eds D.W. Robinson and G.T. Reid)," 73-93 (1993)

12. T. Yatagai, S. Nakadate, M. Idesawa and H. Saito, "Automatic Fringe Analysis Using Digital Image-Processing Techniques," *Opt Eng* 21(3), 432-435 (1982)

13. G. A. Mastin and D. C. Ghiglia, "Digital Extraction of Interference Fringe Contours," *Appl Optics* 24(12), 1727-1728 (1985)

14. T. Y. Chen and C. E. Taylor, "Computerized Fringe Analysis in Photomechanics," *Exp Mech* 29(3), 323-329 (1989)

15. F. Bertolino and F. Ginesu, "Semiautomatic Approach of Grating Techniques," *Opt Laser Eng* 19(4-5), 313-323 (1993)

16. A. E. Ennos, D. W. Robinson and D. C. Williams, "Automatic Fringe Analysis in Holographic-Interferometry," *Opt Acta* 32(2), 135-145 (1985)

17. S. Krishnaswamy, "Algorithm for Computer Tracing of Interference-Fringes," *Appl Optics* 30(13), 1624-1628 (1991)

18. J. A. Aparicio, J. L. Molpeceres, A. M. Defrutos, C. Decastro, S. Caceres and F. A. Frechoso, "Improved Algorithm for the Analysis of Holographic Interferograms," *Opt Eng* 32(5), 963-969 (1993)

19. D. S. Zhang, M. Ma and D. D. Arola, "Fringe skeletonizing using an improved derivative sign binary method," *Opt Laser Eng* 37(1), 51-62 (2002)

20. D. S. Zhang, D. D. Arola and M. Ma, "Digital image processing of moire fringe patterns with an application to fractures in bovine dentin," *Opt Eng* 41(5), 1115-1121 (2002)

21. B. T. Han, "Interferometric Methods with Enhanced Sensitivity by Optical Digital Fringe Multiplication," *Appl Optics* 32(25), 4713-4718 (1993)

22. A. Rosenfeld, "Characterization of Parallel Thinning Algorithms," *Inform Control* 29(3), 286-291 (1975)

23. A. Rosenfeld and A. Kak, *Digital picture processing, Vol. I*, Academic Press, New York (1982).

24. J. B. Schemm and C. M. Vest, "Fringe Pattern-Recognition and Interpolation Using Non-Linear Regression-Analysis," *Appl Optics* 22(18), 2850-2853 (1983)

25. A. Colin and W. Osten, "Automatic Support for Consistent Labeling of Skeletonized Fringe Patterns," *J Mod Optic* 42(5), 945-954 (1995)

26. W. W. Macy, "Two-Dimensional Fringe-Pattern Analysis," *Appl Optics* 22(23), 3898-3901 (1983)

27. P. L. Ransom and J. V. Kokal, "Interferogram Analysis by a Modified Sinusoid Fitting Technique," *Appl Optics* 25(22), 4199-4204 (1986)

28. T. Yatagai, "Automated Fringe Analysis Techniques in Japan," *Opt Laser Eng* 15(2), 79-91 (1991)

29. M. Takeda, H. Ina and S. Kobayashi, "Fourier-Transform Method of Fringe-Pattern Analysis for Computer-Based Topography and Interferometry," *J Opt Soc Am* 72(1), 156-160 (1982)

30. K. H. Womack, "Frequency-Domain Description of Interferogram Analysis," *Opt Eng* 23(4), 396-400 (1984)

31. D. J. Bone, H. A. Bachor and R. J. Sandeman, "Fringe-Pattern Analysis Using a 2-D Fourier-Transform," *Appl Optics* 25(10), 1653-1660 (1986)

32. T. Kreis, "Digital Holographic Interference-Phase Measurement Using the Fourier-Transform Method," *J Opt Soc Am A* 3(6), 847-855 (1986)

33. C. Roddier and F. Roddier, "Interferogram Analysis Using Fourier-Transform Techniques," *Appl Optics* 26(9), 1668-1673 (1987)

34. R. J. Green, J. G. Walker and D. W. Robinson, "Investigation of the Fourier-Transform Method of Fringe Pattern-Analysis," *Opt Laser Eng* 8(1), 29-44 (1988)

35. K. Freischlad and C. L. Koliopoulos, "Fourier Description of Digital Phase-Measuring Interferometry," *J Opt Soc Am A* 7(4), 542-551 (1990)

36. D. Tentori and D. Salazar, "Hologram Interferometry - Carrier Fringes," *Appl Optics* 30(35), 5157-5158 (1991)

37. P. J. Bryanstoncross, C. Quan and T. R. Judge, "Application of the Fft Method for the Quantitative Extraction of Information from High-Resolution Interferometric and Photoelastic Data," *Opt Laser Technol* 26(3), 147-155 (1994)

38. J. Gu and F. Chen, "Fast Fourier-Transform, Iteration, and Least-Squares-Fit Demodulation Image-Processing for Analysis of Single-Carrier Fringe Pattern," *J Opt Soc Am A* 12(10), 2159-2164 (1995)

39. S. De Nicola and P. Ferraro, "Fourier transform method of fringe analysis for moire interferometry," *J Opt a-Pure Appl Op* 2(3), 228-233 (2000)

40. J. H. Massig and J. Heppner, "Fringe-pattern analysis with high accuracy by use of the Fourier-transform method: theory and experimental tests," *Appl Optics* 40(13), 2081-2088 (2001)

41. L. L. Deck, "Fourier-transform phase-shifting interferometry," *Appl Optics* 42(13), 2354-2365 (2003)

42. O. Y. Kwon, "Multichannel Phase-Shifted Interferometer," *Opt Lett* 9(2), 59-61 (1984)

43. B. Brueckmann and W. Thieme, "Computer-Aided Analysis of Holographic Interferograms Using the Phase-Shift Method," *Appl Optics* 24(14), 2145-2149 (1985)

44. M. Chang, C. P. Hu, P. Lam and J. C. Wyant, "High-Precision Deformation Measurement by Digital Phase-Shifting Holographic-Interferometry," *Appl Optics* 24(22), 3780-3783 (1985)

45. Y. Ishii, J. Chen and K. Murata, "Digital Phase-Measuring Interferometry with a Tunable Laser Diode," *Opt Lett* 12(4), 233-235 (1987)

46. M. Kujawinska, "Use of Phase-Stepping Automatic Fringe Analysis in Moire Interferometry," *Appl Optics* 26(22), 4712-4714 (1987)

47. K. Kinnstaetter, A. W. Lohmann, J. Schwider and N. Streibl, "Accuracy of Phase-Shifting Interferometry," *Appl Optics* 27(24), 5082-5089 (1988)

48. E. Vikhagen and O. J. Lokberg, "Detection of Defects in Composite-Materials by Television Holography and Image-Processing," *Mater Eval* 48(2), 244-248 (1990)

49. G. Lai and T. Yatagai, "Generalized Phase-Shifting Interferometry," *J Opt Soc Am A* 8(5), 822-827 (1991)

50. K. Okada, A. Sato and J. Tsujiuchi, "Simultaneous Calculation of Phase Distribution and Scanning Phase-Shift in Phase-Shifting Interferometry," *Opt Commun* 84(3-4), 118-124 (1991)

51. C. Y. Poon, M. Kujawinska and C. Ruiz, "Automated Fringe Pattern-Analysis for Moire Interferometry," *Exp Mech* 33(3), 234-241 (1993)

52. C. Y. Poon, M. Kujawinska and C. Ruiz, "Spatial-Carrier Phase-Shifting Method of Fringe Analysis for Moire Interferometry," *J Strain Anal Eng* 28(2), 79-88 (1993)

53. Y. Morimoto and M. Fujisawa, "Fringe Pattern-Analysis by a Phase-Shifting Method Using Fourier-Transform," *Opt Eng* 33(11), 3709-3714 (1994)

54. Y. Surrel, "Design of algorithms for phase measurements by the use of phase stepping," *Appl Optics* 35(1), 51-60 (1996)

55. G. Stoilov and T. Dragostinov, "Phase-stepping interferometry: Five-frame algorithm with an arbitrary step," *Opt Laser Eng* 28(1), 61-69 (1997)

56. G. H. Kaufmann, "Phase shifting in speckle photography," *Opt Laser Eng* 29(2-3), 117-123 (1998)

57. A. Davila, P. D. Ruiz, G. H. Kaufmann and J. M. Huntley, "Measurement of sub-surface delaminations in carbon fibre composites using high-speed phase-shifted speckle interferometry and temporal phase unwrapping," *Opt Laser Eng* 40(5-6), 447-458 (2003)

58. H. M. Xie, Z. W. Liu, D. N. Fang, F. L. Dai, H. J. Gao and Y. P. Zhao, "A study on the digital nano-moire method and its phase shifting technique," *Meas Sci Technol* 15(9), 1716-1721 (2004)

59. H. M. Xie, H. X. Shang, F. L. Dai, B. Li and Y. M. Xing, "Phase shifting SEM moire method," *Opt Laser Technol* 36(4), 291-297 (2004)

60. M. C. Brito, J. M. Alves, J. M. Serra, R. M. Gamboa, C. Pinto and A. M. Vallera, "Measurement of residual stress in EFG ribbons using a phase-shifting IR photoelastic method," *Sol Energ Mat Sol C* 87(1-4), 311-316 (2005)

61. Y. Morimoto, T. Nomura, M. Fujigaki, S. Yoneyama and I. Takahashi, "Deformation measurement by phase-shifting digital holography," *Exp Mech* 45(1), 65-70 (2005)

62. J. L. Chen, C. R. Sun, Y. W. Qin and X. H. Ji, "Damage evaluation of subsurface defect in sandwich by phase-shifting digital shearography," *Fracture and Strength of Solids Vi, Pts 1 and 2* 306-308(399-404 (2006)

63. F. Henault, "Conceptual design of a phase-shifting telescope-interferometer," *Opt Commun* 261(1), 34-42 (2006)

64. Y. Min, M. Hong, Z. Xi and L. Jian, "Determination of residual stress by use of phase shifting moire interferometry and hole-drilling method," *Opt Laser Eng* 44(1), 68-79 (2006)

65. C. Quan, S. H. Wang and C. J. Tay, "Nanoscale surface deformation inspection using FFT and phase-shifting combined interferometry," *Precis Eng* 30(1), 23-31 (2006)

66. H. N. Yen, D. M. Tsai and J. Y. Yang, "Full-field 3-D measurement of solder pastes using LCD-based phase shifting techniques," *Ieee T Electron Pack* 29(1), 50-57 (2006)

67. C. Han and B. Han, "Phase-shifting in achromatic moiré interferometry system," *OPTICS EXPRESS* 15(16), 9970-9976 (2007)

68. J. M. Huntley, "Automated fringe pattern analysis in experimental mechanics: a review," *J Strain Anal Eng* 33(2), 105-125 (1998)

69. Z. Y. Wang, "Development and Application of Computer-aided Fringe Analysis," in *Mechanical Engineering*, University of Maryland, Maryland (2003).

70. K. Itoh, "Analysis of the Phase Unwrapping Algorithm," *Appl Optics* 21(14), 2470-2470 (1982)

71. R. M. Goldstein, H. A. Zebker and C. L. Werner, "Satellite Radar Interferometry - Two-Dimensional Phase Unwrapping," *Radio Science* 23(4), 713-720 (1988)

72. J. M. Huntley, "Noise-Immune Phase Unwrapping Algorithm," *Appl Optics* 28(16), 3268-3270 (1989)

73. D. J. Bone, "Fourier Fringe Analysis - the 2-Dimensional Phase Unwrapping Problem," *Appl Optics* 30(25), 3627-3632 (1991)

74. N. H. Ching, D. Rosenfeld and M. Braun, "Two-dimensional phase unwrapping using a minimum spanning tree algorithm," *Ieee T Image Process* 1(3), 355-365 (1992)

75. T. R. Judge and P. J. Bryanstoncross, "A Review of Phase Unwrapping Techniques in Fringe Analysis," *Opt Laser Eng* 21(4), 199-239 (1994)

76. D. C. Ghiglia and L. A. Romero, "Robust 2-Dimensional Weighted and Unweighted Phase Unwrapping That Uses Fast Transforms and Iterative Methods," *J Opt Soc Am A* 11(1), 107-117 (1994)

77. J. A. Quiroga, A. Gonzalezcano and E. Bernabeu, "Phase-Unwrapping Algorithm-Based on an Adaptive Criterion," *Appl Optics* 34(14), 2560-2563 (1995)

78. D. Kerr, G. H. Kaufmann and G. E. Galizzi, "Unwrapping of interferometric phase-fringe maps by the discrete cosine transform," *Appl Optics* 35(5), 810-816 (1996)

79. D. C. Ghiglia and L. A. Romero, "Minimum L(p)-norm two-dimensional phase unwrapping," *J Opt Soc Am A* 13(10), 1999-2013 (1996)

80. T. J. Flynn, "Two-dimensional phase unwrapping with minimum weighted discontinuity," *J Opt Soc Am A* 14(10), 2692-2701 (1997)

81. D. C. Ghiglia and M. D. Pritt, *Two-Dimensional Phase Unwrapping: Theory, Algorithms, and Software*, Wiley, New York (1998).

82. G. H. Kaufmann, G. E. Galizzi and P. D. Ruiz, "Evaluation of a preconditioned conjugate-gradient algorithm for weighted least-squares unwrapping of digital speckle-pattern interferometry phase maps," *Appl Optics* 37(14), 3076-3084 (1998)

83. W. Xu and I. Cumming, "A region-growing algorithm for InSAR phase unwrapping," *Ieee Transactions on Geoscience and Remote Sensing* 37(1), 124-134 (1999)

84. M. A. Herraez, D. R. Burton, M. J. Lalor and M. A. Gdeisat, "Fast two-dimensional phase-unwrapping algorithm based on sorting by reliability following a noncontinuous path," *Appl Optics* 41(35), 7437-7444 (2002)

85. W. S. Li and X. Y. Su, "Phase unwrapping algorithm based on phase fitting reliability in structured light projection," *Opt Eng* 41(6), 1365-1372 (2002)

86. J. Arines, "Least-squares modal estimation of wrapped phases: application to phase unwrapping," *Appl Optics* 42(17), 3373-3378 (2003)

87. A. Baldi, "Phase unwrapping by region growing," *Appl Optics* 42(14), 2498-2505 (2003)

88. X. Y. Su and W. J. Chen, "Reliability-guided phase unwrapping algorithm: a review," *Opt Laser Eng* 42(3), 245-261 (2004)

89. J. M. Bioucas-Dias and G. Valadao, "Phase unwrapping via graph cuts," *Lect Notes Comput Sc* 3522, 360-367 (2005)

90. Y. G. Lu, X. Z. Wang and G. T. He, "Phase unwrapping based on branch cut placing and reliability ordering," *Opt Eng* 44(5), - (2005)

91. B. Marendic, Y. Y. Yang and H. Stark, "Phase unwrapping using an extrapolation-projection algorithm," *J Opt Soc Am A* 23(8), 1846-1855 (2006)

92. Y. J. Zhu, L. R. Liu, Z. Luan and A. H. Li, "A reliable phase unwrapping algorithm based on the local fitting plane and quality map," *J Opt a-Pure Appl Op* 8(6), 518-523 (2006)

93. Y. G. Lu, X. Z. Wang and X. P. Zhang, "Weighted least-squares phase unwrapping algorithm based on derivative variance correlation map," *Optik* 118(2), 62-66 (2007)

94. L. An, Q. S. Xiang and S. Chavez, "A fast implementation of the minimum spanning tree method for phase unwrapping," *Ieee T Med Imaging* 19(8), 805-808 (2000)

95. W. Bossaert, R. Dechaene and A. Vinckier, "Computation of finite strains from moire´ displacement patterns," *J Strain Anal Eng* 3, 63-75 (1968)

96. H. A. Vrooman and A. A. M. Maas, "Image-Processing Algorithms for the Analysis of Phase-Shifted Speckle Interference Patterns," *Appl Optics* 30(13), 1636-1641 (1991)

97. A. J. Moore and J. R. Tyrer, "Two-dimensional strain measurement with ESPI," *Opt Laser Eng* 24(5-6), 381-402 (1996)

98. J. Morton, D. Post, B. Han and M. Y. Tsai, "A Localized Hybrid Method of Stress-Analysis - a Combination of Moire Interferometry and Fem," *Exp Mech* 30(2), 195-200 (1990)

99. M. Y. Tsai and J. Morton, "New Developments in the Localized Hybrid Method of Stress-Analysis," *Exp Mech* 31, 298-305 (1990)

100. J. Rhee, S. He and R. E. Rowlands, "Hybrid Moire-numerical stress analysis around cutouts in loaded composites," *Exp Mech* 36(4), 379-387 (1996)

101. K. R. Castleman, *Digital Image processing*, Prentice-Hall, New Jersey (1996).

102. R. C. Gonzalez and R. E. Woods, *Digital Image processing*, Pearson Prentice Hall, New York (2007).

103. M. L. Speriatu, "Temperature Dependent Mechanical Properties of Composite Materials and Uncertainties in Experimental Measurement," in *Mechanical and Aerospace Engineering*, University of Florida, Gainesville (2005).

104. K. G. Larkin and B. F. Oreb, "Design and Assessment of Symmetrical Phase-Shifting Algorithms," *J Opt Soc Am A* 9(10), 1740-1748 (1992)

105. J. R. Lee, J. Molimard, A. Vautrin and Y. Surrel, "Digital phase-shifting grating shearography for experimental analysis of fabric composites under tension," *Compos Part a-Appl S* 35(7-8), 849-859 (2004)

106. J. Duchon, "Splines minimizing rotation-invariant semi-norms in Sobolev spaces. In Constructive Theory of Functions of Several Variables. vol 1, pp 85-100 (Springer Berlin / Heidelberg)," *Constructive Theory of Functions of Several Variables* 1, 85-100 (1976)

107. G. Donato and S. Belongie, "Approximate thin plate spline mappings," *Computer Vision - Eccv 2002 Pt Iii* 2352, 21-31 (2002)

108. I. Barrodale, D. Skea, M. Berkley, R. Kuwahara and R. Poeckert, "Warping Digital Images Using Thin Plate Splines," *Pattern Recogn* 26(2), 375-376 (1993)

109. H. Guo, J. Y. Jiang and L. M. Zhang, "Building a 3D morphable face model by using thin plate splines for face reconstruction," *Advances in Biometric Person Authentication, Proceedings* 3338, 258-267 (2004)

110. M. J. D. Powell, "A thin plate spline method for mapping curves into curves in two dimensions," *Computational Techniques and Applications (CTAC95), Melbourne, Australia, 1995* (1995)

111. F. Girosi, M. Jones and T. Poggio, "Regularization Theory and Neural Networks Architectures," *Neural Comput* 7(2), 219-269 (1995)

112. R. C. Gonzalez, R. E. Woods and S. L. Eddins, *Digital Image processing*, Pearson Prentice Hall, New York (2002).

113. R. C. Gonzalez, R. E. Woods and S. L. Eddins, *Digital Image processing using MATLAB* Pearson Prentice Hall, New York (2004).

114. H. T. Hahn and N. J. Pagano, "Curing Stresses in Composite Laminates," *J Compos Mater* 9(Jan), 91-106 (1975)

115. Z. Wu, J. A. Lu and B. T. Han, "Study of residual stress distribution by a combined method of moire interferometry and incremental hole drilling, part I: Theory," *J Appl Mech-T Asme* 65(4), 837-843 (1998)

116. O. Sicot, X. L. Gong, A. Cherouat and J. Lu, "Determination of residual stress in composite laminates using the incremental hole-drilling method," *J Compos Mater* 37(9), 831-844 (2003)

117. H. T. Hahn, "Residual-Stresses in Polymer Matrix Composite Laminates," *J Compos Mater* 10(Oct), 266-278 (1976)

118. R. Y. Kim and H. T. Hahn, "Effect of Curing Stresses on the First Ply-Failure in Composite Laminates," *J Compos Mater* 13(Jan), 2-16 (1979)

119. B. Benedikt, R. Rupnowski, L. Kumosa, J. K. Sutter, P. K. Predecki and M. Kumosa, "Determination of interlaminar residual thermal stresses in a woven 8HS graphite/PMR-15 composite using X-ray diffraction measurements," *Mech Adv Matl Struct* 9(4), 375-394 (2002)

120. I. G. Zewi, I. M. Daniel and J. T. Gotro, "Residual-Stresses and Warpage in Woven-Glass Epoxy Laminates," *Exp Mech* 27(1), 44-50 (1987)

121. W. A. Schulz, "Determination of residual stress and thermal behavior for composite laminates," in *Mechanical and Aerospace Engineering*, University of Florida, Gainesville (2005).

122. X. G. Huang, J. W. Gillespie and T. Bogetti, "Process induced stress for woven fabric thick section composite structures," *Compos Struct* 49(3), 303-312 (2000)

123. R. Karkkainen, "Stress Gradient Failure Theory for Textile Structural Composites," in *Mechanical and Aerospace Engineering*, University of Florida, Gainesville (2006).

124. P. G. Ifju, X. Niu, B. C. Kilday, S. C. Liu and S. M. Ettinger, "Residual strain measurement in composites using the cure-referencing method," *Exp Mech* 40(1), 22-30 (2000)

125. P. G. Ifju, J. E. Masters and W. C. Jackson, "The Use of Moire Interferometry as an Aid to Standard Test-Method Development for Textile Composite-Materials," *Compos Sci Technol* 53(2), 155-163 (1995)

126. N. M. Strickland, "Residual Strain Measurement of Plain Weave Composites Using The Cure Reference Method," in *Mechanical and Aerospace Engineering*, University of Florida, Gainesville (2007).

127. V. Carvelli and C. Poggi, "A homogenization procedure for the numerical analysis of woven fabric composites," *Compos Part a-Appl S* 32(10), 1425-1432 (2001)

128. J. B. Berman and S. R. White, "Theoretical modelling of residual and transformational stresses in SMA composites," *Smart Mater Struct* 5(6), 731-743 (1996)

129. ASTM, "Standard Test Method for Length Change of Hardened Hydraulic-Cement Mortar and Concrete," in *C157/C157M-06*.

130. J. K. Kim and C. S. Lee, "Prediction of differential drying shrinkage in concrete," *Cement Concrete Res* 28(7), 985-994 (1998)

131. F. Yilmazturk, Kulur, S., Pekmezci, B.Y., "Measurement of Shrinkage in Concrete Samples using Digital Photogrammetric Methods," *The International Archives of the Photogrammtry, Remote Sensing and Spatial Information Sciences* 34(2003)

132. N. M. Strickland, Yin, W.Q., Ifju, P.G., "Residual Strain Measurement Analysis of Woven Composites using Phase Shifting," in *SEM Annual Conference and Exposition - 10th International Congress and Exhibition on Experimental and Applied Mechanics*, pp. 1855-1860 (2007).

133. W. Q. Yin, Strickland, N. M., Ifju, P.G., "Residual Strain Measurement and Analysis of Plain Woven Composites," in *49th AIAA/ASME/ASCE/AHS/ASC Structures, Structural Dynamics, and Materials Conference*, Chicago (2008).

134. W. Q. Yin, Strickland, N. M., Ifju, P.G., "Residual Strain Measurement and Residual Stress Prediction of Woven Composites," in *Society for Experimental Mechanics - 11th International Congress and Exhibition on Experimental and Applied Mechanics*, pp. 687-694, Orlando, FL (2008).

135. S.-C. Liu, "Residual Stress Characterization for Laminated Composites," in *Mechanical Engineering*, University of Florida, Gainesville (1999).

136. T. C. Chen, Yin, W.Q., Ifju, P.G., "Shrinkage Measurement of Concrete Using Phase Shifting," in *Society for Experimental Mechanics - 11th International Congress and Exhibition on Experimental and Applied Mechanics*, pp. 1092-1100 (2008).

137. T. C. Chen, Yin, W.Q., Ifju, P.G., "Experimental Investigation of Aggregate Effects on Shrinkage Behavior in Concrete Materials," in *Society for Experimental Mechanics - 12th International Congress and Exhibition on Experimental and Applied Mechanics* (2009).

138. C. Gogu, "Facilitating Bayesian Identification of Elastic Constants Through Dimensionality Reduction and Response Surface Methodology," in *Mechanical and Aerospace Engineering*, p. 229, University of Florida, Gainesville (2009).

139. D. Lecompte, Sol, H., Vantomme, J., and Habraken, A. M., "Identification of elastic orthotropic material parameters based on ESPI measurements," in *SEM Annual Conference and Exposition on Experimental and Applied Mechanics* (2005).

140. G. Silva, Le Riche, R., Molimard, J., Vautrin, A., and Galerne, C., "Identification of Material Properties Using FEMU: Application to the Open Hole Tensile Test," *Applied Mechanics and Materials* 7-8 (2007)

141. W. J. Noh, "Mixed Mode Interfacial Fracture Toughness of Sandwich Composites at Cryogenic Temperatures," in *Mechanical and Aerospace Engineering*, University of Florida, Gainesville, FL (2004).

BIOGRAPHICAL SKETCH

Weiqi Yin was born in Hunan Province of China in 1980. He received both his master's and bachelor's degree in engineering mechanics from Tsinghua University, China, in 2004 and 2002 respectively. He also got a Master of Science in mechanical engineering at University of Florida in 2007. He received his Pd.D. in mechanical engineering at University of Florida in the fall of 2009.

Yin's research interests are focused on experimental stress analysis including moiré interferometry, digital image correlation, strain gage, etc., composite materials, finite element analysis, and digital image processing.